UNIWERSYTET WARSZAWSKI
Wydział Fizyki

ROZPRAWA DOKTORSKA

Optical Properties of Photonic Crystal Fibers Infiltrated with Liquids

by

Hoang Van Thuy

Doctoral dissertation prepared under the supervision of:

Prof. dr hab. inż. Ryszard Buczyński

University of Warsaw, Faculty of Physics, Poland

and

Dr hab. inż. Mateusz Śmietana

Warsaw University of Technology,
Institute of Microelectronics and Optoelectronics, Poland

September 2020

Abstract

The dissertation concerns optical properties of selected hollow core photonic crystal fibers (PCF), where the core was infiltrated with a broad selection of liquids. The research work includes supercontinuum generation (SCG) in PCFs infiltrated with high nonlinear liquids and studies on transmission windows for antiresonant (AR) fibers filled with low-index liquids for application in bio-lasers and bio-sensing.

The work contains three main parts. The first part includes design, fabrication, and characterization of linear properties of liquid core PCFs. A thermal method based on a conventional fusion splicer has been used to obtain selective filling of the core with liquids. Dispersion characteristics of liquid core PCFs with different structures were simulated numerically and later experimentally verified using March-Zehnder interferometer. This part of the work verifies if liquid core PCFs make possible to obtain all-normal and flat dispersion in the near-infrared spectral range.

The second part of the work includes measurements of SCG using PCFs infiltrated with high-refractive index liquids such as toluene and carbon tetrachloride (CCl_4). When a commercial femtosecond laser was used as a pump source, the liquid core fibers offered supercontinuum (SC) spectrum in the near-infrared region and showed potential for coherence. This part also discusses dynamics of SC formation in liquid-core PCFs, including self-phase modulation followed by optical wave breaking for spectral broadening in all-normal dispersion regime, and soliton dynamics for anomalous dispersion SCG. Due to the design flexibility of the PCFs and the high nonlinearity of liquid, the liquid core PCFs may offer broad SC spectrum with low peak power of input pulses. Therefore, the liquid core PCFs, when supported by commercially available high power laser sources, can be used as components for all-fiber SCG systems. Such systems allow for manufacturing of low-cost coherent SC sources for various applications such as e.g., frequency comb generation, sensing, and medical imaging. Moreover, in order to couple the liquid core PCF with a single mode fiber when all-fiber SCG system is considered, within this work a large mode area (LMA) silica PCF was additionally designed and fabricated. Proposed LMA PCF show low nonlinear properties, low bending loss and it can offer high coupling efficiency with the liquid core PCFs.

The last part of the work focus on the properties of AR fibers infiltrated with low-index liquids, e.g., water and ethanol. In this case, the fibers were filled and other than total internal reflection guiding was implemented. The aim of this part was to verify if the AR fiber with liquid infiltration could offer a broad transmission window. The experiments have proven that the transmission windows of AR fiber experience blue-shift when the fiber is filled with low-index liquids. The shift depends on the refractive index of the liquid and thickness of the capillaries in the cladding region of the fiber. Due to the broad transmission window, the AR fiber infiltrated with low-

index liquid may become a promising approach for optofluidic applications. Thus, in this part, optical properties of commercially available liquids used for biological experiments were also measured over storage time. The biologically-active structures, such as bacteria or cells, require specific life-supporting aqueous solutions called as buffers or cell culture media. Refractive index, transmission spectra and scattering for all the considered liquids are presented and compared with those of pure water. Moreover, influence of aging on the investigated properties has also been discussed. Finally, AR fibers infiltrated with these solutions containing the microorganisms for application in the optofluidic system were discussed.

Streszczenie

Rozprawa obejmuje analizę właściwości optycznych wybranych światłowodów fotonicznych (ang. *photonic crystal fibers*, PCF), których rdzeń został wypełniony cieczami o różnych właściwościach. W szczególności skupiono się na generacji superkontinuum (ang. *supercontinuum generation*, SCG) w światłowodach PCF wypełnionych wysoce nieliniowymi cieczami oraz analizie właściwości transmisyjnych światłowodów antyrezonansowych (AR) wypełnionych cieczami o niskim współczynniku załamania do ich zastosowań w biolaserach i bioczujnikach.

Praca składa się z trzech głównych części. Pierwsza część obejmuje tematykę projektowania, wytwarzania i charakteryzacji właściwości liniowych światłowodów PCF z rdzeniem wypełnionym cieczą. Do selektywnego wypełniania rdzenia cieczami wykorzystano techniką termiczną bazującą na użyciu konwencjonalnej spawarki światłowodowej. Charakterystyki dyspersyjne światłowodów PCF o różnej strukturze i rdzeniem wypełnionym cieczami zostały wyznaczone z użyciem metod numerycznych, a następnie zweryfikowane eksperymentalnie z użyciem układu interferometru Macha-Zehndera. Ta część rozprawy została poświęcona weryfikacji możliwość uzyskania w światłowodach PCF z rdzeniem wypełnionym cieczami całkowicie normalnej i płaskiej dyspersji w zakresie spektralnym bliskiej podczerwieni.

Druga część pracy zawiera pomiary SCG w światłowodach PCF wypełnionych cieczami o wysokim współczynniku załamania, takich jak toluen i CCl_4. Gdy komercyjny laser femtosekundowy został użyty jako źródło pompujące, światłowody z rdzeniem wypełnionym cieczami pozwoliły na uzyskanie widma superkontinuum (ang. *supercontinuum*, SC) w zakresie bliskiej podczerwieni i wykazującego potencjał do koherencji. Ta część rozprawy obejmuje także analizę dynamiki kształtowania widma SC w bliskiej podczerwieni, gdzie wzięto pod uwagę samomodulację fazy poprzedzającą optyczne łamanie fali dla poszerzenia widmowego w zakresie dyspersji normalnej, a także dynamikę solitonową dla SCG w zakresie dyspersji anomalnej. Dzięki szerokim możliwościom w zakresie projektowana i wytwarzania światłowodów PCF oraz wysokiej nieliniowości zastosowanych cieczy, światłowody PCF z rdzeniem wypełnionym cieczą pozwalają uzyskać szerokie widmo SC nawet przy małej mocy impulsów wejściowych. Cecha ta pozwala to na wykorzystanie światłowodów PCF z rdzeniem wypełnionym cieczą jako komponentów w całkowicie światłowodowych systemach SCG, które mogą być używane z dostępnymi komercyjnie źródłami laserowymi dużej mocy. Takie systemy pozwalają na wytwarzanie relatywnie tanich źródeł koherentnego SC dla wielu zastosowań obejmujących m.in. generację grzebieni częstotliwości, a także zastosowania czujnikowe i obrazowanie medyczne. Ponadto, w ramach realizacji prac badawczych w zakresie sprzężenia światła ze światłowodu PCF wypełnionego cieczą

do światłowodu jednomodowego w całkowicie światłowodowym układzie SCG, dodatkowo zaprojektowano i wytworzono krzemionkowy światłowód PCF o dużym polu modu (ang. *large mode area*, LMA). Zaproponowany światłowód LMA PCF charakteryzuje się niską nieliniowością, małymi stratami zgięciowymi oraz umożliwia uzyskanie wysokiej wydajność sprzężenia światła ze światłowodem PCF z rdzeniem wypełnionym cieczą.

Trzecia część rozprawy została poświęcona analizie właściwości światłowodów AR wypełnionych cieczami o niskim współczynniku załamania, takimi jak wodą i etanolem. Dla takich światłowodów mimo wypełnienia ich wspomnianymi cieczami zachodzi inny mechanizm propagacji niż całkowite wewnętrzne odbicie. Celem tej części rozprawy było zweryfikowanie czy światłowód AR wypełniony cieczą może zapewnić szerokie okno transmisji. Eksperymenty potwierdziły, że okna transmisji światłowodu AR po wypełnieniu cieczami podlegają przesunięciu w kierunku fal krótszych. Przesunięcie to zależy od współczynnika załamania cieczy i grubości ścianki kapilary w strukturze płaszcza światłowodu. Dzięki szerokim oknom transmisji światłowód AR wypełniony cieczą o niskim współczynniku załamania jest obiecującym rozwiązaniem do zastosowań optofluidycznych. Mając to na uwadze, w tej części rozprawy zostały zbadane właściwości optyczne dostępnych komercyjnie cieczy używanych w realizacji eksperymentów biologicznych. Analizie poddano również zmiany właściwości tych cieczy wraz z czasem ich przechowywania. Struktury biologicznie, takie jak bakterie lub komórki, wymagają specjalnych roztworów wodnych podtrzymujących procesy życiowe, które nazywane są buforami lub pożywkami do hodowli komórkowych. Współczynnik załamania, widma transmisji i rozpraszania dla wybranych cieczy tego typu zostały zaprezentowane i porównane z właściwościami wody. Przedyskutowano także wpływ starzenia tych roztworów na ich właściwości. Następnie omówiono wykorzystanie światłowodów AR wypełnionych tymi roztworami biologicznymi zawierającymi mikroorganizmy do zastosowań w układach optofluidycznych.

Acknowledgments

This dissertation would be impossible without the help, support, and advice from my family, supervisors, friends, and teammates.

First of all, I would like to express my sincere gratitude to my supervisor, prof. dr. hab. inż. Ryszard Buczyński, for his patience, enthusiasm and insightful guidance throughout my PhD study.

I would like to express my sincere gratitude to my supervisor, dr. hab. inż. Mateusz Śmietana, for his exceptional patience and scientific support.

I am deeply indebted to dr. hab. inż. Rafał Kasztelanic from Faculty of Physics, University of Warsaw for his advice and mentoring in a scientific career.

I am deeply indebted to dr. hab. inż. Mariusz Klimczak from Faculty of Physics, University of Warsaw for his help in discussing the scientific results.

I am grateful to dr. hab. Cao Long Van, prof UZ for encouraging me in the process of completing the thesis.

I would like to express my gratitude to International Cooperation Department, Vietnamese Ministry of Education and Training, and Vinh University let me had the opportunity to do my PhD in Poland.

I would like to express my gratitude to all teammates of Structured Optics & Optofluidics Group of Faculty of Physics, University of Warsaw and Glass Department of the Institute of Electronic Materials Technology, in particular: dr. inż. Grzegorz Stępniewski, dr. inż. Alicja Anuszkiewicz, mgr. Dominik Dobrakowski.

I would like to thank dr. inż. Bartłomiej Siwicki at Heriot-Watt University for his help and guidance at the beginning time I started to work for this dissertation.

I would like to thank the Institute of Geophysics, Faculty of Physics, University of Warsaw for giving me permission to commence this dissertation.

This work has been realized within Foundation for Polish Science Team Programme from the funds of European Regional Development Fund under Smart Growth Operational Programme (TEAM TECH/2016-1/1).

List of Acronyms

AR	Antiresonant
A_{eff}	Effective mode area
BS	Beam splitter
CCl_4	Carbon tetrachloride
C_2Cl_4	Tetrachloroethylene
CCM	Cell culture media
CS_2	Carbon disulfide
CL	Confinement loss
D	Dispersion
D_g	Waveguide dispersion
D_m	Material dispersion
d_{core}	Core diameter
DMEM	Dulbecco's Modified Eagle's Medium
DW	Dispersive wave
EDTA	Ethylenediaminetetraacetic acid
EXPRESS 5	Express Five™ SFM
FDE	Finite difference eigenmode
FWM	Four-wave mixing
GNLSE	General nonlinear Schrödinger Equations
GVD	Group-velocity dispersion
IR	Infrared
k	Imaginary part of complex refractive index
LMA	Large mode area
M	Soliton number
MIR	Mid-infrared
ML	Material loss
MO	Microscope objective
NDF	Neutral density filter
NIR	Near-infrared
$N(\lambda)$	Group refractive index
$N_a(\lambda)$	Relative refractive index
$N_{eff}(\lambda)$	Effective group refractive index
$n_{eff}(\lambda)$	Effective refractive index
$n(\lambda)$	Phase refractive index
$n_c(\lambda)$	Complex refractive index
OPA	Optical parametric amplifier
OPO	Optical parametric oscillator
OWB	Optical wave breaking
PBG	Photonic band-gap
PBS	Dulbecco Phosphate Buffered Saline
PCF	Photonic crystal fiber
PMLs	Perfectly matched layers

SC	Supercontinuum
SCG	Supercontinuum generation
SEM	Scanning electron micrograph
SPM	Self-phase modulation
SSL	Surface scattering loss
SSFS	Soliton self-frequency shift
SSFM	Split-Step Fourier Method
SRS	Stimulated Raman scattering
TBE	TRIS- Borate-EDTA Buffer
TIR	Total internal reflection
ZDW	Zero dispersion wavelength
f	Filling factor
Λ	Lattice constant
λ	Wavelength
η	Coupling efficiency

CONTENTS

1 Introduction

1.1 Brief History of Optical Fiber

Optical fibers are one of the greatest scientific advents in the last century. Nowadays, they have found their important role in, e.g., communication, lasers, sensors, imaging technique, etc. Light guiding by total internal reflection (TIR) was first demonstrated by D. Colladon [1,2] and J. Tyndall [3] in the mid-nineteenth century. In the 1920s, C. Hansell [4] and J. L. Baird [5] used a glass fiber bundle to send images. It is to note that at that time only bare glass fibers were used. For this reason light was propagated away from the fibers when they were touching each other or their surface was scratched. Consequently, the fibers were quite leaky and did not transmit much light. A breakthrough to meet this problem was reported in the 1950s that was to cover of glass fiber with a lower refractive index material [6,7]. This feature significantly decreased the confinement loss of the fiber. This type of fiber structure including core and cladding has been the basic optical fiber solution until today. Subsequent intensive studies aimed at explaining the mechanisms of glass losses [8] and technological progress allowed fabrication of an optical fiber with attenuation of 16 dB/km at wavelength of 0.633 μm [9]. Based on this experimental realization of low loss optical fiber in 1970 [9], worldwide communication - among other fields - experienced extraordinary growth.

The conventional fiber guides the light due to TIR. However, the small difference in refractive index (Δn) of core and the cladding causes bending loss. For example, the bending loss of SMF-28 – a commercial single mode fiber [10] – is 0.5 dB at 1.55 μm for one turn with a bend radius of 10 mm [10]. Higher Δn may be obtained by using silica doping with other material, e.g., germanium [11]. However, the doping of the core led to increase of attenuation of the fiber through increased absorption and Rayleigh scattering. The high attenuation caused a dramatic decrease in output power. Also, the nonlinear effects on the scale of a few kilometers of propagation length in conventional fiber cannot be neglected. The optical nonlinearities of the fiber can have deleterious effects on optical signals in communication because the pulses propagated in the fiber are distorted in temporal and spectral profiles via the nonlinear effects. Thus, new guiding mechanisms to minimize or eliminate the effects of nonlinearity and attenuation of the fiber are expected. One of them was to use the air-glass microstructure for optical guiding [12, 13].

Another milestone in the development of fiber optics originated from the theory of S. John [14] and E. Yablonovitch [15]. They extended the concept of the band-gap mechanism in semiconductors for the photonics area. In 1991, E. Yablonovitch *et al.* reported the first experimental observation of the photonic band-gap effects in a bulk high-index material, which was created by simply drilling three sets of holes 35.26^0 off vertical into the top surface of solid slab or wafer [16]. Inspired by the experiment

of E. Yablonovitch *et al.*, P. St. J. Russel and his collaborators developed their own structure of fiber and fabricated the fiber by the method of stacking silica capillaries in a hexagonal pattern to guide the light in the core according to the band-gap mechanism. At the first attempt, their fibers had a solid core, which was surrounded by an array of micrometer-scaled air-holes arranged in a hexagonal lattice. Consequently, the fiber did not guide the light based on the photonic band-gap effect, but rather a mechanism akin to TIR [17]. Nowadays, this fiber is named *solid core PCF*. The most popular structure of this fiber was microstructured fibers of silica glass with air-holes arranged in a hexagonal lattice, in which the central region was replaced by a glass rod acting as the core, as shown in Figure 1.1(a). The advantage properties of solid core PCF compared to conventional fiber is able to optimize its dispersion, as well as other mode properties by changing the diameter and lattice pitch of air-holes the cladding region.

The efforts of Russel and his collaborators to guide the light in the air-core of the fiber were eventually reported in [18]. Their PCFs, in which the core was formed by including a larger air hole in the central region, as shown in Figure 1.1(b), could confine more than 99% of the light in its core over a distinct transmission window. Nowadays, this fiber is called *hollow core PCF*. The mechanism guiding of this fiber based on the photonic band-gap effect, thus it also has been named *photonic band-gap (PBG) fiber*.

Later, the following researches pointed out that the exact geometry of the cladding of hollow core PCF is not the crucial factor in displaying broadband guidance [19, 20], but the geometry of the first layer surrounding the core is crucial for the transmission performance of the fiber [21, 22]. In 2011, Wang *et al.* [22] optimized the structure of kagome hollow core PCF and experimentally demonstrated that loss of this fiber depends crucially on the core shape. In 2011, Pryamikov *et al.* [23] achieved a breakthrough to guide the light in the air-core fiber with further broad transmission windows. They fabricated and experimentally investigated transmission windows of fiber as shown in Figure 1.1(c). This fiber had a single cladding layer and the core was formed by a single row of silica capillaries and offered the relative broad transmission windows in the mid-infrared range (MIR) with low loss when compared with those of PBG fiber. Nowadays, this sort of fiber is known as *negative-curvature core fiber*. The guiding mechanism of this fiber based on the antiresonance, which plays a critical role in inhibiting the coupling between light in the core and other regions of the negative curvature fiber. Therefore, the other name of this fiber is *antiresonant (AR) fiber*.

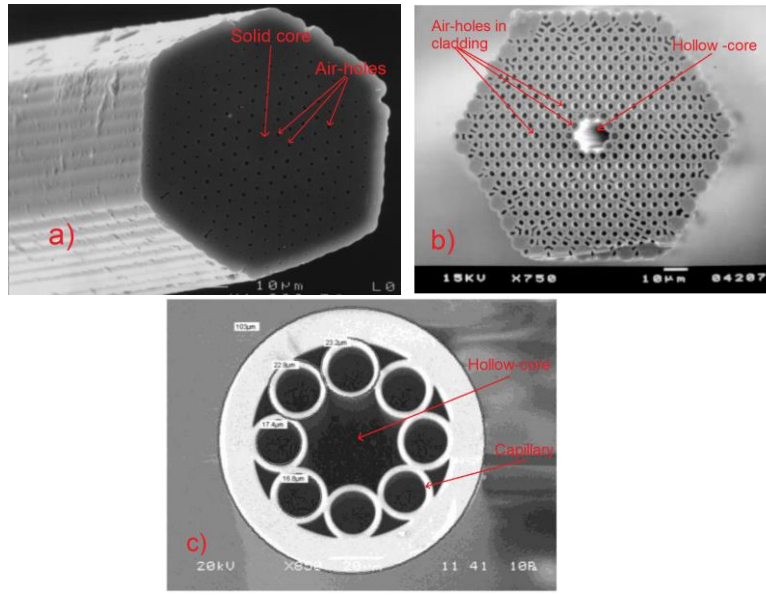

Figure 1.1. Scanning electron microscope (SEM) images of (a) solid core PCF [17], (b) PBG-fiber [18], (c) AR fiber [23].

Although the PCF can guide the light in the air-core, its attenuation is still not low enough for communication, since small disturbances in real microstructure and roughness of the inner surface of the walls cause significant losses. The minimum attenuation of hollow core PCF, in the laboratory, was achieved at 1.2 dB/km [24], and the attenuation of commercially available hollow core fibers reaches at least 30 dB/km at 1.55 μm wavelength [25], while attenuation of conventional communication fiber is around 0.2 dB/km at λ=1.55 μm [26]. Therefore, PCFs are not suitable for data transmission on long distances. However, with the huge possibilities of modifying the structure, and thus a high degree of freedom to optimize the optical properties, PCFs have found numerous applications. For instance, a large mode area (LMA) fiber can be used for high power delivery [27], and hollow core PCFs with low loss have been used in laser technology [28]. Liquids and gases can be detected by the sensor using suspended core PCF [29]. With the high capability to optimize dispersion and effective mode area, PCFs are a great choice to investigate the nonlinear phenomena resulting in, e.g., supercontinuum generation (SCG) [30].

Hollow core PCF can be selectively infiltrated with liquid into the core where it serves as a propagation medium. Due to the unique properties of the liquids, e.g., high nonlinearity, high transparency, capability for modification of its refractive index by changing ambient temperature, liquid core PCFs have numerous applications, e.g., in sensing and SCG.

The AR fibers infiltrated with low-index liquid can be used for optofluidic lasers [31]. They have also been used as temperature sensors [32] because the high-loss resonant wavelengths of these fibers are sensitive to change of the liquid's refractive index, which results from the change of temperature [32].

In recent years, the liquid core fibers have been intensively used for nonlinear optics study. In fact, in 1967, Shimizu *et al*. investigated the frequency broadening via the interaction between the light and liquid [33]. They used carbon disulfide in this study because it has a relatively high nonlinear refractive index, which is several times larger than that of fused silica. However, the early experiments with interaction between light and liquid were limited, because the liquid samples could only allow for propagation length of few centimeters. By incorporating liquid to fiber internal structure geometry, it is possible to obtain a nonlinear liquid medium in which the light is confined in the small region of the core (a few micrometers) and over a few decimeters of the long fiber sample. It is worthy of note that if the light is confined in the small area, the nonlinear coefficient of the liquid core fiber would increase, and thus, the nonlinear phenomena are enhanced.

1.2 Motivation and State-of-The-Art of Liquid Core Photonic Crystal Fiber

The aim of this work is to develop a nonlinear liquid core PCF for SCG applications, and liquid core AR fibers dedicate to sensors and optofluidic fiber lasers.

1.2.1 Nonlinear Liquid Core Photonic Crystal Fiber

Supercontinuum (SC) is generated when a collection of nonlinear optical processes and effects of dispersion act together upon the input pulses, which propagates in a nonlinear medium. These effects cause spectral broadening of input pulses. As a result, the output beam is a smoothly spectral continuum. The nonlinear media are typical glasses, nonlinear fibers, gases, and liquids. Nowadays, SC light source has played a significant role in various applications ranging from communication to advanced optical coherence tomography [34]. In particular, SC light source was used for high-precision optical frequency and time metrology [34], high-capacity encoding and decoding of information to terabits/sec communication, ultrafast laser pulse generation (attosecond pulses). With the advent of optical fibers, as well as non-silica material for nonlinear fibers, SC spectra have covered from ultra-violet to mid-infrared (MIR). The SC spectra in MIR range have had a transformative impact on biomedical imaging, optical coherence tomography [35], and MIR multispectral imaging of tissue. This approach allows for distinguishing between epithelial and surrounding connective tissue within colon tissue [36]. So far, the brightness of the infrared (IR) SC source can be compared with that of synchrotron IR beamlines [37].

Recently, three common approaches are used for SCG in optical fibers. The first one is to use the short pulse injecting to the nonlinear fibers, which are made from silica or soft-glasses, e.g., tellurite, chalcogenide, and fluoride. However, silica has a relatively low nonlinear - $n_2 = 2.74\times10^{-20}$ m^2/W at $\lambda = 1.053$ μm [38]. It is also not transparent in MIR range, what originates from multi-photon absorption on Si-O bonds and the vibrational resonance of OH- ions. Fluoride and tellurite glasses can extend the high transparent range up to 5.5 μm. However, fluoride glass is also low nonlinear ($n_2 = 3.4\times10^{-20}$ m^2/W at $\lambda = 1.55$ μm [39]). Tellurite glass has a high linear refractive index. Therefore, if single mode telluride fiber is considered, it will offer a small effective mode area. This feature leads to a low coupling efficiency between the nonlinear fiber and a standard single mode fiber when the all-fiber SCG system is considered. The chalcogenide glasses are interesting for SCG fiber because they are relatively high nonlinearity, such as As_2Se_3 chalcogenide glass has $n_2 = 16\times10^{-18}$ m^2/W at $\lambda = 1.55$ μm - 600 time higher than that of silica. They also have high transparency in MIR range (up to 20 μm [40]). Petersen *et al.* obtained SCG in the range from 1.4 μm up to 13 μm in chalcogenide fiber with input pulse having a central wavelength at 6.3 μm, 100 fs pulse duration and 760 μW (7.15 MW of peak power) [41]. However, zero-dispersion wavelengths (ZDWs) of dispersion characteristics of bulk chalcogenide glasses are located in the MIR range. Hence, it is challenging to design and fabricate a micro-structured chalcogenide fiber, which offers ZDW being compatible with a pump wavelength of commercially available high peak power laser sources. The SCG in chalcogenide fibers are usually pumped by a complex and expensive laser system with pump wavelength at MIR range, i.e., using the optical parametric amplifiers (OPAs) and oscillators (OPOs) [40,41]. Moreover, soft-glass fibers require a sophisticated cladding microstructure to reduce losses to acceptable levels and require complex fabrication methods. The faster changing of the viscosity of the soft-glasses during the process of drawing fibers requires a very accurate controlled temperature with a varied range of temperatures less than $\pm$ 25 ^{0}C, while for fused silica is $\pm$ 150 ^{0}C. The small temperature fluctuation leads to distorting the fiber structure during the drawing process. The applications of soft-glass fibers have also been limited by glass susceptibility to crystallization, glass toxicity, high purity requirements for the raw materials, and low mechanical resistance of the final fibers. In addition, the soft-glass fibers are mechanical weakness and difficult to splice with typical silica fibers. The huge difference in the thermal expansion coefficient of the soft glasses and that of silica makes the integration of fiber systems even more demanding.

The second approach for SCG fibers is to use the gas core PCFs. The gas core PCFs are typically low-loss and offer the tunability of both dispersion and nonlinear characteristics by changing the gas pressure and temperature [42]. Cssataro *et al.* observed the SCG from 0.27 μm to 3.1 μm in a gas-core AR fiber with an input pulse energy of 10 μJ, 100 fs pulse duration and central wavelength at 1.7 μm [43]. Adamu *et al.* reported the SCG in a gas core AR fiber with spectral bandwidth from 0.2 μm to 4 μm with input pulse having a central wavelength at 2.46 μm, pulse duration of 100

fs, and pulse energy of 8 μJ [44]. However, challenges of using gas-core PCF relate to the limitation of the transmission window, which is an inherited feature of hollow core PCFs based on the band-gap mechanism. The AR fibers usually have a relatively large mode area, and thus, require the relatively high input peak power, at hundreds of MW [43, 44], to obtain the broad SCG.

Another approach is to use liquid core fibers. The high nonlinearity of the liquids, e.g., organic solvents, can be comparable with soft-glasses commonly used in SCG fibers. The nonlinear refractive indices of nitrobenzene and carbon disulfide (CS_2) are up to two orders higher than that of silica [45]. High transparency of carbon disulfide and carbon chloride in the near-infrared (NIR) [46] allows for obtaining stable high-intensity and broad SCG for as long as 70 hours and the output power at watt-level [47]. The soliton dynamics for SCG in CS_2 core fibers have been reported in [48]. The results show that if the liquid with a high fraction of the non-instantaneous part of the nonlinearity is used, the effects of input noises on the degradation of temporal coherence of anomalous dispersion SCG in the liquid core fiber can be reduced [48]. The possibility of mixing of liquids allows to tune their linear refractive index, such as a mixture of CS_2 and carbon tetrachloride (CCl_4) with the proper refractive index for liquid core SCG fiber has been reported [49]. Moreover, the liquid core fibers also have the capability for real-time tuning their dispersion characteristics due to the relatively high thermo-optic coefficient of the liquid [50]. Table 1.1. shows the overview of experiments on SCG in liquid core PCFs.

It is well known that the dispersion characteristic of an optical fiber is a crucial factor in the process of the SCG [30], such as the fiber with near-zero flat dispersion will offer SCG with further broad spectral bandwidth. For an optical fiber, its dispersion is approx. a sum of material and waveguide dispersion [51]. Therefore, the general approach to optimize the dispersion of optical fibers for SCG is to modify their geometrical structure, e.g., core diameter, photonic cladding parameters.

As shown in Table 1.1, most of the experimental results of SCG in liquid core fibers are focused on step-index-liquid core optical fibers because they only require a straightforward and convenient method for filling microcapillaries with selected liquids. However, the lack of flexibility design in the case of step-index liquid core fibers leads to decreasing the degree of freedom to optimize their optical properties, e.g., dispersion, A_{eff}, single mode operation, for SCG applications.

On the other hand, hollow core PCFs infiltrated with high nonlinear liquid allows to determine dispersion characteristics and modal properties for SCG application through the modification of photonic cladding parameters, such as diameter and lattice pitch of the air-holes in the cladding region.

Table 1.1. The state of the art of SCG experiments of liquid core optical fibers.

	Liquid	Pulse width (fs)	Pulse energy (nJ)	Pump wavelength (μm)	Range of SC (μm)	All-normal	Ref.
Step index liquid core fibers	Toluene	18×10^3	200	0.532	0.550 ÷ 0.87	yes	[52]
	CS_2	180	2.55	1.91	1.79 ÷2.4	yes	[53]
	CS_2	450	0.83	1.685	1.2÷2.4	no	[54]
	CS_2	460	14	1.95	1.1 ÷ 2.7	no	[48]
	CS_2	350	0.5	1.92	1.2 ÷ 3	no	[50]
	TCE (C_2Cl_4)	270	0.5	1.92	1.1 ÷ 2.4	no	[50]
	CS_2	110	1.62	1.95	1.3 ÷ 2.5	no	[49]
Liquid core PCFs	Water	60	92	0.98	0.66 ÷1.14	no	[55]
	Water	45	7000	1.2	0.5 ÷ 1.5	no	[56]
	CCl_4	210	2.2	1.03	0.7 ÷ 1.3	no	[57]

The first SCG experiments with water-core PCFs were shown in [55,56]. However, the spectral broadening in these fibers is limited due to the high attenuation in NIR range and low nonlinear refractive index of water. The work in [56] used the input pulse with high peak power (150 MW) to obtain SC spectra. It is noted that too high input peak power leads to coherence degradation [58].

The works to analyze SCG in hollow core PCFs infiltrated with high nonlinear liquids were shown in [59-61]. Zhang *et al*. numerically studied the SCG in hollow core PCF with its core filled with highly nonlinear liquids such as CS_2 and nitrobenzene [59]. Owing to the high nonlinear refractive index of CS_2 - $n_2 = (4.3 \div 5.1)\times10^{-18}$ m^2/W at λ=1.064 μm [62] - the authors obtained SC spectrum from 1μm to 2.3 μm with low input peak power (1 kW). Van *et al.* and Dinh *et al.* obtained the broad all-normal dispersion SCG from visible to NIR range in CCl_4 and toluene-core PCFs [60, 61]. Although these works were based solely on numerical simulation, they show the potential of using liquid core PCF for SCG applications.

Because of given above, a part of my work is devoted to experimental verification of the concept of SCG in nonlinear liquid core PCFs. It includes the design, fabrication of the toluene and CCl_4-core PCF. The SC spectra in these liquid core PCFs are measured using commercial femtosecond lasers as pump laser sources.

1.2.2 Liquid Core Antiresonant Fiber for Optofluidic Applications

The interaction between the light and liquid medium has found various applications, e.g., sensors or optofluidic lasers. Most of the optofluidic applications is based on possibility to identify absorption bands or photoluminescence of compounds in liquids. The magnitude of the light-liquid interactions depends on the length of the liquid sample. For example, the linear absorption of light propagated inside the aqueous medium is determined according to Beer-Lambert law [63]:

$$\frac{P}{P_0} = 10^{-\varepsilon(\lambda)cL}, \tag{1.1}$$

where P and P_0 are transmitted powers through contaminated and pure water, respectively, $\varepsilon(\lambda)$ is the wavelength-dependent molar absorptivity of the analyte, c is the concentration of the absorbing substance, and L is the light-matter interaction length.

However, the liquid sample used in spectrophotometric techniques is typically investigated in glass or polymer cuvettes with a light path of 10 mm. As shown in Eq. (1.1), increasing the length of light-liquid interaction allows to detect the low concentration of an analyte [63,64]. Therefore, the use of hollow core fibers infiltrated with selected liquids as propagation media seems to be a perfect solution to extend the interaction length and enhance the sensitivity of the approach.

However, the majority of liquids including important solvents have a lower refractive index than that of silica in the NIR range. The refractive index of water and ethanol is around 1.33 and 1.36 in NIR. Water-based organic solutions have a refractive index that is slightly higher than the one of water [46], while that of silica is around 1.47. Therefore, the sophisticated design of liquid core PCFs with high air-fraction in the cladding region (higher than 70%) is necessary to maintain TIR light-guidance [55-57]. Such a fiber requires the complex process to selectively fill the core and simultaneously maintain air-glass cladding for TIR light guidance [55-57].

In another approach, hollow core PBG fibers can be used with low-index liquids. In this case, band-gap effects are maintained, however, the infiltration of liquids leads to decrease of refractive index contrast between core and cladding. Consequently, band-gap is shifted to the short wavelength band and its size is dramatically decreased [65-69]. For instance, heavy water filled hollow core PBG with Λ = 3 μm and d_{core} = 8.2 μm caused a shift from 1050 nm-centered transmission band to around 600 nm [65]. Also, the estimated initial bandwidth of 300 nm was narrowed to 170 nm (reduction by ~43%). The results in [66] presented the blueshifting of band-gap of a hollow core PBG fiber with Λ = 2.75 μm and d_{core} = 10 μm infiltrated with an aqueous solution of fructose. The transmission band centered at

1060 nm shifted to around 595 nm and its bandwidth decreased from 280 to 170 nm (by 39%) due to the liquid infiltration. The narrow bandwidth of transmission windows of liquid-filled PGB fibers causes limited ability to use liquid core PBG fiber for optofluidic applications. Moreover, a small size of the core of PBG fibers (a couple of micrometers) leads to a very time-consuming infiltration process, and the flow-rate of liquid through the fiber is hardly controllable.

As an alternative approach, AR fibers which have broad transmission bandwidth has been used for several optofluidic applications, as shown in Table 1.2. The relatively large size of the core (few tens micrometers) allows to control of the flow-rate of liquid through the core. Therefore, liquid-filled AR fibers have been already considered for application in chemical nanoreactors [70], sensors [32,63,71,72], and lasers [73]. For example, Unterkofler *et al.* have used the AR fiber with kagome lattice for online monitoring of photochemical reactions [70]. Liu *et al.* considered AR fiber as a sensor when one or more of the side capillaries are filled with ethanol [71]. In this case, a periodic attenuation of 1.1 dB/m in the spectral domain is observed in the NIR range. Due to the large thermo-optic coefficient of ethanol, Wei *et al.* predicted the shifting of the transmission window of ethanol-filled AR fiber via changing of temperature with a sensitivity of 2.48 nm/ºC [32]. Thus, the ethanol-filled AR fiber can be used for temperature sensing. Nissen *et al.* have shown that it is possible to detect selected pharmaceuticals at a very low concentration such as 0.1 μM by means of UV absorption spectrum [63]. Yu *et al.* have used AR fiber infiltrated with dye solvent as a gain medium for optofluidic laser [73]. In this case, the side capillaries can behave as a micro-ring resonator and microfluidic channel. Consequently, a stable optofluidic dye laser with a low threshold of 15.14 nJ/mm^2 was achieved.

Because of popular applications of liquid-filled AR fibers in optofluidic, the study of optical properties of liquid core AR fibers is necessary. The results of such works can be used as supporting for design and optimization the structure of liquid core AR fibers towards practical applications. Liu *et al.* have demonstrated the AR fiber infiltrated with water and ethanol [72]. Their preliminary results have shown that reduction of the contrast of refractive index between core and cladding does not dramatically decrease the size of transmission windows, as it took place in the case of PBG fibers.

In this dissertation, a part of the work is devoted to investigating the optical properties of AR fibers infiltrated with low-index liquids. The AR fibers used in this work are single-ring and double-ring tubular capillaries with different thicknesses. This work includes the theoretical and experimental investigation of the changing of spectral position of transmission windows for liquid-filled AR fibers. The numerical method is also used to estimate the losses of these fibers.

Table 1.2. Some applications of AR fibers infiltrated with low-index liquid.

#	AR fiber	Image of the fiber	Liquid	Application	Ref.	Year of Pub.
1	Kagome-structured hollow core-AR fiber	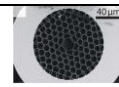	H_2OCbl (cyanocobalamin in aqueous solution)	photochemical nanoreactor	[70]	2012
2	Simplified hollow core AR fiber	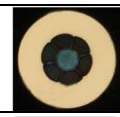	Alcohol	Temperature sensor	[71]	2013
3	Nodeless AR fiber	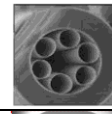	Water and Ethanol	Biological sensor	[72]	2017
4	Hexagonally shaped inner core AR fiber	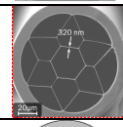	Pharmaceuticals	Pharmaceuticl Detection	[63]	2018
5	Nodeless AR fiber	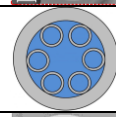	Series AA [66]	Temperature sensor	[32]	2019
6	Nodeless AR fiber	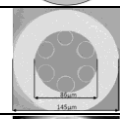	dye	Optofluidic laser	[73]	2018
7	Negative curvature AR fiber (made from Schott SF6)	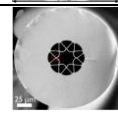	Toluene	Photochemical microreactor	[74]	2017
8	hollow core AR fiber with five functional concentric layers of capillaries	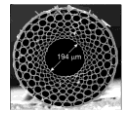	Mono bromonaphthalene containing magnetite nanoparticles	Optical bioimaging system	[75]	2019

1.3 Purpose and Thesis of the Work

This dissertation contains numerical and experimental studies on the optical properties of various liquid core PCFs. The investigated PCFs with different structures are fabricated at *Department of Glass, Institute of Electronic Materials Technology in Warsaw*. Then, the experiments to investigate the selected fibers are implemented at *Faculty of Physics, University of Warsaw* and *Faculty of Electronics and Information Technology, Warsaw University of Technology*. The work is aimed at verifying the following theses:

- **Thesis 1:** *Silica hollow core photonic crystal fibers infiltrated with liquids can offer flat all-normal dispersion regime in near-infrared range. The dispersion feature is compatible with central wavelengths of commercially available femtosecond lasers for supercontinuum generation applications.*
- **Thesis 2** *A broad spanning supercontinuum generation can be achieved in hollow core photonic crystal fibers with liquid infiltration and low peak power of input pulses*
- **Thesis 3:** *Antiresonant fibers infiltrated with low-index liquids offer broadband transmission windows and are suitable for optofluidic systems.*

In order to verify the **Thesis 1**, I use the conventional fusion splicer to collapse air-holes in the cladding region of the hollow core PCFs. The parameters of the fusion splicer, e.g., fusion time, were set up to obtain the desired results, i.e., collapsed air holes and an open core. The end of the fiber with collapsed cladding air-holes is immersed in the reservoir, which contains selected liquid and connects with the microfluidic pump system. The dispersion characteristics of investigated fibers are numerical calculated and then experimentally verified using Mach-Zehnder interferometer setup. The SCG in investigated PCFs are obtained under pumping with the commercial femtosecond laser as a pump source. The results of this work have been published in scientific journals (list of the author's publications) [A1, A2].

In order to verify the **Thesis 2,** two CCl_4-core PCFs with different structures, and thus different dispersion profiles, are used to measure SCG with a femtosecond laser as a pump source. The pump laser has central wavelength at 1560 nm and pulse duration of 90 fs. With flat near-zero dispersion profile in NIR range and high nonlinear refractive index of CCl_4, the investigated CCl_4-core PCFs offered broad SCG with relatively low input peak power compared to those of previous works on SCG in large mode area solid core fibers. These results have also been published in a scientific journal (list of the author's publications) [A3].

In order to verify the **Thesis 3**, I developed the experimental setup to observe the transmission window of AR fibers with different thicknesses of capillaries

infiltrated with water and ethanol. In this setup, the microfluidic pump system was used to keep the liquid inside the fiber. The transmission windows of the investigated AR fibers were measured in the wavelength range of 0.5 μm ÷ 1.1 μm. The numerical method was also used to estimate the spectral position and bandwidth of transmission windows and the losses of AR fibers. The results have been submitted for publication in a JCR journal [A9].

1.4 Structure of Dissertation and Author's Contribution

The dissertation is organized as follows:

- **Chapter 1** introduces the brief-history of optical fiber researches as well as state-of-the-art liquid core fibers for SCG and optofluidic applications.
- **Chapter 2** summarises the linear and nonlinear properties of optical fiber that are significant factors for SCG and optofluidic applications. The results in this chapter are based on the literature review.
- **Chapter 3** summarizes the linear and nonlinear properties of organic solvents and the original mechanisms for their nonlinear responses. The results in section 3.1 are based on the literature review. In section 3.2, I show the linear properties of commercial buffers and cell culture media (CCM). All measurements as well as result analysis presented in section 3.2 are my original contributions.
- **Chapter 4** includes the numerical and experimental investigation for the linear properties of toluene and CCl_4-core PCFs with different structures. The process to fabricate liquid core PCFs as well as the experimental system to measure the dispersion of these fibers are presented here.

  All simulation and experimental works as well as result analysis presented in this chapter is my original contribution.
- **Chapter 5** presents all-normal dispersion SCG in toluene-core PCF with femtosecond laser as a pump source. It includes numerical simulation of pulse propagation in this fiber and experimental setup to verify the SCG.

  All linear and nonlinear simulations, verification experiments, and result analysis presented in this chapter are my original contribution.
- **Chapter 6** presents all-normal and anomalous dispersion SCG in two CCl_4-core PCFs with different structures. The numerical calculation of the first-order coherence to estimate the coherent characteristics of SCG in the CCl_4-core PCFs is also showed here.

  All simulations, experimental works, and result analysis presented in this chapter are my original contribution.
- **Chapter 7** is devoted to investigating the optical properties of large mode area solid-core PCF dedicated to coupling with liquid core PCFs for the all-fiber SCG system. The developed PCF is numerically analyzed and

experimentally verified for dispersion, nonlinearity, and single mode operation in NIR range. The coupling efficiency between this fiber and the liquid core PCFs is also numerically estimated.

The simulation to character dispersion and pulse propagation in proposed fiber as well as experimental works presented in this chapter are my original contribution. I also contribute to the calculation of bending loss of the fiber.

- **Chapter 8** presents the transmission windows of AR fibers infiltrated with water and ethanol in NIR range. The losses of these fibers are numerically estimated. The ability to use these fibers for optofluidic applications is also discussed.

  All experimental works and result analysis in this chapter are my original contribution. I also participate in the numerical calculation of losses of test fibers.

- **Chapter 9** concludes the dissertation and show an outlook for the future works based on the results shown in this dissertation.

1.5 List of Publication

The results of the research described in this thesis have been disseminated in the following forms:

Publications in JCR journals

[A1] Van Thuy Hoang, Rafal Kasztelanic, Alicja Anuszkiewicz, Grzegorz Stepniewski, Adam Filipkowski, Slawomir Ertman, Dariusz Pysz, Tomasz Wolinski, Khoa Dinh Xuan, Mariusz Klimczak, and Ryszard Buczynski, "*All-normal dispersion supercontinuum generation in photonic crystal fibers with large hollow cores infiltrated with toluene*," Optical Material Express 8(11), 3568-3582 (2018).

[A2] Van Thuy Hoang, Rafal Kasztelanic, Adam Filipkowski, Grzegorz Stępniewski, Dariusz Pysz, Mariusz Klimczak, Sławomir Ertman, Van Cao Long, Tomasz R. Woliński, Marek Trippenbach, Khoa Dinh Xuan, Mateusz Śmietana, and Ryszard Buczyński, "*Supercontinuum generation in an all-normal dispersion large core photonic crystal fiber infiltrated with carbon tetrachloride*," Optical Material Express 9(5), 2264-2278 (2019).

[A3] Van Thuy Hoang, Rafal Kasztelanic, Grzegorz Stępniewski, Khoa Dinh Xuan, Van Cao Long, Marek Trippenbach, Mariusz Klimczak, Ryszard Buczyński, Jacek Pniewski, "*Femtosecond supercontinuum generation around 1560 nm in hollow core photonic crystal fibers filled with carbon tetrachloride,*" Applied Optics 59(12), 3720-3725 (2020).

[A4] Van Thuy Hoang, Bartłomiej Siwicki, Marcin Franczyk, Grzegorz Stępniewski, Hieu Le Van, Van Cao Long, Mariusz Klimczak, Ryszard Buczyński, *"Broadband low-dispersion low-nonlinearity photonic crystal fiber dedicated to near-infrared high-power femtosecond pulse delivery,"* Optical Fiber Technology 42, 119-125 (2018).

[A5] Van Thuy Hoang, Grzegorz Stepniewski, Karolina H. Czarnecka, Rafał Kasztelanic, Van Cao Long, Khoa Dinh Xuan, Liyang Shao, Mateusz Smietana, and Ryszard Buczynski, "*Optical Properties of Buffers and Cell Culture Media for Optofluidic and Sensing Applications*," Applied Sciences 9(6), 1145 (2019).

[A6] Chu Van Lanh, Van Thuy Hoang, Van Cao Long, Krzysztof Borzycki, Khoa Dinh Xuan, Vu Tran Quoc, Marek Trippenbach, Ryszard Buczyński and Jacek Pniewski, "*Optimization of optical properties of photonic crystal fibers infiltrated with chloroform for supercontinuum generation*," Laser Physics 27(7), 075107 (2019).

[A7] Lanh Chu Van, Van Thuy Hoang, Van Cao Long, Krzysztof Borzycki, Khoa Dinh Xuan, Vu Tran Quoc, Marek Trippenbach, Ryszard Buczyński, and Jacek Pniewski, "*Supercontinuum generation in photonic crystal fibers infiltrated with nitrobenzene*," Laser Physics 30(3), 035105 (2020).

[A8] Trung Le Canh, Van Thuy Hoang, Hieu Le Van, Dariusz Pysz, Van Cao Long, Thuan Bui Dinh, Dung Tien Nguyen, Quang Ho Dinh, Mariusz Klimszak, Rafal Kasztelanic, Jacek Pniewski, Ryszard Buczynski, and Khoa Xuan Dinh, "*Supercontinuum generation in all-normal dispersion suspended core fiber infiltrated with water*," Optical Material Express 10(7), 1733-1748 (2020).

[A9] Van Thuy Hoang, Dominik Dobrakowski, Grzegorz Stepniewski, Rafal Kasztelanic, Dariusz Pysz, Khoa Xuan Dinh, Mariusz Klimczak, Mateusz Smietana, and Ryszard Buczynski, "*Antiresonant fibers with single and double ring of capillaries for optofluidic applications*," Optics Express, submitted (August, 2020).

Conference presentations

[B1] Paulina Stafiej, Adam Filipkowski, Dariusz Pysz, Ryszard Stepien, Van Thuy Hoang, Andrzej Kazmierczak, Jaroslaw Cimek, Andrew Waddie, Marisz Klimczak, Ryszard Piramidowicz, Mohamad R.Taghizadeh and Ryszard Buczynski, "*Nanostructured microlenses for coupling between single mode fiber and channel waveguides*", Conference on Optical fibers and their applications (17th). Bialystok- Suprasl, Poland (2017).

[B2] Van Thuy Hoang, Rafal Kasztelanic, Alicja Anuszkiewicz, Grzegorz Stepniewski, Adam Filipkowski, Slawomir Ertman, Van Cao Long, KhoaDinh Xuan, and Ryszard Buczynski, "*Dispersion measurement of photonic crystal*

*fiber infiltrated with toluene,"*20th International Conference on Transparent Optical Networks, 1-5 of July 2018, Bucharest, Romania.

[B3] Van Thuy Hoang, Rafal Kasztelanic, Alicja Anuszkiewicz, Grzegorz Stepniewski, Adam Filipkowski, and Ryszard Buczynski, "*Supercontinuum generation in photonic crystal fiber infiltrated with liquid,"* XIV International Workshop Nonlinear Optics Application (NOA), 23-26 of May 2018 in Wroclaw (Poland).

[B4] Van Thuy Hoang, Rafal Kasztelanic, Adam Filipkowski, Mariusz Klimczak, Dariusz Pysz, Grzegorz Stepniewski, Khoa Dinh Xuan, Ryszard Buczynski, "*Photonic crystal fiber infiltrated with carbon tetrachloride for supercontinuum generation*,"The 2019 Conference on Laser and Electro-Optics/Europe and the European Quantum Electronics Conference (CLEO®/Europe-EQEC), 23-27 June in Munich (Germany).

2 Theory of Light Propagation in Photonic Crystal Fiber

This chapter presents the optical properties of PCFs including mechanism of light-guidance, dispersion characteristics, and nonlinear phenomena with ultra-short pulse lasers as pump sources. Due to the design flexibility, for practical applications, e.g., SCG, the dispersion of PCFs can be modified by changing their geometry. The modeling of light propagation is also presented in this chapter, including the nonlinear phenomena responsible for spectral broadening when the pulse propagates in the fiber.

2.1 Guiding Mechanism in Photonic Crystal Fiber

A solid core PCF is made by stacking capillaries around a solid rod in the preform fabrication process. The air-holes in the cladding region are located along its entire length. As a result, the average refractive index of the cladding region is lower than that of core. Thus, most of the solid core PCFs work according to TIR mechanism.

Figure 2.1 shows the hexagonal lattice of solid core PCF with the diameter d of air-holes in the cladding region, and lattice constant Λ. The core diameter d_{core} is determined through d, and Λ as given in Eq (2.1):

$$d_{core} = 2\Lambda - d. \tag{2.1}$$

The confinement of the light in the core depends on the trade-off between microstructure parameters and a refractive index of fiber materials. In some special cases, as shown in Figure 2.2, there is no light guided in the solid core of the PCF.

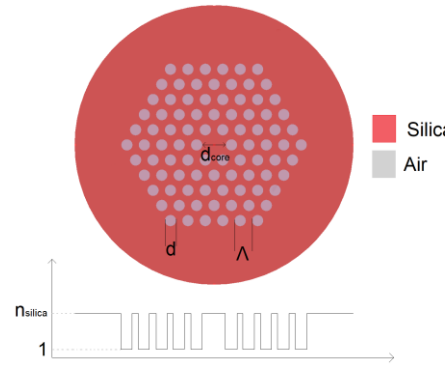

Figure 2.1. The schematic representation of solid core PCF.

In the solid core PCF with a hexagonal lattice, the air-filling fraction (f_{air}) is calculated as:

$$f_{air} = \left(\frac{\pi}{2\sqrt{3}}\right)\left(\frac{d}{\Lambda}\right)^2 \tag{2.2}$$

Figure 2.2 shows the propagation diagram for hexagonal shape in silica PCF with an air-filling fraction of 45% [76]. The black area C_4 is the region where the light is evanescent in every region of the fiber. In area C_1, the light is free to propagate in every region of the fiber while area C_2 shows the light propagating only in the photonic crystal and the core. Propagation of modes occur in area C_3, where the light is confined in the core and the light in the cladding is evanescent due to the reduction of an average of the refractive index of the cladding. The finger-shaped black regions show the band-gaps, which is the light free to propagate in any medium, but it is blocked from penetrating the cladding by band-gap mechanism [76].

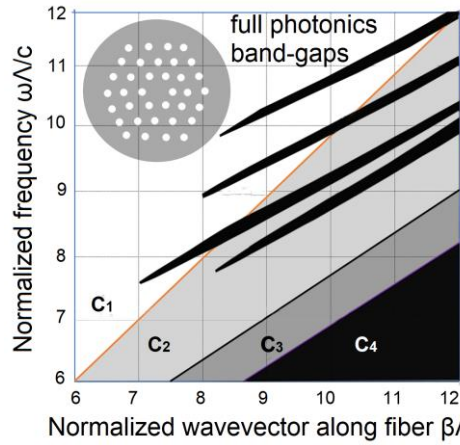

Figure 2.2. The propagation diagram for a hexagonal lattice solid core PCF with an air-filling fraction of 45%. The orange line corresponds to the air line [76].

The liquid core PCF for SCG in the following chapters, which is made from silica hollow core PCF selectively filled with liquid in the area of the core only. Typically, the selected nonlinear liquid has a higher refractive index than that of silica, thus the liquid core PCF for SCG works according to TIR mechanism as a solid core PCF.

In the case of hollow core PCFs, the core has a refractive index that is close to 1 and is lower than that of cladding. Thus, this fiber can not guide the light by TIR mechanism. However, the light can be guided in the core of hollow core PCF by band-gaps mechanism [76,77]. Figure 2.3 shows the propagation diagram of honeycomb lattice hollow core PBG fiber. In S_1 and S_2 regions, the cladding supports

propagating mode. The black region below the light line shows the band-gaps regions, where the light is guided in the core of the fiber.

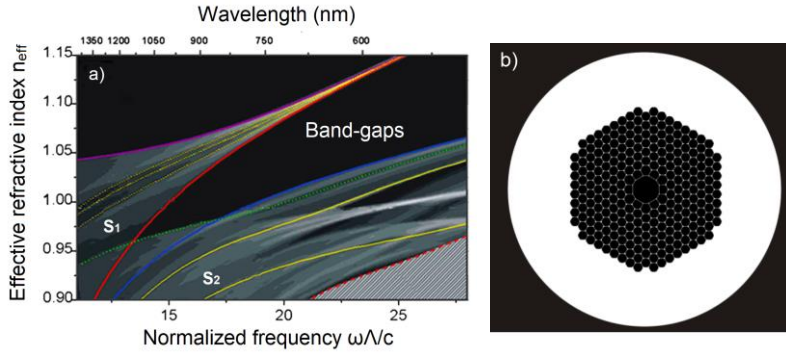

Figure 2.3. The numerically calculated density of states for hollow core PCF with the honeycomb lattice [42]. The commercial band-gap PCF with honeycomb lattice [78], the black and white colors correspond to air and silica, respectively.

In the case of AR fibers, antiresonance has a role to inhibit coupling between core and cladding mode. An example to consider the antiresonant mechanism is a slab waveguide, as shown in Figure 2.4. *W* and *t* are the sizes of the core and thickness of layer glass, respectively. n_0 and n_1 are a refractive index of air and the glass, where $n_0 < n_1$. k_L and k_T are longitudinal and transverse wave vector in the glass region, respectively.

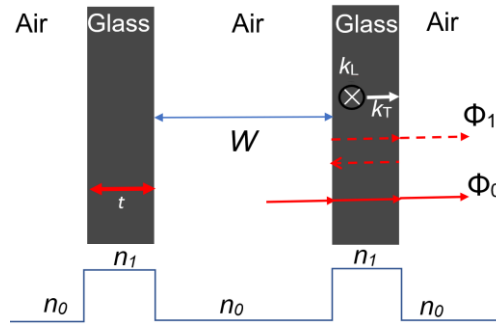

Figure 2.4. Cross-section and index profile of an M-type slab waveguide [79].

When *W* is much larger than λ, longitudinal k_L is approximate to $k_0 n_0$, and transverse wave vector k_T is approximate to $k_0\sqrt{n_1^2 - n_0^2}$, where $k_0 = 2\pi/\lambda$ is wave number in the air.

The different phase between the light passing through the glass slab with and without additional refraction is given in Eq (2.3):

$$\Delta\Phi = \Phi_1 - \Phi_0 = 2t\,k_0\sqrt{n_1^2 - n_0^2}. \tag{2.3}$$

The resonance condition is when $\Delta\Phi = 2m\pi$, thus wavelength λ_m of the light that is not confined in the waveguide is given in Eq (2.4):

$$\lambda_m = \frac{2t}{m}\sqrt{n_1^2 - n_0^2}, \quad (m = 1,2.3\ldots) \tag{2.4}$$

As an example, the results of measuring transmission windows of the AR fiber that has typical the structure as shown in Figure 2.5. It includes the cladding with the number of capillaries *p*, and thickness of capillaries *t*. AR fiber shown in Figure 2.5(a) has p = 7, t = 1.884 µm and d_{core} = 64.8 µm. The schematic setup for transmission window measurement is shown in Chapter 8. The non-transmission wavelength is estimated by Eq (2.4). The spanning spectra of the transmission windows depend on the thickness of the capillaries *t* and the refractive index of the material fiber [79]. In the case of t = 1.884 µm, the non-transmission wavelengths according to Eq (2.4) in NIR are 572 nm, 665 nm, 797 nm, 990 nm with m = 7,6,5,4, respectively. These calculated results are in good agreement with the experimentally observed spectrum of the AR fiber in NIR range (from 500 nm to 1100 nm), as shown in Figure 2.5(c). In this dissertation, the transmission windows and losses of AR fibers are also numerically simulated using FEM method (COMSOL Multiphysics, Wave optics module).

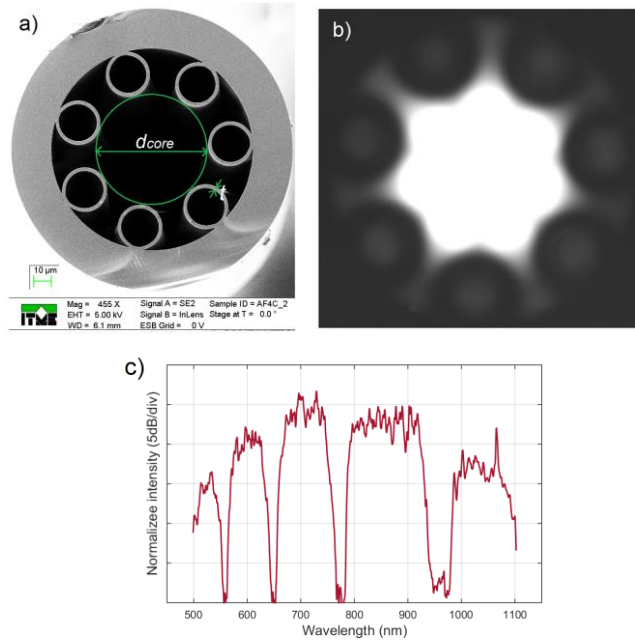

Figure 2.5. SEM image of nested AR fiber (a). The light guided inside AR fiber (b) and transmission windows of the output spectrum are also shown (c).

2.2 Chromatic Dispersion

The mode propagation constant β is one of the key parameters to describe the light propagation in the optical fiber. The value of β is different for individual modes and depends on the frequency (wavelength). The β would affect the pulse propagating in the fiber and contribute to spectral broadening. The dispersion relationship of the propagation constant $\beta(\omega)$ can be developed into the Taylor series around the central frequency ω_0 to the form as given in Eq (2.5) [80]:

$$\beta(\omega) = n(\omega)\frac{\omega}{c} = \beta_0 + \frac{\partial\beta}{\partial\omega}(\omega-\omega_0) + \frac{1}{2}\frac{\partial^2\beta}{\partial\omega^2}(\omega-\omega_0)^2 + \frac{1}{6}\frac{\partial^3\beta}{\partial\omega^3}(\omega-\omega_0)^3 + \ldots \tag{2.5}$$

The definition of β_m is given in Eq (2.6):

$$\beta_m = \left(\frac{d^m\beta}{d\omega^m}\right)_{\omega=\omega_0} \quad \text{(m=1,2,3...).} \tag{2.6}$$

The parameters β_1 is knows as inverse of group velocity [80], as given in Eq (2.7):

$$\beta_1 = \left.\frac{\partial\beta}{\partial\omega}\right|_{\omega_0} = \frac{1}{v_g} \tag{2.7}$$

The relation between v_g and group refractive index N_g is given in Eq (2.8) [80]:

$$v_g = \frac{c}{N_g} = \left[\frac{1}{c}\left(n + \omega\frac{dn}{d\omega}\right)\right]^{-1} \tag{2.8}$$

where n is phase refractive index of propagation medium.

From Eq (2.5) and (2.8), the parameters β_1 and β_2 are calculated in relation to refractive index n and their derivative, given in Eq (2.9) and (2.10) [80]:

$$\beta_1 = \left.\frac{\partial\beta}{\partial\omega}\right|_{\omega_0} = \frac{1}{v_g} = \frac{1}{c}\left(n + \omega\frac{dn}{d\omega}\right), \tag{2.9}$$

$$\beta_2 = \left.\frac{\partial^2\beta}{\partial\omega^2}\right|_{\omega_0} = \frac{1}{c}\left(2\frac{dn}{d\omega} + \omega\frac{d^2n}{d\omega^2}\right) = \frac{\lambda^3}{2\pi c^2}\frac{d^2n}{d\lambda^2} \tag{2.10}$$

As shown in Eq (2.9) and (2.10), β_1 is in relation to the group velocity of the pulse and β_2 represents the dispersion of the group velocity. The unit of β_1 and β_2 are $\left[\frac{ps}{km}\right]$ and $\left[\frac{ps^2}{km}\right]$, respectively. In telecommunications, the dispersion D is commonly used in the optical fiber literature in place of β_2. It is related to β_2 in relation given in Eq (2.11) [80]:

$$D = -\frac{2\pi c}{\lambda^2}\beta_2 = -\frac{\lambda}{c}\frac{d^2n}{d\lambda^2} \quad \left[\frac{\text{ps}}{\text{nm}\cdot\text{km}}\right]. \tag{2.11}$$

It is important to distinguish two different D regime. The regime with $D < 0$ ($\beta_2 > 0$) is normal dispersion, it means that the red components travel faster than the blue. In contrast, $D > 0$ ($\beta_2 < 0$) is an anomalous dispersion regime, and the red components travel slower than the blue. The wavelength, where $D = 0$, is known as zero-dispersion wavelength (ZDW).

The D of optical fiber is not only provided by material dispersion ($D_m(\lambda)$) of the propagation medium, but also by waveguide dispersion ($D_g(\lambda)$) that depends on the geometrical structures of the fiber. As shown in Figure (2.6), D is approximate to the sum of $D_g(\lambda)$ and $D_m(\lambda)$ as given in Eq(2.12) [51]:

$$D \approx D_g(\lambda) + D_m(\lambda), \tag{2.12}$$

The origin of $D_g(\lambda)$ can be understood by considering that the propagated light has a frequency-dependent distribution of propagation constant. $D_g(\lambda)$ depends on the geometrical structure of the fiber and guided mode. $D_g(\lambda)$ occurs even if the fiber material is non-dispersive ($n(\lambda)$ = constant). D_m originates from the dependence of the refractive index of fiber material on the wavelength, $n = n(\lambda)$.

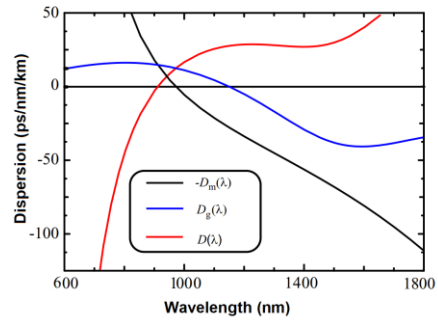

Figure 2.6. The D_g, $-D_m$, and D of the fundamental mode of a PCF [51].

Therefore, the D can optimize by the modification of photonic parameters, i.e., Λ and filling factor f ($f = d/\Lambda$). In general discussion of D in PCF, it is useful to consider two special cases: (i) $f \rightarrow 1$, (ii) $f < 0.8$. In the first case, the PCF is like a strand of silica completely surrounded by air. The average refractive index of the cladding region $n_{clad} \rightarrow 1$. The D characteristics of the fundamental mode in such fibers with various core diameter d_{core} from 0.5 μm to 4 μm are shown in Figure 2.7. With the large d_{core}, the D of a strand of silica in the air is approximate to that of silica. When d_{core} reduces, the value of D in the anomalous regime will increase, while that in normal regime will decrease. Such fibers have typically two ZDWs, first one (λ_1) is in the investigated range of 400 nm ÷ 1600 nm, and the larger one (λ_2) is in NIR. The decreasing of core diameter leads to both ZDWs shift to short wavelengths. If the core diameter is further decreased, the maximum amount of D in the anomalous regime would decrease, and eventually, D would be in normal regime through the

entire spectral range. The shortest wavelength at which anomalous *D* can be obtained in silica fibers is around 500 nm.

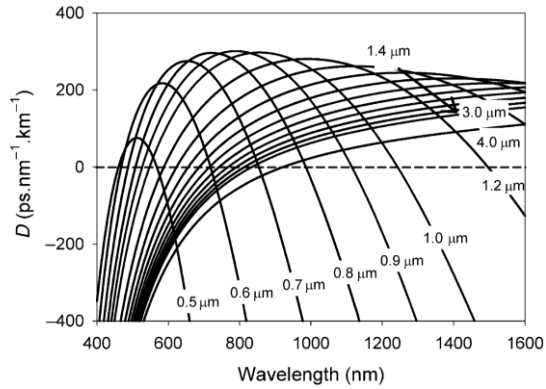

Figure 2.7. *D* of the fundamental mode in with $f \approx 1$ and d_{core} varies from 0.5 μm to 4 μm [30].

In the case of $f < 0.8$, when fiber has a fixed core diameter, the extra degree of freedom for modifying the *D* is offered by changing the diameter of air-hole in the cladding region. The d_{core} of a PCF is typically calculated by Eq (2.1). Figure 2.8 shows *D* of PCF with fixed d_{core} = 2 μm, and $f = 0.1 \div 0.99$. If f =0.99, the *D* is essentially the same as a strand of silica in the air of the same core diameter. Even as *f* reduces to 0.8, the *D* still has the general form of *D* of a silica strand model. The further decrease of *f* causes the decrease of amount of maximum *D* in the anomalous regime and the blue-shifting of the ZDW (λ_2) toward NIR range.

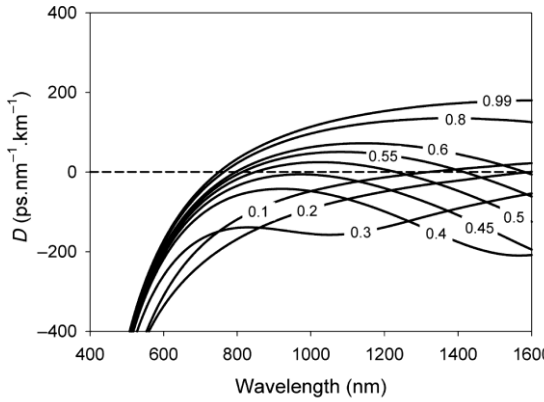

Figure 2.8. *D* of fibers with fixed d_{core} = 2 μm, f varies from 0.1 to 0.99 [30].

When f < 0.4, the difference of refractive index between cladding region and core is reduced, and such silica fibers can offer only one guided mode, independent of wavelength, so-called endlessly single mode fibers [81]. If f < 0.1, the waveguide does not confine the light very well in the core region, and the D is similar to that of bulk silica.

Figure 2.9 shows the D of fiber for fixed f = 0.4 and various d_{core}. The D is all-normal in investigated wavelength range if d_{core} < 2.5 μm. Increasing d_{core} leads to appear of the anomalous regime. The D is similar to that is bulk silica when d_{core} > 6 μm.

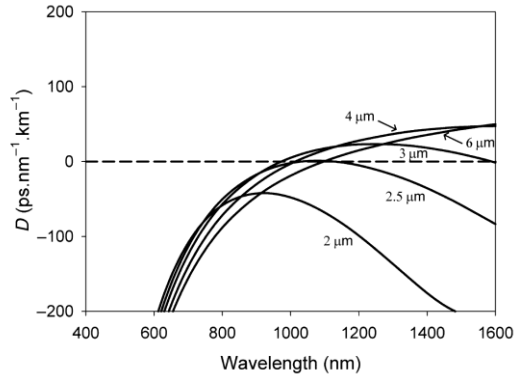

Figure 2.9. The D of fibers with f =0.4 and d_{core} varies from 2 μm to 6μm [30].

The flexibility of design to modify D of PCF is its advantage. Therefore, PCFs have found numerous applications all over the world, starting from the telecommunication to metrology, spectroscopy, microscopy, astronomy, micromachining, biology, sensor, and laser.

2.3 Modelling of Pulse Propagation

2.3.1 The Generalized Nonlinear Schrödinger Equation

The propagation of light in a cylindrical fiber is governed by Maxwell's equations. In the International System of Units (SI), these equations are [82]:

$$\nabla \times \boldsymbol{E} = -\frac{\partial \boldsymbol{B}}{\partial t}, \tag{2.13}$$

$$\nabla \times \boldsymbol{H} = \boldsymbol{J} + \frac{\partial \boldsymbol{D}}{\partial t}, \tag{2.14}$$

$$\nabla \cdot \boldsymbol{D} = \rho_f, \tag{2.15}$$

$$\nabla \cdot \boldsymbol{B} = 0, \tag{2.16}$$

where $\boldsymbol{E}$ and $\boldsymbol{D}$ are electric field, electric flux density vector, respectively, $\boldsymbol{H}$ and $\boldsymbol{B}$ are magnetic field and magnetic flux vector, respectively, $\boldsymbol{J}$ and ρ_f are current density vector and charge density, respectively. If optical fiber made from non-metallic materials, no free charge exits, and thus, $\boldsymbol{J}=0$ and $\rho_f=0$. The relations between electric, magnetic field vector and the flux vector is given in Eq (2.17), and (2.18):

$$\boldsymbol{D}=\varepsilon_0\boldsymbol{E}+\boldsymbol{P}, \tag{2.17}$$

$$\boldsymbol{B}=\mu_0\boldsymbol{H}+\boldsymbol{M}, \tag{2.18}$$

where ε_0 is the vacuum permittivity, μ_0 is vacuum permeability, $\boldsymbol{P}$ and $\boldsymbol{M}$ are the induced electric and magnetic polarization, respectively. The fiber material is typically a nonmagnetic medium, thus $\boldsymbol{M}$ = 0. Substituting Eq (2.17), (2.18) into Eq (2.13) and using Eq (2.14 ÷2.16), one can eliminate $\boldsymbol{B}$ and $\boldsymbol{D}$ in favor of $\boldsymbol{E}$ and $\boldsymbol{P}$, and obtain:

$$\nabla\times\nabla\times\boldsymbol{E}=-\frac{1}{c^2}\frac{\partial^2\boldsymbol{E}}{\partial t^2}-\frac{1}{\mu_0}\frac{\partial^2\boldsymbol{P}}{\partial t^2}, \tag{2.19}$$

where $c=1/\sqrt{\varepsilon_0\mu_0}$ is the speed of light in vacuum.

The $\boldsymbol{P}$ consists of two parts - linear $\boldsymbol{P_L}$ and nonlinear $\boldsymbol{P_{NL}}$. These parts relate to the electric field as a function of position $\boldsymbol{r}$ and time t [80,83], that are given in Eq (2.20), and (2.21):

$$\boldsymbol{P_L}=\varepsilon_0\int_{-\infty}^{+\infty}\chi^{(1)}(t-t_1)\boldsymbol{E}(\boldsymbol{r},t_1)\,dt_1, \tag{2.20}$$

$$\boldsymbol{P_{NL}}=\varepsilon_0\iiint\chi^{(3)}(t-t_1,t-t_2,t-t_3)\times\boldsymbol{E}(\boldsymbol{r},t_1)\boldsymbol{E}(\boldsymbol{r},t_2)\boldsymbol{E}(\boldsymbol{r},t_3)\,dt_1dt_2dt_3, \tag{2.21}$$

where $\chi^{(1)}$, and $\chi^{(3)}$ are first and third-order susceptibility, respectively.

Eq (2.19) is rewritten as given in Eq (2.22):

$$\nabla^2\boldsymbol{E}-\frac{1}{c^2}\frac{\partial^2\boldsymbol{E}}{\partial t^2}=\mu_0\frac{\partial^2\boldsymbol{P_L}}{\partial t^2}+\mu_0\frac{\partial^2\boldsymbol{P_{NL}}}{\partial t^2}. \tag{2.22}$$

In the case of $\boldsymbol{P_{NL}}$ originated only from the response of the propagation medium regarded as instantaneous. The absolute of P_{NL} is give in Eq (2.23) [80]:

$$\begin{aligned}P_{NL}&=\frac{3}{4}\varepsilon_0\chi^{(3)}\left|E(\boldsymbol{r},t)\right|^2E(\boldsymbol{r},t)\\&=\varepsilon_0\varepsilon_{NL}E(\boldsymbol{r},t)\end{aligned} \tag{2.23}$$

in the frequency domain, Eq (2.22) is written as given in Eq (2.24):

$$\nabla^2\tilde{\boldsymbol{E}}(\boldsymbol{r},\omega)+n(\omega)\frac{\omega^2}{c^2}\tilde{\boldsymbol{E}}(\boldsymbol{r},\omega)=0, \tag{2.24}$$

where $\tilde{\boldsymbol{E}}(\boldsymbol{r},\omega)$ is the Fourier transform of $\boldsymbol{E}(\boldsymbol{r},t)$ by definition in Eq (2.25):

$$\tilde{\boldsymbol{E}}(\boldsymbol{r},\omega)=\int_{-\infty}^{\infty}\boldsymbol{E}(\boldsymbol{r},\mathrm{t})\exp(i\omega t)\,dt, \tag{2.25}$$

and

$$n(\omega)=n_0+n_2 I. \tag{2.26}$$

n_0 in Eq (2.26) is the refractive index of the propagation medium, I is the intensity of light propagated in the fiber, and n_2 is the nonlinear refractive index. Both refractive indices can be determined from first and third-order susceptibility as given in Eq (2.27) and (2.28) [80]:

$$n_0(\omega)=1+\frac{1}{2}\mathrm{Re}\left[\tilde{\chi}^{(1)}(\omega)\right], \tag{2.27}$$

$$n_2=\frac{3}{8n_0}\tilde{\chi}^{(3)}(\omega) \tag{2.28}$$

where $\tilde{\chi}^{(1,3)}(\omega)$ is the Fourier transform of $\chi^{(1,3)}(t)$.

Using the method of separation of variables $\tilde{E}$ can be rewritten in the form, according to Eq (2.29) [80]:

$$\tilde{E}(\boldsymbol{r},\omega-\omega_0)=MF(x,y)\tilde{A}(z,\omega-\omega_0)exp(-i\beta_0 z), \tag{2.29}$$

where M is normalization constant, $\tilde{A}(z,\omega-\omega_0)$ is the slowly varying envelope along the fiber depending on the frequency ω, and β_0 is the first Taylor coefficient of the propagation constant. Eq (2.24) is written in the form:

$$\frac{\partial^2 F}{\partial x^2}+\frac{\partial^2 F}{\partial y^2}+\left(\varepsilon(\omega)k_0^2-\tilde{\beta}\right)F=0, \tag{2.30}$$

$$2i\beta_0\frac{\partial\tilde{A}}{\partial z}+\left(\tilde{\beta}^2-\beta_0^2\right)\tilde{A}=0, \tag{2.31}$$

where $\tilde{A}(z,\omega)$ is a slowly varying function of z, ε is the dielectric constant that can be approximated as given in Eq (2.32) with $\tilde{\alpha}$ is the attenuation of fiber:

$$\varepsilon\approx n_0^2+2n_0n_2I+\frac{i\tilde{\alpha}}{2k_0}=n_0^2+2n_0\Delta n \tag{2.32}$$

F(x,y) is a function for modal distribution on the x- and y-axis. In the first-order perturbation theory, *F(x,y)* remains unchanged, however, the eigenvalue is given according to Eq (2.33) [80]:

$$\tilde{\beta}(\omega)=\beta(\omega)+\Delta\beta, \tag{2.33}$$

where

$$\Delta\beta=\frac{k_0\int\int_{-\infty}^{\infty}n_2 I\left|F(x,y)\right|^2\,dxdy}{\int\int_{-\infty}^{\infty}\left|F(x,y)\right|^2\,dxdy} \tag{2.34}$$

In first-order in perturbation, $\tilde{A}(z,\omega)$ can be written as given in Eq (2.35) [80]:

$$\frac{\partial \tilde{A}}{\partial z} = i\left[\beta(\omega) + \Delta\beta - \beta_0\right]\tilde{A} \tag{2.35}$$

Substituting the expansion of β (ω) in a Taylor series in Eq (2.5) to Eq (2.35). The equation to determine $\tilde{A}(z,\omega)$ is given in Eq (2.36):

$$\frac{\partial \tilde{A}}{\partial z} = i\left[\sum_{k=1}^{\infty}\frac{1}{k!}\beta_k(\omega-\omega_0)^k + \Delta\beta\right]\tilde{A} \tag{2.36}$$

The time domine of *A(z,t)* take the inverse Fourier transform $\tilde{A}(z,\omega)$ by using:

$$A(z,t) = \frac{1}{2\pi}\int_{-\infty}^{\infty}\tilde{A}(z,\omega-\omega_0)\exp\left[-i(\omega-\omega_0)t\right]d\omega. \tag{2.37}$$

During the Fourier transform, the term $(\omega-\omega_0)$ is replaced by $i\frac{\partial}{\partial t}$. Eq (2.36) is written in time domain - so-called Nonlinear Schrödinger Equation:

$$\frac{\partial A}{\partial z} + \sum_{k=1}^{\infty}\frac{(i)^{k-1}}{k!}\beta_k\frac{\partial^k A}{\partial t^k} + \frac{\alpha}{2}A = i\gamma|A|^2 A \tag{2.38}$$

where γ is the nonlinear coefficient given by the following manner with A_{eff} and n_2 is the nonlinear refractive index :

$$\gamma = \frac{n_2\omega_0}{cA_{eff}} \tag{2.39}$$

Eq (2.38) describes the pulse propagation with the nonlinear part originated only from the instantaneous response. However, it does not include all of the third-order nonlinear effects, such as third-harmonic generation, four-wave mixing, and Raman scattering [80]. These effects can be induced by assuming the form of third-order susceptibility as given in Eq (2.40) [80,84]:

$$\chi^{(3)}(t-t_1,t-t_2,t-t_3) = \chi^{(3)}R(t-t_1)\delta(t-t_2)\delta(t-t_3), \tag{2.40}$$

where *R*(*t*)is the nonlinear response function normalized in a form similar to the delta function [80,84]:

$$\int_{-\infty}^{\infty}R(t)dt = 1. \tag{2.41}$$

Using Eq (2.40) and Eq (2.23), the generalized nonlinear Schrödinger equation (GNLSE) is given according to Eq (2.42):

$$\frac{\partial A}{\partial z} + \frac{\alpha}{2}A + \sum_{k=1}\frac{(i)^{k-1}}{k!}\frac{\beta_k\partial^{(k)}A(z,t)}{\partial t^k} = i\gamma\left(1+\frac{i}{\omega_0}\frac{\partial}{\partial t}\right)\left(A(z,t)\int_{-\infty}^{\infty}R(t')\left|A(z,t-t')\right|^2 dt'\right), \tag{2.42}$$

The left-hand term of Eq (2.42) describes the linear effects, e.g., dispersion, losses on the pulse propagation. The right-hand term shows nonlinear effects. Numerical modelling based on the GNLSE is used in this thesis to simulate the

complex process of pulse propagation in the fibers of ultra-short input pulses. These numerical results then will be verified experimentally.

2.3.2 Numerical Method

In order to solve GNLSE (Eq. 2.42) for investigated fiber, the symmetry split-step Fourier method (SSFM) is used. In general, linear and nonlinear properties act simultaneously during pulse propagation along the fiber. In the case of SSFM, the total path of the pulse propagation in the fiber is divided into very short sections with a length of *h*. In each sample with *h* length, the linear operation ($\hat{L}$) and nonlinear operation ($\hat{N}$) can be assumed to act independently.

The solution if the linear operation acts alone:

$$\frac{\partial A_L}{\partial z} = \hat{L}A_L \leftrightarrow A_L(z+h,t) = \exp\left(h\hat{L}\right)A_L(z,t) \tag{2.43}$$

In general, the nonlinear step has to be solved by numerical integration due to z-dependence as five in Eq (2.44) [80]:

$$\frac{\partial A_N}{\partial z} = \hat{N}A_N \leftrightarrow A_N(z+h,t) = \int_z^{z+h} \exp\left(h\hat{N}\right)A_N(z,t)\,dz \tag{2.44}$$

In SSFM, the $A(z+h,t)$ is a result of the process (i) half a linear step, (ii) the nonlinear step, and (iii) linear half-step, as presented in Eq (2.45):

$$A(z+h,t) = \left[\exp\left(\frac{h}{2}\hat{L}\right)\right]\left[\int_z^{z+h} \exp\left(h\hat{N}\right)A_N(z,t)\,dz\right]\left[\exp\left(\frac{h}{2}\hat{L}\right)\right]A(z,t) \tag{2.45}$$

The linear operation including *D*, attenuation, which is calculated by commercially available Lumerical Mode Solution software and represented in the frequency domain, would be transformed into the time domain by Fourier transform. In this dissertation, simulations of pulse propagation in investigated PCF by SSFM are carried out by using the MATLAB code provided in [30] and modified by *dr hab. Mariusz Klimczak* from Faculty of Physics, University of Warsaw (Poland). The numerical results for nonlinear phenomena in the investigated fibers would be used as a reference to be compared with experimental results.

2.4 Nonlinear Phenomena

This section presents some significant nonlinear phenomena occurring in optical fiber with ultra-short input pulses. These nonlinear mechanisms are the main contributions to spectral broadening for SCG applications.

2.4.1 Self-Phase Modulation

Self-Phase Modulation (SPM) is the first nonlinear phenomena occur early in propagation length in optical fiber and induce spectral broadening. SPM originates from the self-induced nonlinear phase shift in the form [80]:

$$\Phi_{NL}(L,t) = |U(0,t)|^2 \frac{L_{eff}}{L_{NL}}, \tag{2.46}$$

where $U(0,t)$ normalized amplitude at beginning of propagation length (z = 0), the relation between $U(z,t)$ and $A(z,t)$ is given in following form with P_0 is peak power of the input pulse:

$$A(z,t) = \sqrt{P_0}\exp\left(\frac{-\alpha z}{2}\right)U(z,t), \tag{2.47}$$

L_{eff} is effective length:

$$L_{eff} = \left[1-\exp(-\alpha L)\right]/\alpha, \tag{2.48}$$

L_{NL} is nonlinear length:

$$L_{NL} = \frac{1}{\gamma P_0}. \tag{2.49}$$

It is to note that L_{NL} provides the length scales over which nonlinear effects become important for pulse evolution. If the length of the fiber sample $L << L_{NL}$, the nonlinear effects can be neglected. L_{eff} is a length scale at which the fiber with zero-attenuation has the same nonlinear impact as a fiber with attenuation α at L.

The time-dependent phase, as shown in Eq (2.46), leads to the time-dependent instantaneous frequency [80]:

$$\omega(z,t) = -\frac{\partial \Phi_{NL}}{\partial t} = \omega_0 - \gamma P_0 \frac{\partial U(t)}{\partial t} z, \tag{2.50}$$

where ω_0 is a central frequency of input pulse.

Consequently, SPM creates the new spectral components that separate from ω_0. The spectral broadening dependents on the nonlinearity of propagation medium, peak power P_0, the slope of the pulse, and propagation length z.

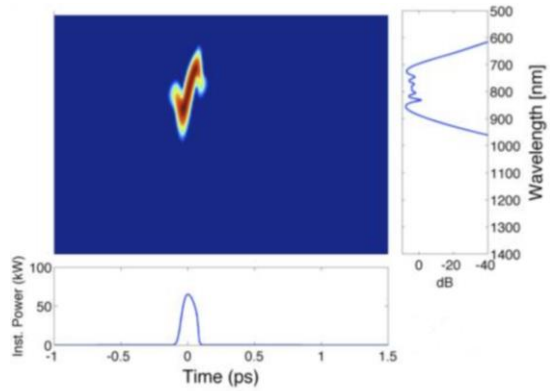

Figure 2.10. Spectrogram of the pulse due to the effects of SPM [85].

Figure 2.10 shows the temporal profile and spectrum induced by SPM. The remarkable feature of the spectral profile is the presence of many peaks, and the outmost peaks are the most intense. Due to the effects of SPM, the instantaneous frequency varies linearly in time, thus the temporal profile has the S-shape.

In the case of including the effects of *D*, two fundamentally different behaviors can be observed due to the trade-off between SPM and the effects of *D*. With normal-dispersion regime, SPM and effects of *D* lead to simultaneously temporal and spectral broadening. Consequently, the output beam with broad spectral bandwidth can be observed, as shown in the following chapters. In the anomalous *D* regime, the effects of SMP can be balanced with that of *D*, leading to the formation of soliton, as shown in Figure 2.11.

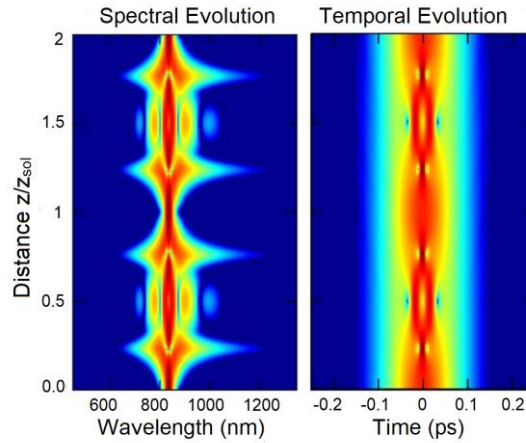

Figure 2.11. Periodic evolution of the spectral and temporal characteristics of a *N*=3 soliton with propagation distance z over one soliton period z_{sol} [86].

2.4.2 Optical Wave Breaking / Four-Wave Mixing

At the beginning of propagation length, the pulse is broadened by SPM. In the normal *D* regime, the components at the trailing edge propagate slower than the central components of the pulse, as shown in Figure 2.13 (a). When the central component overtakes the slower component, optical wave breaking (OWB) begins to appear. The overlap between these components also leads to the interference beats in the temporal pulse profile (Figure 2.13 (b)&(c)) and the new wavelength band is created by the four-wave mixing (FWM) process [85]. As shown in Figure 2.12, the new wavelength band around 700 nm is suddenly created at 3 cm of propagation and attributed to OWB. At the leading edge, OWB also occurs at 8 cm of propagation and created the wavelength band around 1300 nm. During further propagation, the energy would be redistributed from the central pulse to the leading and trailing edge, and the temporal profile would become further flat (Figure 2.13 (d)).

Figure 2.12. Evolution of the SCG along the PCF with all-normal dispersion, and input pulse with central wavelength at 790 nm, pulse duration of 200 fs, pulse energy of 20 nJ [87].

Figure 2.13. The spectrogram representation of the pulse evolution at different propagation lengths inside the all-normal dispersion PCF. The input pulse with a central wavelength at 790 nm, pulse duration of 200 fs, pulse energy of 20 nJ [87].

2.4.3 Soliton Fission

As shown in section 2.4.1, in the anomalous *D* regime, the balance of effects of SPM and *D* leads to the soliton formation. However, this balance can be unstable due to the effects of, e.g., high-order *D* and Raman scattering. These effects as the perturbation are the reason for breaking up of the injected higher-order soliton into a train of fundamental solitons (Figure 2.14). The first injected soliton has the highest intensity.

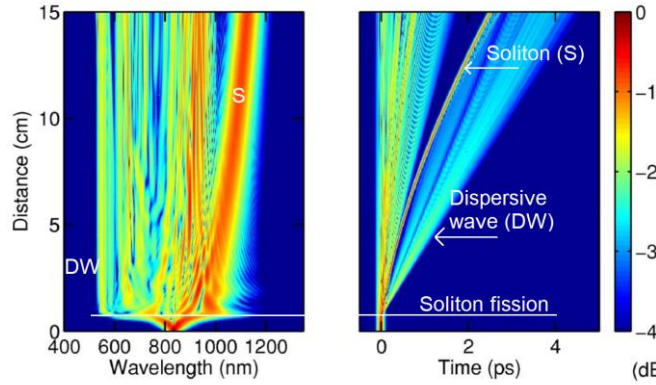

Figure 2.14. Spectral and temporal evolution in optical fiber with input pulses: central wavelength at 835 nm, pulse duration of 50 fs, and peak power of 10 kW [86].

The length of propagation (L_{fiss}) where soliton fission occurs is given in the following form [30,86]:

$$L_{fiss} = \frac{L_D}{M} = T_0 \sqrt{\frac{1}{|\beta_2|\gamma P_0}}, \tag{2.51}$$

where M is the soliton number:

$$M = \frac{L_D}{L_{NL}} = \frac{\gamma P_0 T_0^2}{|\beta_2|}. \tag{2.52}$$

After soliton fission, each fundamental soliton shifts toward longer wavelengths caused by intra-pulse Raman scattering [86]. In the quantum optics side, the scattering of the photon by a medium molecule results in lower frequency photon and higher vibrational state of the molecule [88].

2.5 Supercontinuum Generation in Optical Fiber

SCG in an optical fiber occurs when input pulse with high peak power launches the fiber [30,86]. The nonlinear effects described in the previous sections and effects of the D can cause a significant extension of the spectrum of the input pulse propagating in the optical fiber. Due to the small d_{core} of fiber (few micrometers), the optical fiber can offer the small effective mode area, and thus, nonlinear phenomena are enhanced. Nonlinear optical fibers made of silica glass or soft-glasses with near-zero flat dispersion are usually used for SCG. In the case of femtosecond laser as a pump source, there are two fundamental mechanisms for SCG, which are (i) SPM and soliton dynamics in anomalous dispersion regime and (ii) SPM and OWB induced by FWM in all-normal dispersion regime [30,86].

In the anomalous regime ($D > 0$), the effects of D and nonlinearity can be balanced with each other leading to the formation of soliton. However, due to the effects of the perturbations, e.g., high-order D, soliton fission would occur and create M injected fundamental solitons. M is the soliton number, which depends on the amount of D at the pump wavelength λ_p, peak power P_0, and pulse width T_0 of input pulses, as given in Eq (2.52). Due to the soliton mechanism, it is possible to obtain the broad spanning SC with relatively low peak power and short propagation length. However, any small intensity fluctuations of the fundamental solitons cause the wavelength fluctuations through the Raman soliton self-frequency shift (SSFS). The wavelength fluctuations of SC spectrum will be transferred into time domain due to the effects of chromatic dispersion of the fiber. As a result, anomalous dispersion SCG has a complex temporal profile, considerable intensity variations, and low temporal coherence [80]. For example, Figure 2.15 shows the evolution of anomalous dispersion SCG in optical fiber pumped by femtosecond laser pulses and the evolution of coherent characteristics along the fiber sample. At the beginning of propagation, SC spectrum has high coherence. During further propagation, the coherence is degraded due to the effects of input noises, e.g., one-photon-per-mode noise.

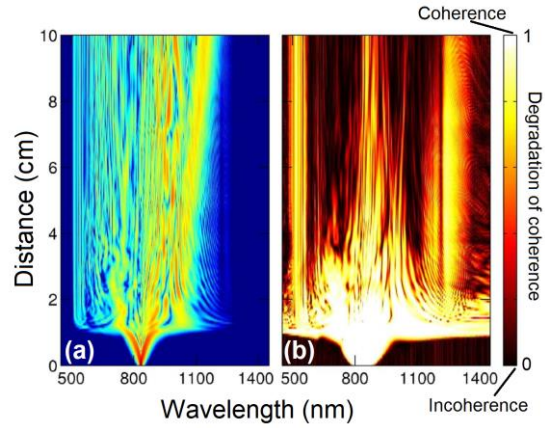

Figure 2.15. Evolution of anomalous-dispersion SCG in optical fiber (a) and of the corresponding degree of coherence (b) with input pulses: 10 kW peak power, pulse duration of 100 fs, and central wavelength at 835 nm [86].

In the case of the normal regime ($D < 0$), the spectral broadening is induced by SPM at the beginning of propagation length, and then, OWB induced by FWM is the main contribution to generate the spectral side wings. However, during further propagation, the creating new wavelength band at the trailing edge of the pulse is restricted due to the high slope of the dispersion profile. At the leading edge, the A_{eff} gradually increases with the long-wavelength band, and thus, decrease nonlinear

coefficient. Consequently, the generation of long-wavelength band at the leading edge is also limited, as shown in Figure 2.16 (a).

In the short propagation length, the effects of input noises can be effectively suppressed. Thus, the all-normal SCG at the short-propagation can offer high coherence (Figure 2.16 (b)). However, upon further propagation, the appearance of stimulated Raman scattering (SRS) and FWM components cause noisy interference structures and pulse-to-pulse fluctuations [58]. Consequently, the coherence of SCG is gradually decreased (Figure 2.16 (b)).

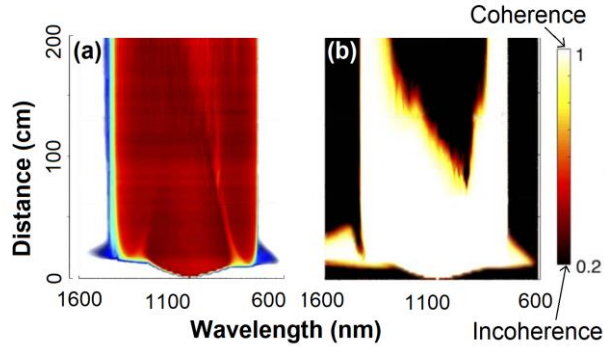

Figure 2.16. Evolution of pulse propagation in all-normal dispersion fiber (a) and the coherent characteristics with single-photon-per-mode noise over 2 m of propagation distance (b). The input pulse: peak power of 100 kW, pulse duration of 600 fs, the central wavelength at 1040 nm [58].

2.6 Fiber Material

Silica glass with high purity and high transparency in NIR range is commonly used for telecommunication fibers. However, in SCG application, the spectral bandwidth of SCG beyond 2 μm is limited by the high attenuation of silica. Thus it is necessary to consider using nonlinear glasses. The soft-glasses have been considered for MIR SCG, as shown in Table 2.1.

The fundamental material properties of these non-silica glasses can enhance SCG across the MIR range since they can have intrinsic nonlinearities from 10 times to 100 times higher that of silica, and they are transparent up to MIR range, as shown in Figure 2.17. However, their ZDWs generally locate at MIR range (Figure 2.17), thus it is challenging to design a fiber with near-zero flat normal dispersion to be compatible with commercial femtosecond lasers. Typically, the SCG in these non-silica fibers has been obtained using the pump lasers operating at long wavelength, e.g., the laser using optical parametric amplifiers (OPAs) and oscillators (OPOs) [41,89]. However, these pump lasers are complex setups and costly to maintain.

As an alternative, the use of a hollow core fiber infiltrated with liquid into the core as a propagation medium has been applied for SCG and optofluidics. In

particular, organic solvents, which have high nonlinearity and transparency, are typically infiltrated into the core of the fiber for SCG [47-54]. The low-index liquids are filled into AR fiber for application in sensors [71,72], lasers [73]. The unique optical properties of liquids are presented in Chapter 3.

Table 2.1. Optical properties of different glasses [30].

Glass type	**Code**	**Main component**	**Linear refractive index n_0**	**Nonlinear refractive index n_2 (10^{-20} m^2/W)**	**λ_{ZDW} (μm)**
Silica	Si	SiO_2	1.45	2.74	1.26
Lead Silicate	SF57	$PbO\text{-}SiO_2$	1.81	41	2
Bismuth oxide	Bi	Bi_2O_3	2.02	32	2.29
Germinate	PbGe	$PbO\text{-}GeO_2$	1.8	22	1.78
Tellurite	ZnTe	$ZnO\text{-}TeO_2$	2.03	51	2.24
Fluoride	ZBLAN	$ZrF_4\text{-}BaF_2$	1.5	3.3	1.62
Chalcogenide	AsS	As_2S_3	2.44	594	4.81
	GLS	$Ga_2S_3\text{-}La_2S_3$	2.41	216	
	GLSO	$Ga_2S_3\text{-}La_2O_3$	2.25	177	4.64

* Linear and nonlinear indices n_0 and n_2 at 1.06 μm (Si, SF57, PbGe, ZnTe, ZBLAN) and 1.5 μm (Bi, AsS, GLS, GLSO).

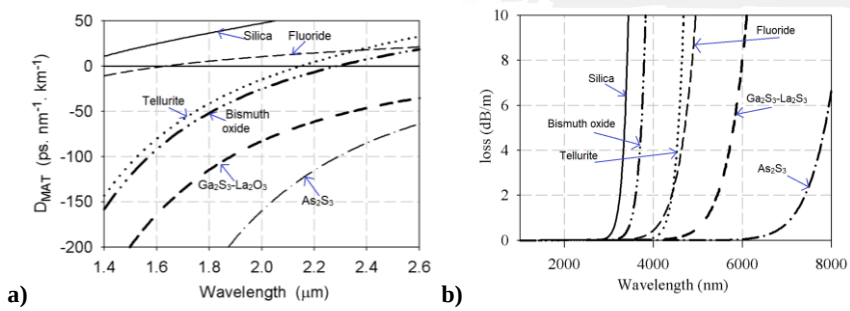

Figure 2.17. The D_m curves (a) and attenuation of soft-glasses (b). The soft-glasses are bismuth oxide glass (Bi), tellurite glass (NaTeZn), fluoride glass (ZBLAN), and chalcogenide glasses (GLSO, AsS) [30].

3 Optical Properties of Liquids

This chapter consists of two parts. The first one generalizes the optical properties of nonlinear organic solvents based on the results in the literature [46,62]. These liquids are dedicated to nonlinear liquid core PCF for SCG applications.

The second one is devoted to the first experimental investigations of transmission, refractive index, and light scattering of the buffers and cell culture media, as well as their aging effect. These aqueous solutions are foreseen for optofluidic and sensing applications. Work presented in this section is the original contributions of PhD candidate and has been published in [A5].

3.1 Organic Solvents

3.1.1 Linear Refractive Index of Organic Solvents

The linear refractive indices of organic solvents are also an important factor that influences critically the *D* of the optofluidic system, and thus, they influence the broadening of the pulses propagated in this system. As shown in Figure 3.1, most of the nonlinear liquids have higher refractive index than that of silica in NIR range. This allows the nonlinear liquid core PCF can guide the light in the core by TIR mechanism. Chloroform has lower refractive index than that of silica. However, a chloroform-core PCF can guide the light by TIR mechanism if a PCF with a large *f* is used [A6, 91]. Based on the refractive index, the D_m of liquids can be determined according to Eq (2.10) and Eq (2.11). In the NIR range, the D_m is flat, near-zero, and all-normal, Figure 3.1 (b). Therefore, it is possible to design liquid core PCFs with flat and near-zero dispersion for SCG in NIR range [59-61]. It is to note that *D* of the fiber is one of the key factors that influence the light propagation process in the medium, as presented in Chapter 2.

The linear refractive indices of liquids, and thus their D_m, are also possible to be controlled by changing ambient temperature, or even pressure of liquids, due to their extraordinary high thermo-optic and piezo-optic coefficients [50,92]. The dependence of the linear refractive index on the temperature and pressure is given in Eq (3.1):

$$n(T) = n_0 + \sigma\left(T - T_0\right) + \xi\left(P - P_0\right), \tag{3.1}$$

where n_0 is the linear refractive index of the liquid at 20 ^{0}C (T_0) and 10^5 Pa (P_0). $\sigma = \partial n / \partial T\big|_{T_0}$ and $\xi = \partial n / \partial P\big|_{T_0,P_0}$ are named thermo-optic and piezo-optic coefficient.

The thermo-optic coefficients of organic solvents are higher than the one of the glasses [93]. For example, the absolute value of thermo-optic coefficient σ of carbon tetrachloride is 5.4×10^{-4} (K^{-1}) [90] while that of silica is 0.11×10^{-4} (K^{-1}) [93]. With the high sensitivity of the refractive indices due to changing ambient temperature, liquid

core PCFs would have a high degree of freedom for *D* tuning. Chemnitz *et al.* demonstrated the soliton dynamics in carbon disulfide core fiber with *D* tunning by changing the ambient temperature in a range of 0 ÷ 40 ^{0}C [48]. H. L. Van *et al.* optimized the *D* of PCF infiltrated with water and ethanol by changing temperature [94].

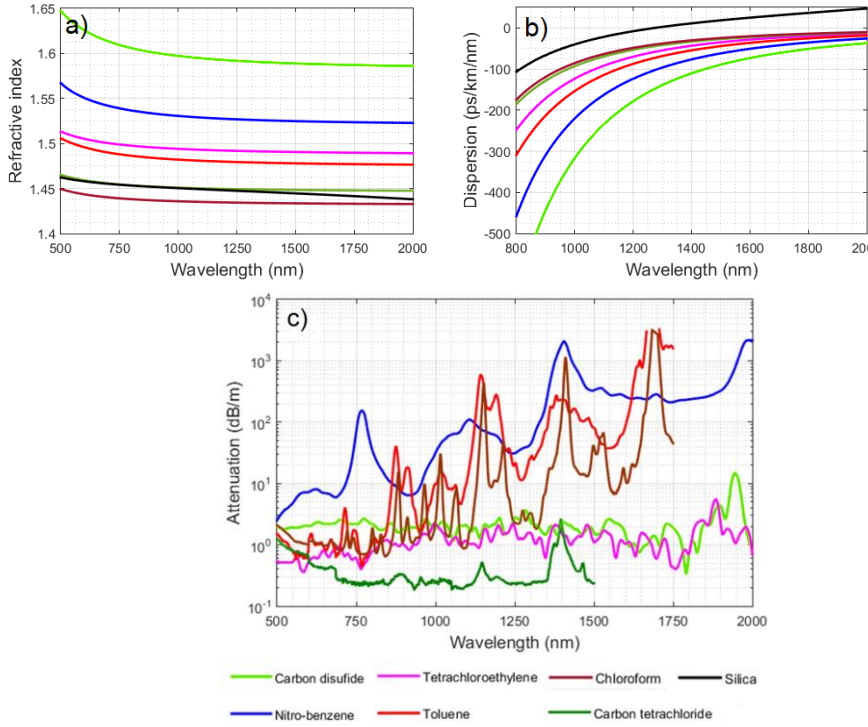

Figure 3.1. Linear optical properties of organic solvents. Linear refractive indices (a), *D* (b), and attenuation (c) [46,49,59].

The attenuations of the nonlinear liquids are shown in Figure 3.1(c). Chloroform and benzene derivatives have high attenuation in NIR. The absorption of liquids results in the decrease of light energy in the core of the fiber, and thus, the intensity of the output beam is decreased. On the other hand, the attenuations of carbon disulfide (CS_2), carbon tetrachloride (CCl_4), and tetrachloroethylene (C_2Cl_4) in NIR range are relatively low when compared with those of other organic solvents. CCl_4 is an interesting liquid for optofluidic application because it is highly transparent up to 11 μm [46,95]. Refractive index of CCl_4 is similar to that of silica, this allows to obtain high coupling efficiency between CCl_4-core PCF and single mode fiber for all-fiber SCG systems.

3.1.2 Nonlinear Properties of Organic Solvents

Nonlinear refractive indices of organic solvents are comparable to those of soft-glasses. The nonlinear refraction of the liquids originates from the bound-electron and nuclear mechanism [62,90]. The bound-electron mechanism contributes to the third-order response via the effects of purely electronic second hyperpolarizability of the individual molecules. The response time of this mechanism is typical below 1 fs, while that of nuclear mechanisms are approximately hundreds of fs owing to the large mass of the nuclei [62,90]. Because commercial femtosecond lasers typically have pulse duration around a few hundred femtoseconds, the bound-electron mechanism seems to be essentially instantaneous. Therefore, it has been called as an instantaneous contribution while nuclear mechanisms are named non-instantaneous contributions. The effective nonlinear refractive index ($n_{2,eff}$) originate from these contributions are written as given in Eq (3.2) [62,90]:

$$n_{2,eff} = n_{2,el} + \frac{\int_{-\infty}^{\infty} I(t) \int_{-\infty}^{\infty} R(t-t') I(t') dt' dt,}{\int_{-\infty}^{\infty} I^2(t) dt} \tag{3.2}$$

where $I(t)$ is the irradiance, $R(t)$ is a non-instantaneous component of the third-order response, $n_{2,el}$ is nonlinear refractive index originating from bound-electrons that depend on the linear refractive index n_0, the vacuum permittivity ε_0, and the bound-electronic third-order susceptibility $\chi^{(3)}$ as given in Eq (3.3) [80]:

$$n_{2,el} = \frac{3\,Re\left(\chi^{(3)}\right)}{4 n_0^2 \varepsilon_0 c}. \tag{3.3}$$

The nuclear mechanisms originate from nuclear motion due to the effects of external light and are described in Eq (3.2) by the term of $R(t)$. The nuclear contribution is as a sum of three responses, i.e., molecular reorientation, libration, collision-induced [62], as given in Eq (3.4):

$$R(t) = \frac{1}{N}\left[n_{2l} C_{2l} e^{-t/t_{fl}} \int_0^{\infty} \frac{\sin(\omega t)}{\omega} g(\omega) d\omega + \sum_{k=c,d} n_{2k} C_{2k} \left(1 - e^{-t/t_{rk}}\right) e^{-t/t_{fk}} \right] \Theta(t), \tag{3.4}$$

where d, c, l denote reorientation, collision-induced, libration contribution, respectively. $\tau_{r,k}$ and $\tau_{f,k}$ are rise time and fall time. $N = n_{2,el} + n_{2,l} + n_{2,c} + n_{2,d}$.

Due to the contribution of non-instantaneous mechanism, nonlinear responses of organic solvents are comparable to those of soft-glasses, e.g. telluride, chalcogenide. The effects of the four mentioned mechanisms have different polarization dependencies. In particular, the bound-electronic and collision-induced follow isotropic symmetry while reorientation and libration follow anisotropy. Therefore, nonlinear liquids with asymmetrical molecules, e.g., CS_2, would have a high ratio of non-instantaneous contribution to nonlinear response due to the effects of the external field, while CCl_4 with symmetrical molecule does not have the

contribution of reorientation and libration mechanism to nonlinear response [62], as shown in Table 3.1.

A pulse-width dependence of the n_{eff} of the liquids is shown in Figure 3.2. In the case of pulse-width < 50 fs, the instantaneous mechanism is a significant contribution to the nonlinear refractive index ($n_{2,el} \approx n_{2,eff}$). When pulse-width increases from 50 fs to 3 ps, the liquids with asymmetrical molecules, e.g., CS_2, toluene, have an exponential increase of $n_{2,eff}$ due to noninstantaneous nuclear contributions, particularly librational and reorientation responses. CCl_4 with the symmetrical molecule does not show a considerable increase of $n_{2,eff}$ for long pulse-width.

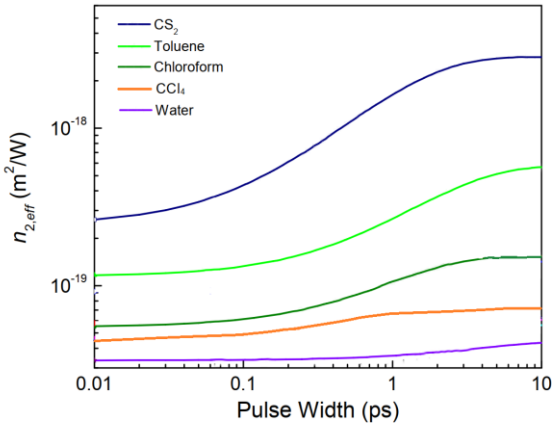

Figure 3.2. The pulse-width dependent $n_{2,eff}$ of nonlinear liquids [62,96].

CS_2 has high nonlinearity and high transparency in NIR range and has been used for several optofluidics applications [53,97]. However, it is highly toxic, carcinogenic, and explosive [98,99]. On the other hand, CCl_4 and toluene are much lower toxicity when compared to that of CS_2. Moreover, CCl_4 with high transparency [46,95] has been popularly used in the optofluidic applications [49,100]. Toluene, with a high nonlinear refractive index, can offer the SC spectrum with a broad spectral bandwidth in a short fiber sample [60]. The use of short fiber samples can avoid the effects of high attenuation of toluene in NIR range. Therefore, in this dissertation, CCl_4 and toluene-core PCFs would be used for SCG.

Table 3.1. Parameters of optical properties of organic solvents.

		Linear property		**Nonlinear parameter**			
Liquid	Chem. formula	Ref. index @ λ=1.04μm	Ther.-optic coeff.	$n_{2,el}$	$n_{2,d}$ $\tau_{r,d}$ $\tau_{f,d}$	$n_{2,c}$ $\tau_{r,c}$ $\tau_{f,c}$	$n_{2,l}$ $\tau_{f,l}$
Carbon disulfide	CS_2	1.5961 [46]	-7.80 [93]	1.50 [62]	18 0.15 1.61	1.0 0.15 0.14	7.6 0.45
Toluene	$C_6H_5CH_3$	1.4816 [46]	-5.51 [93]	0.60 [62]	3.0 0.25 2.1	0.12 0.25 0.2	1.2 0.35
Nitro-Benzene	$C_6H_5NO_2$	1.5298 [46]	-4.60 [93]	0.6 [62]	5.0 0.1 3.5	0.35 0.2 0.1	1.7 0.4
Tetrachloroethylene	C_2Cl_4	1.493 [49]	-5.5 [92]	0.53 [49]	5.01 0.1 4.5	0.31 0.1 2.98	2.08 0.78
Carbon tetrachloride	CCl_4	1.4506 [46]	-5.40 [93]	0.48 [62]	-	0.2 0.1 0.15	-
Chloroform	$CHCl_3$	1.4355 [46]	-5.30 [93]	0.41 [62]	0.75 0.25 1.8	0.08 0.1 0.1	0.4 0.25

- *$n_{2,m}$ are given in the units of 10^{-19} m^2/W; $\tau_{r,m}$ and $\tau_{f,m}$ are given in units of ps. The thermo-optic coefficient in 10^{-4} K^{-1}.*

3.2 Buffers and Cell Culture Media

In recent years, the knowledge of the interaction of light with the various cultured microorganisms, e.g., cells, bacteria, are applied widely in, e.g, bio-sensor [101] and optofluidic bio-lasers [102-104]. In order to keep the living microorganisms, buffer and cell culture media (CCM) are typically required to deliver biochemical nutrients for them. However, for measurements and numerical analyses, the optical properties of buffers and CCM are considered to be equivalent to those of water, which may have a negative impact on the performance of these devices and the interpretation of data obtained during measurements. Otherwise, obviously, the clear information of the optical properties of the aqueous solution allows to optimize the design of the optofluidic devices.

This section shows the first experimental results of the linear properties of commercial buffers and cell culture media. The results shown in this section are based on the paper [A5].

3.2.1 Definition of Buffers and Cell Culture Media

The aqueous solutions, which contain and provide the life function for cultured microorganisms, are called buffer (buffer solution) or CCM. Buffer is an aqueous solution, which typically is either a mixture of weak acid and salt of this acid with a conjugate base or vice versa. The unique properties of the buffer are to keep pH at nearly constant when the acid or the base is added. Therefore, buffers have been used in the biological system for the activation of many enzymes, e.g., blood plasma [105]. CCM are typically liquids designed to support the growth of microorganisms or cells [106]. Different type of CCM is used for different types of cells [107]. Generally, CCM contains the nutrients, growth factors, hormones, and other biologically-active which are essentially required for in-vitro growth, storage, or transport of living cells.

Two popular used buffers and two CCM are demonstrated linear optical properties, i.e., refractive index, scattering, transmission. Two buffers are Dulbecco Phosphate Buffered Saline (PBS) and TRIS- Borate-EDTA Buffer (TBE). Two CCMs are Express Five™ SFM (EXPRESS 5) and Dulbecco's Modified Eagle's Medium (DMEM).

PBS contains NaCl, phosphate buffer, and KCl, and has pH in the physiological range of 7.2 ÷7.6. It has been used for cultured cells or performing analysis with RNA and protein. TBE contains TRIS (tris(hydroxymethyl)aminomethane), boric acid, and EDTA (Ethylenediaminetetraacetic acid). TBE typically is used to stabilizing nucleic acid against enzymatic degradation [108]. EXPRESS 5 and DMEM contain specific nutrients like glucose, sodium pyruvate (source of energy), specific egzogenous amino acids, $NaHCO_3$, and buffering salts. They have been used in many types of human, mammalian cell culture or procedures. The main components of these liquids are summarized in the Table. 3.2.

The ingredients of the buffers and CCM can be changed with stored time, and thus, optical properties of buffers and CCM may change over time. In the following sections of this chapter, the optical properties of fresh, 3-months, and 8-months storage buffers and CCM are measured.

Table 3.2. The main properties of investigated fresh buffers and CCM.

Buffer/CCM	Stability [months]	Storage temperature [^{0}C]	Composition	Producer, formal characteristics
TBE (TRIS-Borate-EDTA Buffer)	24	15-30	89 mM Tris, 89 mM boric acid, 2 mM EDTA; pH ~8.3 at 25°C	Buffer, Merck-Millipore cat. No. 574795
PBS (HyClone™ Dulbecco's Phosphate Buffered Saline solution)	24	15-30	140 mM NaCl, 10 mM phosphate buffer, 3 mM KCl; pH 7.4 at 25°C	Buffer, GE Healthcare cat. No. SH30028.02 Hyclone
EXPRESS 5 (Cell culture medium Express Five™ SFM)	18	2-8	sodium pyruvate $NaHCO_3$, low glucose, low phenol red; serum-free medium	Used for protein purification and in Baculovirus Expression Vector System; Gibco cat. No. 10486-025
DMEM (Cell culture medium Dulbecco's Modified Eagle's medium)	6	2-8	sodium pyruvate, $NaHCO_3$, low glucose, phenol red.	Used for cell culture; SIGMA cat. No. D5796

3.2.2 Refractive Index of Buffers and Cell Culture Media

The Michelson interferometer used to measure the group refractive index (N_g) of fresh buffers and CCM is shown in Figure 3.3. As a light source, a fiber-coupled HL-2000 halogen lamp (Ocean optics Inc., Largo, FL, USA) is used to ensure the stable and flat the input spectrum. The HL-2000 provides the spectrum with a wavelength range of 360÷2400 nm. The liquids are investigated in a cuvette, which is made from pure silica. The cuvette has square cross-section 10×10 mm and the wall thickness of 1mm. The light emitted from the source is collimated by micro-lens (L), and then it is divided into two parts by beam splitter (BS). The first part of the light (signal arm) passes through the cuvette and is reflected by mirror (M_2), which is mounted on the 2-axis stage. Another part in reference arm has optical path that is adjusted by the translation motion of mirror (M_1). The spectrometers are: visible spectrometer (Red Tide, Ocean Optics Inc., Largo, FL, USA) with range wavelength

of 350÷1000 nm and infrared spectrometer (AvaSpec-NIR256/512-1.7, Avantes BV, Apeldoorn, The Netherlands) with range wavelength of 900÷1700 nm.

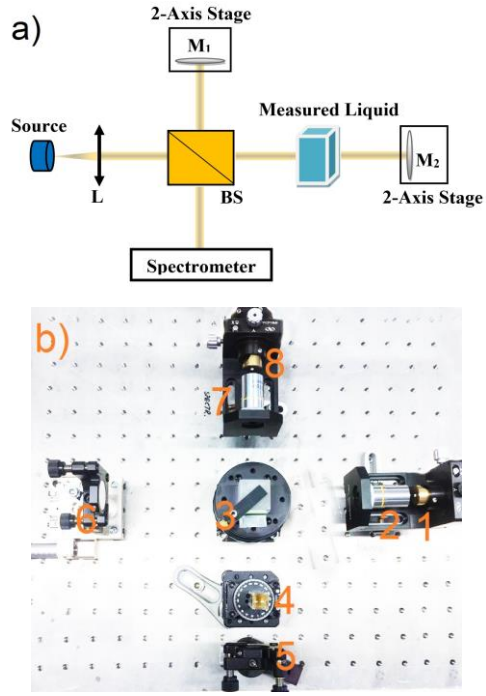

Figure 3.3. Schematic representation of Michelson interferometer (a), and experimental set up (b) with:

1. The output of the multimode fiber, which guides the light from the halogen lamp
2. Micro-objective 20X, which collimate the light
3. Beam splitter
4. Cuvette containing tested liquid
5. Mirror in the signal arm
6. Mirror in the reference arm
7. Micro-objective, which converges light to input face of multimode fiber
8. Multimode fiber, which connects the spectrometer

In each measurement, the mirror M_1 is adjusted to obtain the balanced interferometer configuration with zero displacements. Then, an empty silica cuvette is mounted. Its group refractive index is also measured. In the following step, the tested liquid is poured into the cuvette. In general, the difference of the optical path between the signal arm and reference arm is given in Eq (3.5):

$$\Delta(\lambda) = 2L_1 - 2L_2 - 2\left(N(\lambda) - 1\right)d, \tag{3.5}$$

where $2L_1$ and $2L_2$ are an optical path in the air of reference arm and signal arm, respectively. $N(\lambda)$ and d is group refractive index and length of the investigated sample, respectively.

$N(\lambda)$ is determined by the value of wavelength λ that satisfies $\Delta(\lambda)$ equal to zero and spectral interference fringes have an infinite period:

$$N(\lambda) = \frac{L_2 - L_1}{d} + 1 \Rightarrow N(\lambda) = \frac{\Delta l}{d} + 1, \tag{3.6}$$

where Δl is the deference of the optical path of the reference arm and signal arm.

The relation between the $N(\lambda)$ and phase refractive index ($n(\lambda)$) is given in Eq (3.7) [80]:

$$N(\lambda) = n(\lambda) - \lambda \frac{dn(\lambda)}{d\lambda}. \tag{3.7}$$

For each liquid, $n(\lambda)$ is formed by Sellmeier as given in Eq (3.8):

$$n^2(\lambda) = 1 + \sum_{i=1}^{3} \frac{B_i \lambda^2}{\lambda^2 - C_i}, \tag{3.8}$$

giving $N(\lambda)$ is described in Eq (3.9):

$$N(\lambda) = n(\lambda) + \frac{\lambda^2}{n(\lambda)} \sum_{i=1}^{3} \frac{B_i C_i}{\left(\lambda^2 - C_i\right)^2}, \tag{3.9}$$

where B_i and C_i are Sellmeier constants. The fitting of experimental data of $N(\lambda)$ with Eq (3.9) allows for the identification of the Sellmeier constants.

$n(\lambda)$ of distilled water is measured and compared with other results as shown in [109]. The difference between the value of the experimental data and reference data [109] for $n(\lambda)$ is 10^{-4} (Figure 3.4). This difference result originates from the sensitivity of the spectrometers. The agreement between experimental data for $n(\lambda)$ of water and those in [109] confirms that the Michelson setup as shown in Figure 3.3, can be used to measure $n(\lambda)$ of tested liquids.

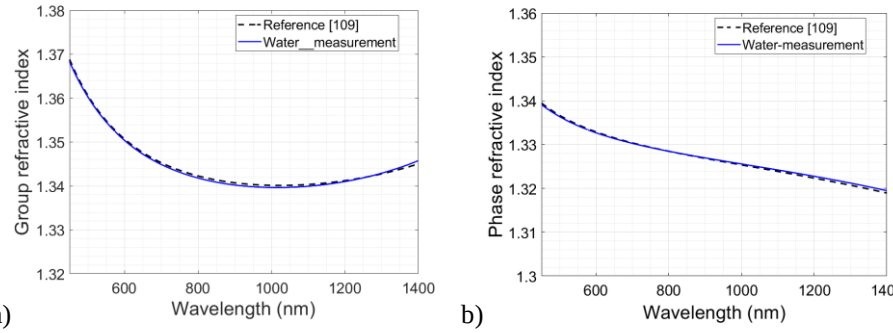

Figure 3.4. The experimental data of $N(\lambda)$ (a) and $n(\lambda)$ (b) of distilled water. The values are compared to those in [109].

n(λ) of the fresh buffers and CCM in the wavelength range of 450÷1450 nm are presented in Figure 3.5. The results show that *n(λ)* of buffers and CCM is slightly higher than that of water. The reason for higher *n(λ)* relates to the addition of chemical and biological nutrients in buffers and CCM. In particular, *n(λ)* of buffers, on average, is higher than that of water by 0.08 %. The structural components of CCM are different from those of buffers, this leads to the differences of refractive indices. CCM have phase refractive indices, on average, higher by 0.2% than that of water. These differences may play a significant role when the use of these media for label-free sensing devices is considered. These experimental data are fitted with Sellmeier performance, as written in Eq (3.8) with coefficients shown in Table 3.3.

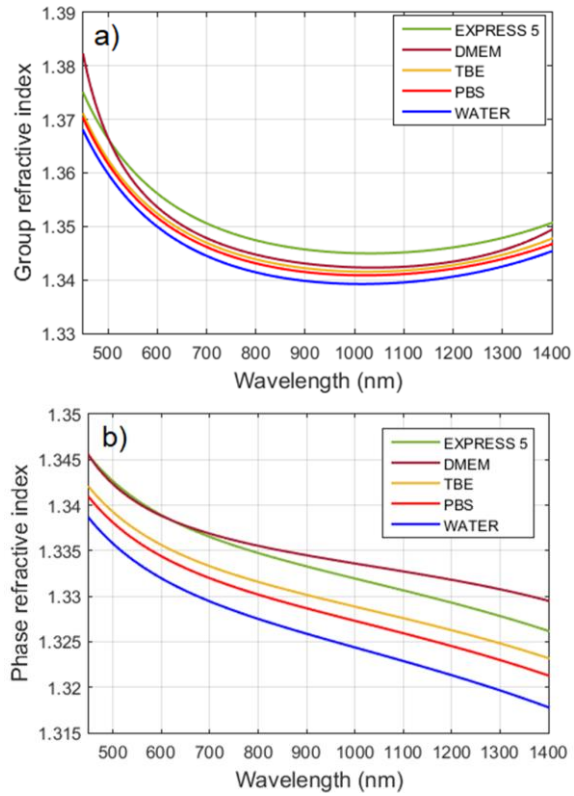

Figure 3.5. Group (a) and phase refractive indices (b) measured for the investigated liquids. Legend: TBE—TRIS-Borate-EDTA Buffer; PBS—Dulbecco's Phosphate Buffered Saline solution; EXPRESS 5—Cell culture medium Express Five™ SFM; DMEM—Cell culture medium Dulbecco's Modified Eagle's Medium.

Table 3.3. Sellmeier coefficients of the buffers and CCM.

Coefficients	DMEM	EXPRESS 5	TBE	BPS
B_1	0.770818	0.775107	0.766475	0.763614
B_2	-12,415.01	-8912.71	-9070.89	-9246.06
B_3	73.6953	41.0681	40.3204	47.7781
C_1 (μm^2)	0.00945	0.00907	0.00898	0.00905
C_2 (μm^2)	22578.45	31067.85	30520.46	30036.29
C_3 (μm^2)	135.0971	140.2136	133.3024	151.858

Legend: TBE—TRIS-Borate-EDTA Buffer; PBS—Dulbecco's Phosphate Buffered Saline solution; EXPRESS 5—Cell culture medium Express Five™ SFM; DMEM—Cell culture medium Dulbecco's Modified Eagle's Medium.

n(λ) at wavelength λ=589 nm, named n_D, of the buffers and CCM stored in the fridge for 3 months and 8 months are measured by Abbe refractometer (RL-3, PZO S.A Warsaw, Poland) and shown in Table 3.4. These results indicate that n_D of buffers and CCM has not been significantly changed with long-term handling. There is only n_D of 8 months PBS that slightly increased. This increase may originate from the results of the salt crystallization of NaCl and KCl, which are a component of PBS.

Table 3.4. Evolution of n_D of investigated liquids with a storage time of the buffers and CCM.

Liquid	Fresh	3 months	8 months
DMEM	1.3370	1.3373	1.3375
EXPRESS 5	1.3381	1.3381	1.3381
TBE	1.3360	1.3362	1.3362
PBS	1.3348	1.3349	1.3362

Legend: TBE—TRIS-Borate-EDTA Buffer; PBS—Dulbecco's Phosphate Buffered Saline solution; EXPRESS 5—Cell culture medium Express Five™ SFM; DMEM—Cell culture medium Dulbecco's Modified Eagle's Medium.

3.2.3 Transmittance of Buffers and Cell Culture Media

The setup to measure transmission properties of buffers and CCM is shown in Figure 3.6. The light source is a fiber-coupled HL-2000 halogen lamp. The liquids are investigated in a silica cuvette (10×10-mm and the wall thickness of 1 mm). The light is collimated by an achromatic minor-objective (L), and it propagates perpendicularly to the wall of the cuvette. The output beam from the cuvette is divided into two parts by a flip mirror (M) to ensure robust coupling conditions to both the spectrometers. The spectrometers are again visible spectrometer (Red Tide, Ocean Optics Inc., Largo, FL, USA) with range wavelength of 350÷1000 nm and infrared spectrometer (AvaSpec-NIR256/512-1.7, Avantes BV, Apeldoorn, The Netherlands) with range wavelength of 900÷1700 nm. They are used simultaneously to record the intensity of output light.

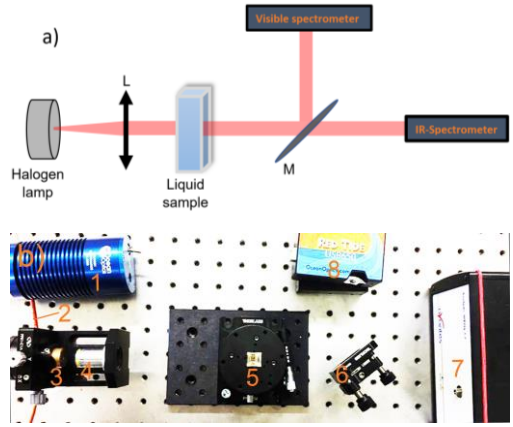

Figure 3.6. Schematic representation of transmission measurement setup (a), and experimental set up (b) with:

1. Halogen lamp
2. Multimode fiber
3. The end of multimode fiber
4. Micro-objective 20X
5. Cuvette containing tested liquid
6. Mirror
7. IR spectrometer
8. Visible spectrometer

The transmittance of 10 mm length of the liquid sample is determined in the following step, (i) measure output intensity I_0 of the light for empty cuvette, (ii) measure intensity of output beam I_1 for cuvette containing the liquid. The relation between I_0 and I_1 are calculated in the case of normal incidence and neglecting the distinction between *s* and *p* polarization [110]:

$$\frac{I_0}{I_1} = \frac{T_a^2}{T_b^2 T} \Leftrightarrow T = \frac{I_1 T_a^2}{I_0 T_b^2} \tag{3.10}$$

where T is the transmittance of the 10 mm length of the liquid sample. T_a and T_b are transmitted power at the interface silica-air or silica-liquid, respectively. T_a and T_b are determined by Fresnel's equation is given in Eq (3.11), where n_s and n_l are $n(\lambda)$ of silica and liquid, respectively.

$$T_a = 1 - \left|\frac{n_s - 1}{n_s + 1}\right| \text{ and } T_b = 1 - \left|\frac{n_s - n_l}{n_s + n_l}\right| \tag{3.11}$$

n_s and n_l have already been measured. It is assumed that the refractive index and transmittance of air in the laboratory are equal to 1.

Transmittance of the 10 mm length of liquid samples is presented in Figure 3.7. Transmission spectra of the buffers are similar to that of water. In particular, the buffers are transparency in the visible range and show relatively low transparency in the NIR range. Two absorption peaks appear at 950 nm and 1200 nm, which relate to overtones of the OH-group stretch mode. The results also show that the addition of the ingredients, i.e., TRIS, NaCl, KCl, EDTA, boric acid, to water do not change the transmission. In the case of CCM, the addition of nutrients, e.g., glucose, sodium pyruvate, and phenol red dye leads to decreasing the transmission in the visible range, while it is similar to that of water in the NIR range. In particular, EXPRESS 5 has a relatively low transmission with wavelength below 600 nm. DMEM contains a high concentration of phenol red dye, thus, the phenolsulfonphthalein absorption results in critical reduction of transmission in the visible range, i.e. the absorption peak around 570 nm.

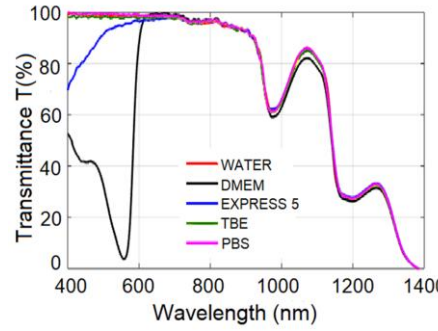

Figure 3.7. The transmission of the investigated liquids measured in the 10-mm-long cuvette. Results of water are provided for reference.

The buffers and CCM are kept in the dark in the fridge at a temperature of 4^0C. Next, the liquids with 3-months and 8-months storage time have been measured for their transmission. The aim of this work is also to verify the influence of long-term handling on properties of buffers and CCM. Figure 3.8 presents the transmittance of

the stored liquid samples. The results pointed out that the buffers and CCM kept below 3-months do not change significantly their transmission. However, those of CCM decrease critically with 8-months storage (Figure 3.8 (a),(b)). In particular, the transmission of EXPRESS 5, which is kept for 8-months, is extremely low. During the storage process, CCM might be degraded and/or infected by fungi or bacteria, resulting in increasing light scattering and decreasing the transmission. Indeed, the CCM should be used no longer 1 month from the date of the first use as recommended by the manufacturer. The CCM should be used within 2-4 weeks in a clean-room environment, such as in a chamber with laminar flow to reduce the possibility of infection. The degradation of CCM is caused by low concentration of CO_2 in room conditions (around 0.4 %), while the concentration of CO_2 for cell culture in an incubator is typical at 5% ÷10%.

For the buffers, the transmission of TBE is stable during 8-months of storage. The high stability relates to TBE containing Tris, boric acid, and EDTA, which offer the alkaline pH condition. Transmission of PBS has not been changed for the first 3-months of storage. However, it is significantly reduced in the visible range with further storage time. For 8-months stored PBS, the transmittance is reduced by around 25% at 400 nm wavelength and 10% at 600 nm. The decrease in transmission of PBS results from the crystallization of salts, e.g., NaCl, KCl.

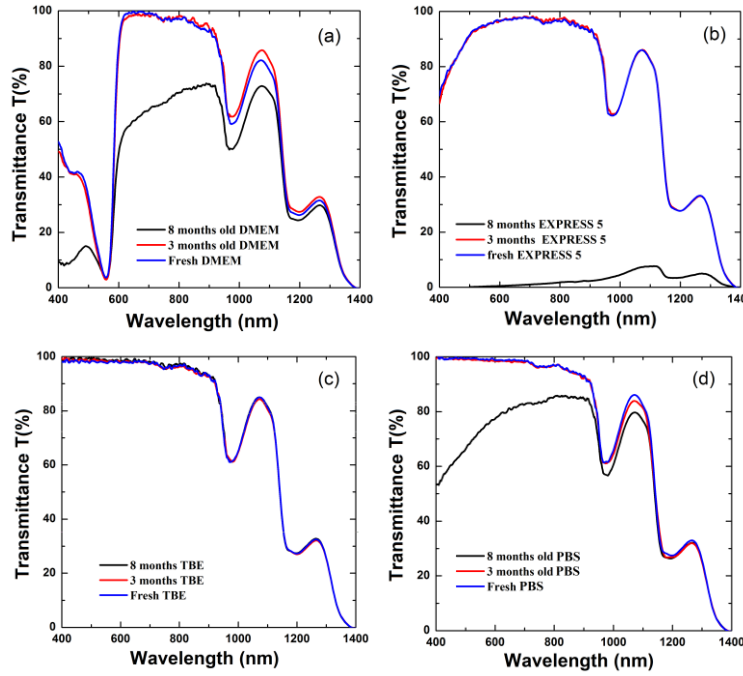

Figure 3.8. The effect of long-term handling on transmission characteristics of (a) DMEM, (b) EXPRESS 5, (c) TBE, and (d) PBS.

3.2.4 Light Scattering of Buffers and Cell Culture Media

Scattering losses of buffers and CCM are measured by setup as shown in Figure 3.9. The light source is a single mode semiconductor laser (LP660-SF60, Thorlabs Inc., Newton, NJ, USA) with a wavelength of 658 nm. The collimated light from the laser source was directed to Aperture 1, which has a diameter of 0.3 mm. The investigated liquid is covered in a cylindrical cuvette, which is made from silica and has a diameter of 130 mm, the wall thickness of 0.5 mm. The light from cuvette propagates to Aperture 2 with a diameter of 1.3 mm and then is directed to the lens. The light intensity (optical power) at each scattering angle is measured. The Aperture 2, lens, and optical power are mounted on the rotation stage, which rotates from -90^0 to 90^0 around the cuvette.

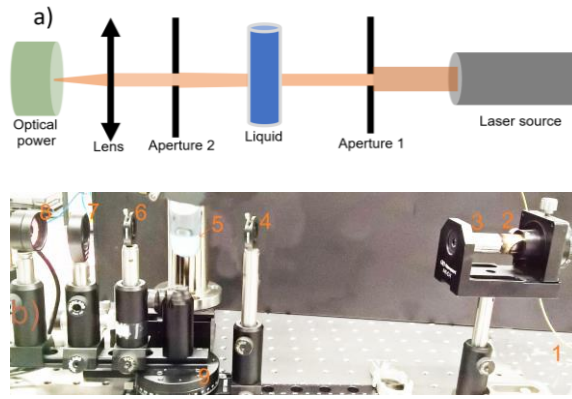

Figure 3.9. Scheme of scattering measurement (a), and experimental setup (b) with:
1. Single mode fiber, which guides the light from the laser
2. The output end of the single mode fiber
3. Micro-lens 10x collimating the light
4. Aperture with a diameter of 0.3 mm
5. Cuvette containing the tested liquid
6. Aperture with a diameter of 1.3 mm
7. Focusing lens
8. Optical powermeter
9. Vertical translation platform

For this scattering measurement, the ratio P_α / P_0 is measured at each angle α and intensity at α=0, where α is named scattering angle. The scattering characteristics of the fresh buffers and CCM are presented in Figure 3.10. The results point out that the light intensity decreases exponentially with the scattering angle. At the scattering angle of 5^0, the light intensity is 10^3 times smaller than P_0. In the case of α larger than 45^0, the light intensity reduces approx. zero for all of the liquids. A light scattering of fresh buffers and CCM is similar to that of distilled water. Therefore, it is possible to

conclude that the addition of ingredients, e.g. salts, phenol red, nutrients, acid, does not influence the light scattering.

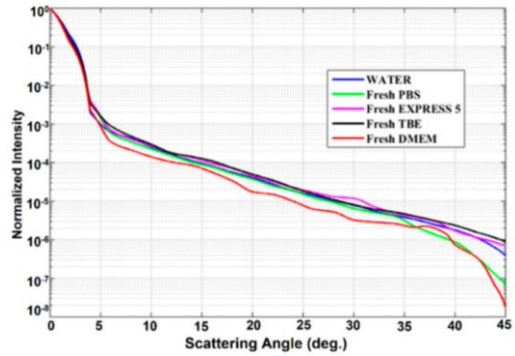

Figure 3.10. Scattering properties of the investigated liquids.

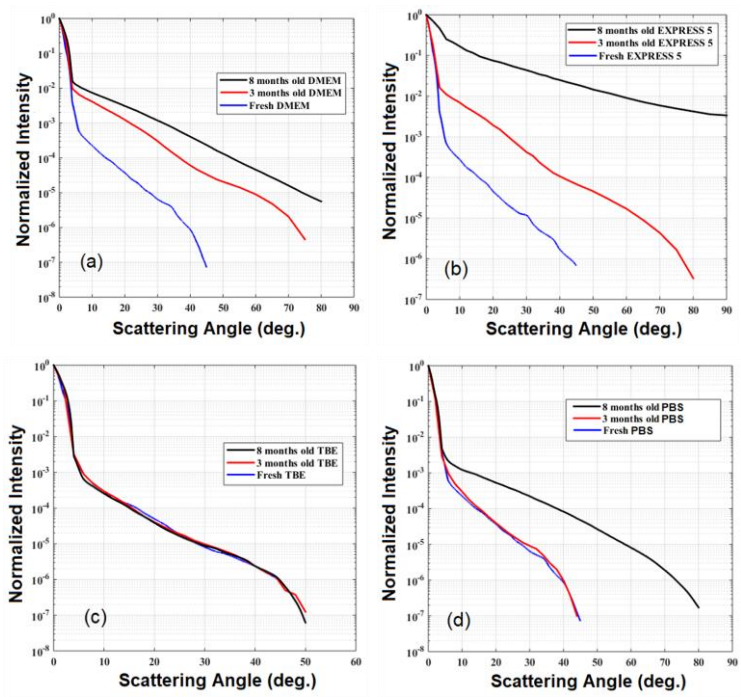

Figure 3.11. Light scattering characteristics after 3- and 8-months-long storage time for (a) DMEM, (b) EXPRESS 5, (c) TBE, and (d) PBS.

The light scattering of TBE buffer does not change over the stored time. As shown in Figure 3.11(c), the light scattering of TBE stored for 3-months and 8-months is similar to that of fresh TBE. The light scattering of PBS buffer does not

change during 3 months of storage. However, scattering of 8-months stored PBS is significantly increased, due to crystallization of the salts in PBS. The crystallization can create the particles, and their size is comparable with the wavelength of the laser source. The light scattering of CCM has changed remarkably in time stored. In particular, 8-months stored EXPRESS 5 has dramatically changed the light scattering, such as, at a scattering angle of 45^0, the normalized intensity increase from 10^{-6} (fresh EXPRESS 5) to 10^{-2} (8-months stored EXPRESS 5). At the scattering angle of 90^0, the normalized intensity is around 10^{-3}. The change of light scattering leads to decrease of transmission of these liquids, as shown in Figure 3.11(b). The increase of light scattering originates from the addition of, e.g., infection by bacteria. Moreover, the nutrient ingredient decomposition also results in degradation of the medium.

3.3 Conclusion

In the case of organic solvents, their optical properties are summarized from the literature [46,62]. Organic solvents have relatively high nonlinear refractive indices, which can compare with that of soft-glass for SCG fiber. The major part of the nonlinear response of organic solvents is the result of the non-instantaneous contributions, which originates from nuclear mechanisms. The $n_{2,eff}$ of the liquids depends on the pulse-width. With short input pulses, only the bound-electronic nonlinearity contributes significantly due to the nearly instantaneous nature, thus $n_{2,eff} \approx n_{2,el}$. With long input pulses, the effect of the reorientation mechanism is a significant contribution to the nonlinear response asymmetrical molecules, such as CS_2, toluene.

Most of the nonlinear liquids have higher refractive indices than that of silica. Thus, hollow core silica PCFs infiltrated with these liquids guide the light by TIR mechanism. CCl_4, C_2Cl_4, and CS_2 are highly transparent in the NIR range [46,49]. Therefore, they are the most interesting liquids for nonlinear photonics. The use of organic solvents filled into the core of the hollow core fiber, which allows enhancing the optical nonlinearity of the liquids and tunable *D*, has emerged as a promising approach for both of fundamental nonlinear optics and the development of new kind of custom-tailored light sources. In the following chapters for SCG, CCl_4 and toluene would be used, since they are high nonlinear, high transparent in NIR, and lower toxicity when compared to that of other nonlinear liquids [99]. For instance, the threshold limit value (TLV), which is a level that a person can be exposed to day after day for a working lifetime without adverse effects, can be used to estimate the toxic level of organic solvents. TLV of toluene is 75 mg/m^3, while that of carbon disulfide and benzene are 31 and 1.6 mg/m^3, respectively [98]. In fact, due to low toxicity, toluene has been used for some commercial products, e.g. temperature sensors [111]. In the case of CCl_4, it has refractive index very similar to that of fused silica in NIR range, thus CCl_4-core PCF can offer high coupling efficiency with typical silica fibers when all-fiber SCG system is considered.

In the case of Buffers and CCM, they have refractive indices that are slightly higher than that of water. The difference may reach up to 0.012 and 0.006 for CCM and buffers in the NIR range, respectively. Transmission of buffers is similar to that of water, while that of CCM is relatively low in NIR range. The transmission window of these liquids is limited at the 1.4 μm wavelength. This leads to the limited application of the buffers and CCM in optofluidic devices, e.g., sensors. With long-term storage, the transmission of the buffers is stable for 3 months, however, transmission of 8 months stored PBS remarkably decreases due to the crystallization of the salts. In the case of CCM, light scattering has been increasing over time, resulting in a decrease in transmission. The significant change of optical properties of buffers and CCM can lead to the misleading results of some optical experiments. The well-known change of optical properties in stored time would provide the database, which uses to investigate the degradation process of liquids in long-term handling.

The linear properties of buffers and CCM are important for the development of optofluidic systems. For example, the bio-sensors, which are used to detect a biological component, usually rely on a label-free sensing mechanism. In such a case, the changes in the optical properties of the growing biological films are monitored in the vicinity of the sensor surface [112,113]. In recent years, due to the “selectivity”, the sensor is possible to detect the target species at extraordinarily low concentration [113]. Therefore, the changes in optical properties of aqueous media containing cultured microorganisms influence crucially the results.

4 Linear Optical Properties of Photonic Crystal Fibers Infiltrated with Liquids

This chapter has been devoted to the design and fabrication of toluene-core and CCl_4-core PCFs for SCG applications. The finite difference eigenmode method is used to design liquid core PCFs. Next, the liquid core PCFs with selected structures are fabricated, and their linear optical properties are experimentally verified. The results shown in this chapter are based on the papers [A1-A3].

The nonlinear refractive index of organic solvents is relatively high [45]. Some organic solvent, e.g., CCl_4 is highly transparent in NIR [46]. Therefore, the optical fibers infiltrated with organic solvents are promising for SCG. There are the SCG experiments in liquid core fibers reported in [48÷57], but most of them used step-index fibers, which are micro-capillary infiltrated with selected liquid into the core as a light propagation medium. However, the lack of flexibility in the design of step-index fiber led to the limitation in *D* engineering. First observations of SCG in water-core PCF were reported in [55-56]. It is worth noting that water has a low nonlinear refractive index, thus it cannot be treated as a good combination with unique properties of PCF for SCG applications.

Using the hollow core silica infiltrated with high nonlinear liquid it is possible to optimize the *D* profile, the A_{eff}, and mode properties, by independent changing the size of air-holes and Λ.

4.1 Optical Properties of Toluene and Carbon Tetrachloride

Toluene and CCl_4 have been selected for investigation in this work. Toluene has a high nonlinear refractive index ($n_{2,\ \mathrm{toluene}} = 16\times10^{-19}$ m^2 /W at λ=1064 nm [45]). It also has relatively high attenuation in NIR range [46]. However, when toluene core PCF is used for SCG, the spectral broadening in toluene-core PCF occurs rapidly in the first centimeters of its length [60], while the effect of high attention of toluene is significant just after few tens centimeters of propagation length. Therefore, short toluene-core PCF can support SCG with the broad bandwidth, and the attenuation of the fiber does not significantly decrease the brightness of the output spectrum. Toluene also has higher linear refractive index than that of silica (Figure 4.1). Thus, if the toluene core PCF is used for SCG applications, the light is strongly confined inside the core region due to the huge difference of refractive indices between the core and cladding. As a result, A_{eff} decreases, and thus, nonlinear coefficient increases. However, the huge difference of refractive indices also causes the multimode operation and decreases the coupling efficiency between toluene core PCF and typical silica fiber.

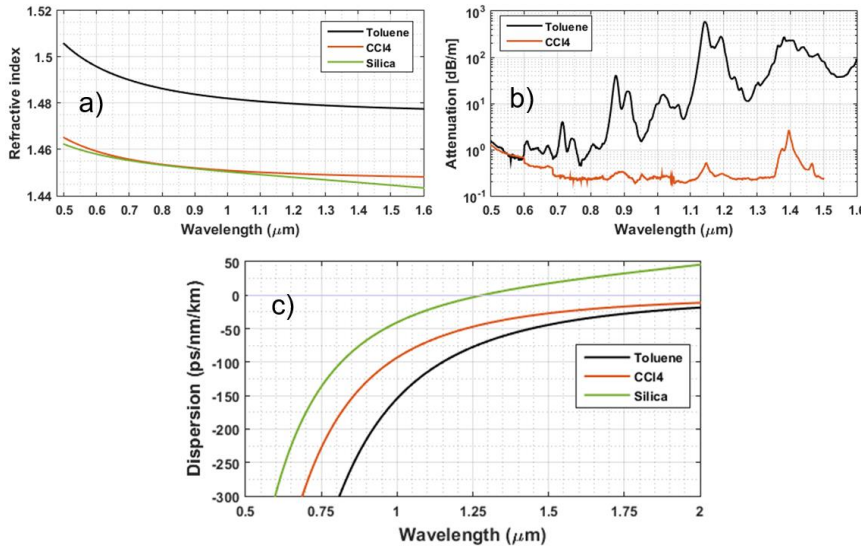

Figure 4.1. Refractive index (a) and attenuation (b) of toluene and CCl_4 [46]. *D* of bulk silica, toluene, and CCl_4 is shown in (c).

Nonlinear refractive index of CCl_4 $n_2 = 1.53\times10^{-19}$ m^2/W at λ=1064 nm [45] and 5 times higher than that of silica ($n_2 = 2.74\times10^{-20}$ m^2/W at λ=1050 nm). A significant advantage of CCl_4 is its high transparency [46, 95]. Therefore, the brightness and bandwidth of SCG in CCl_4-core PCF are not reduced significantly by attenuation of CCl_4.

Toluene and CCl_4 have flat, near-zero, and normal D_m in NIR range, as shown in Figure 4.1. Thus, hollow-core PCF infiltrated with these liquids can offer the flat, near-zero dispersion, which is compatible with commercial femtosecond lasers for SCG applications.

The refractive index of toluene, CCl_4, and fused silica used for numerical modelling may be represented by Sellmeier as given in Eq (4.1):

$$n=\sqrt{1+\frac{B_1\lambda^2}{\lambda^2-C_1}+\frac{B_2\lambda^2}{\lambda^2-C_2}+\frac{B_3\lambda^2}{\lambda^2-C_3}}, \tag{4.1}$$

where B_i and C_i are coefficients.

Table 4.1 show these coefficients for silica, toluene, and CCl_4 in the visible and NIR spectral range.

Table 4.1. The Sellmeier coefficients of the investigated liquids and silica.

Coefficients	**Silica** [61]	**Toluene** [46]	**CCL_4** [46]
B1	0.6694226	1.17477	1.09215
B2	0.4345839	0	0
B3	0.8716947	0	0
C1 (μm^2)	4.4801×10^{-3}	0.01825	0.01187
C2 (μm^2)	1.3285×10^{-2}	0	0
C3 (μm^2)	95.341482	0	0

4.2 Chromatic Dispersion of Photonic Crystal Fibers Infiltrated with Liquids

D of the investigated liquid core PCF depends on the geometrical structure of the fiber and material of the core, i.e. toluene or CCl_4 [59]. The *D* is one of the critical factors for SCG and determines a dynamic for spectral broadening in an optical fiber. For example, in the case of the ultra-short input pulses, the soliton dynamics, e.g., soliton fission, soliton self-frequency shift, are significant mechanisms for spectral broadening in the anomalous *D* regime. Consequently, the output spectrum is not flat and its coherence property is critically reduced by the effect of input noises. In normal *D* regime, SMP, OWB induced by FWM are main contributions to spectral broadening. The effects of input noises are suppressed in the normal *D* regime. Therefore, the coherence is improved [30].

The *D* of liquid core PCFs is calculated using the finite difference eigenmode (FDE) method with various geometrical parameters. i.e., *f* and *Λ*. This method in the frequency domain is used to numerically solve Maxwell's equations in complex for two-dimensional photonic structures, and it is implemented using commercially available Lumerical Mode Solution software [114]. In particular, the cross-section of developed PCF is divided into discrete rectangular cells (Yee cells) [115] – it is called Cartesian style mesh. The fundamental simulation quantities, i.e., material properties and geometrical information, electric and magnetic field, are calculated at each mesh point. In such a case, a matrix of eigenvalues representing the propagation constant, as well as, a matrix of eigenvectors representing the field distribution, are obtained. The boundary condition, as well as, continuity of electric and magnetic field at the cell borders allows to determine the distribution of the electric field and the effective refractive index of the waveguide mode. The boundary condition used for the simulation herein is *perfect matched layer (PML) boundaries*. This boundary condition allows for radiation to propagate out of the computational area without interferometer with the field inside, and boundaries absorb incident light upon them.

The schematic representation of the geometrical structure of the modelled fiber has been shown in Figure 4.2. The structure of the fiber has five rings of air-holes in

the cladding. The diameter of the core is $d_{core} = 2\Lambda$ to ensure the technological feasibility of the analyzed structure. Typically, the relative size of air-holes in the first ring influence critical on the *D*, while outer rings reduce the confinement loss.

After the design of liquid core PCF, the silica hollow core PCFs are fabricated in *Institute of Material Electronic Technology in Warsaw-Poland* by the stack-and-draw technique [116]. The scanning electron microscope (SEM) image of the silica hollow core PCFs are imported to this software as a structure of the investigated fiber, and then, the central core is filled with selected liquid (toluene, CCl_4). The D_m of fused silica, and selected liquid, as well as, their imaginary part of refractive index are used to calculate linear optical properties of investigated PCF.

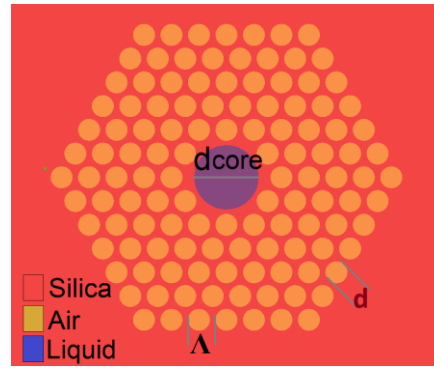

Figure 4.2. Schematic representation of the modeled structure. The analyzed fibers have five rings of air-hole in the cladding and core diameter $d_{core} = 2\Lambda$. The air-core is infiltrated with toluene and carbon tetrachloride.

The air-core of hollow core PCF is selectively infiltrated with toluene and CCl_4. The refractive index of the core is higher than that of the cladding. Thus the light is guided in the core by TIR. The mode number in the optical fiber depends on the difference of refractive indices between core and cladding, and size of the core [80]. The large core PCF infiltrated with the liquids is a multimode fiber. However, the fundamental mode is selectively excited during SCG measurements. Furthermore, the high-order modes do not affect significantly SCG efficiency with short pump pulse (<10 ps) [117]. Therefore, the *D* of the fundamental mode is mainly analyzed in this work.

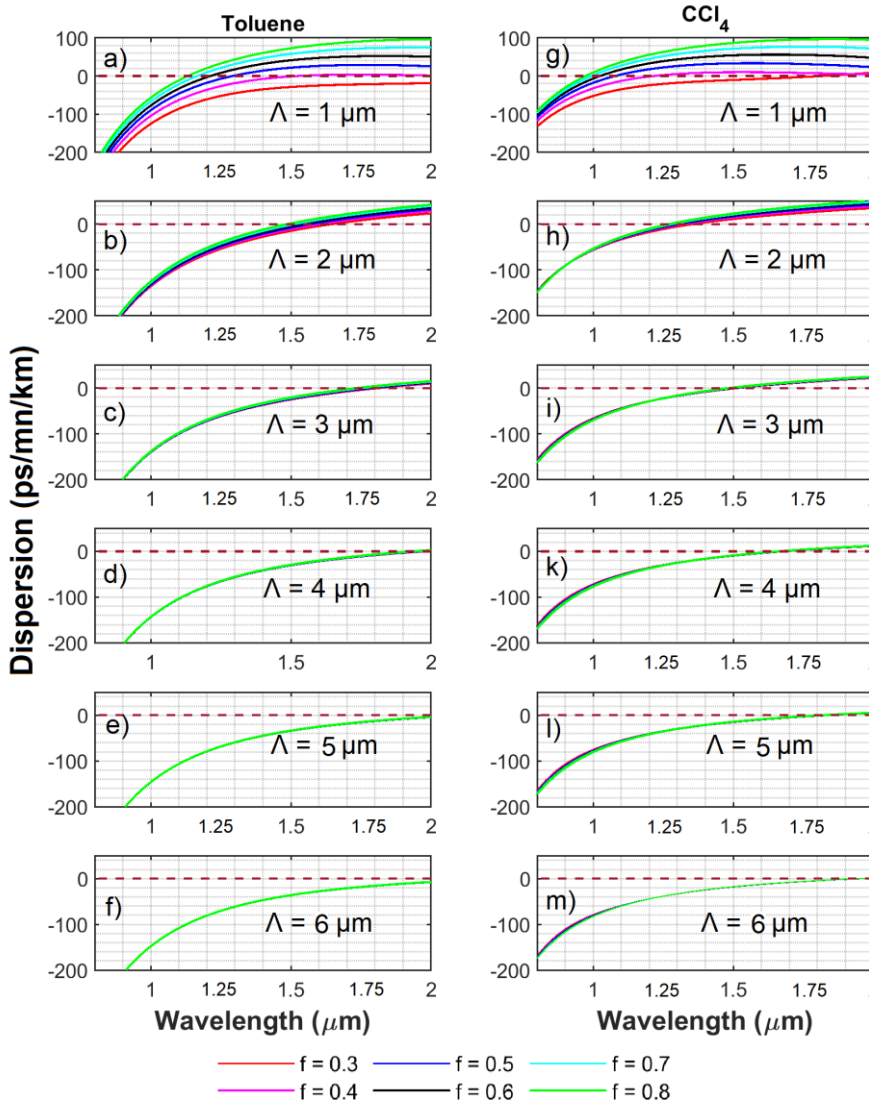

Figure 4.3. The D of toluene (a÷f) and CCl_4-core PCFs (g÷m) with the Λ = 1 ÷ 6 μm, f = 0.3 ÷ 0.8. The core diameter: $d_{core} = 2\Lambda$.

For the design of the fibers, the Λ changes from 1 μm to 6 μm, what corresponds to d_{core} = 2 ÷ 12 μm. The f changes from 0.3 to 0.8. Mogilevtsev *et al.* [118] pointed out that the D depends crucially on the f of PCFs with Λ/λ < 1.5. Therefore, in the case of Λ smaller than 2 μm, the increase of f shifts the D noticeably toward the anomalous regime and blue-shifts the position of ZDWs (Figure 4.3(a) & 4.3(b)). Flat and all-normal D can be obtained with Λ=1, f=0.3 in both toluene and

CCl_4-core PCF. In the case of $\Lambda > 2$ µm, the D moderately shifts with the increase of f. The difference of D_m of toluene and CCl_4 causes a difference of D between CCl_4-core and toluene-core PCF with the same micro-structures. In particular, Figure 4.4 shows the distribution of ZWD of toluene-core and CCl_4-core PCF with various values of Λ and f. The ZDW of toluene-core PCF shifts toward longer wavelengths when compared to that of CCl_4-core PCF with the same geometrical parameters.

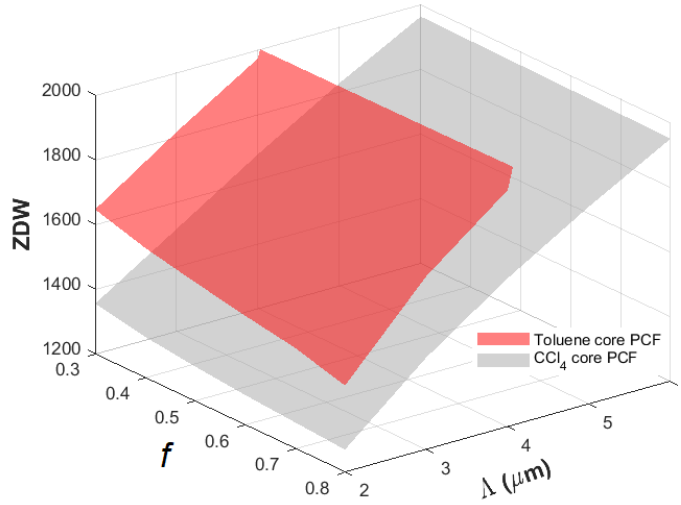

Figure 4.4. Distribution of ZDW with the various values of f and Λ for toluene-core and CCl_4-core PCFs.

The all-normal D of toluene and CCl_4-core PCFs can be obtained in the cases of (i) using PCFs with a small value of Λ, e.g., $\Lambda \leq 1$ µm, and changing the size of air-holes to optimize D; (ii) the large core PCFs ($\Lambda \geq 5$ µm), where D is comparable to the D_m of selected liquid inside the core. In the first case, small core PCFs do not offer high coupling efficiency with standard single mode fiber when an all-fiber SCG system is considered. It is to note that the fibers used for ultra-short pulse delivery have low nonlinearity and low D, i.e., PBG fiber, and large mode area fiber. However, it is impossible to connect the band-gap fiber with liquid core PCF because of the infiltration of liquid to air-holes of the PBG fiber. The large mode area fiber, which possesses low D and nonlinearity, should be dedicated to splicing with a liquid core fiber for all-fiber SCG system. Hence, the large-core PCF infiltrated with liquid, which has an effective mode area close to that of short-pulse delivery fiber, would ensure the high coupling efficiency. Additionally, as shown in Figure 4.3, the liquid core PCF with a $\Lambda \geq 5$ µm and $d_{core} \geq 10$ µm has a normal D regime in NIR range. Therefore, in the following chapters, the large-core PCFs infiltrated with liquids would be used for SCG applications.

4.3 Fabrication of Liquid Core Photonic Crystal Fibers

A conventional fusion splicer has been used for collapsing air-holes in the PCF cladding area. There are known some other methods to selective filling liquid into PCF. In particular, Vieweg *et al.* [57] used the photopolymerization method based on the two-photon direct-laser writing technique to close individual air-hole in the cladding. However, this method only works well for fiber with f close to 1. Its main drawback is a requirement for the high stability of the setup and the precision of air-hole addressing. Huang *et al.* proposed to use UV-adhesive to close the air-holes [119], where a high-pressure pump system was used to push the glue into all air-holes of the fiber. This method is based on the difference of the infiltration speed of the UV-adhesive into air-core and the air-holes in the cladding. Because the air-core diameter is larger than that of air-holes in the cladding, UV-adhesive was filled into the core faster. However, the viscosity of UV-adhesive is very high, e.g. the viscosity of NOA 73 used in [119] is 170 cps [120] while that of water is 1 cps, thus it requires the high pressure and long time to push the glue into the air-holes. Moreover, this method requires the precision of the infiltration length of air-hole with the glue. In this work, the thermal method supported by a conventional fusion splicer is used to collapse and seal all of the air-holes in the cladding [121]. The drawback of this method lack of capability for sealing each air-hole since the fiber is collapsed from the outer to the inner region by the electric arc. However, in the case of closing the whole of air-holes in the cladding area and leaving only the air-core opens, this method is quite simple to implement. This method requires just the precision for the parameters of time and intensity of electric current between electrodes. Thus, a conventional fusion splicer has been used in this work to close all of the air-holes in the cladding of tested fiber, as shown in Figure 4.6.

The fusion splicer is Ericsson FSU 975, which employs two electrodes to initiate an arc, as shown in Figure 4.5. The two electrodes are spaced symmetrically with the fibers in-between to ensure the uniform distribution of the heat in the processed sample. The relative position between fiber and the electrodes is adjusted by the camera's viewing plane. To collapse all of the air-holes in the cladding, the applied intensity of arc and fusing time are 8 mA and 0.2 s, respectively. The core stays opened after the splicing process.

After the splicing process, the collapsed end-faces of the fiber are checked with Polarizing Microscope BX53-P to ensure that the fusion process was successful, i.e., sealed all of the air holes and air-core was still open, as shown in Figure 4.6. Because of the effect of the thermal process, the core diameter of the collapsed facet is reduced. For example, when a hollow core PCF with the Λ = 6.2 μm, f = 0.88, d_{core} = 12 μm, has been used in this splicing process, the d_{core} at the collapsed end-face is reduced to 3 μm (Figure 4.6(c)). The reduction of d_{core} leads to a decrease of the coupling efficiency in the SCG measurement when the light is coupled into the fiber at the collapsed end.

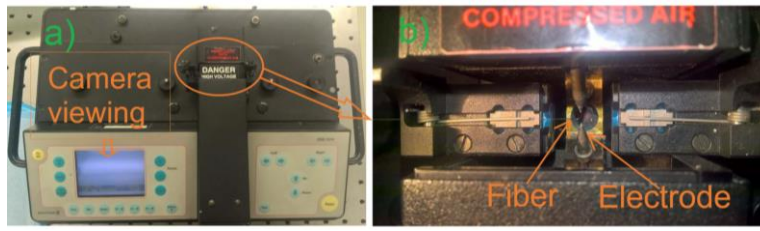

Figure 4.5. Fusion splicer FSU 975 (a) and two electrodes and the fiber (b).

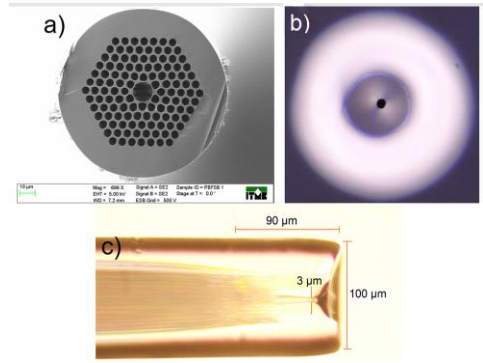

Figure 4.6. The SEM images of hollow core PCF with the Λ = 6.2 µm, f =0.88, d_{core} = 12 µm (a), the end-face (b), the cross-section of collapsed end by fusion splicer (c). The all of air-holes in the cladding were closed. The air-core stayed open, however, it reduced its diameter from 12 µm to 3 µm as a result of heat.

Next, the collapsed end of the fiber is immersed in the liquid reservoir, which contains toluene or CCl_4, as shown in Figure 4.9. The liquid is infiltrated into the core by capillary action. The infiltration time of liquid into the core depends on the size of the core and properties of liquids, i.e. surface tension and liquid's density [122]. The 12 cm of toluene core PCF with a d_{core} = 12 µm needs 5 minutes of infiltration, where 20 cm of CCl_4-core PCF with d_{core} = 9 µm requires 8 minutes. The setup, which is shown in Figure 4.6, allows to observe the process of infiltration into the fiber. The white light from SC source is converged at a point on the fiber near output end-face by micro-objective 20X. The scattered light emitted from the output end-face is collimated by micro-objective 40X. The output end-face of fiber is imaged by the CCD camera. As shown in Figure 4.7(a), the air-holes and the core are gray. When the liquid is filled into the whole core, the core is brighter due to the light scattering (Figure 4.8(b)). Because $n(\lambda)$ of toluene and CCl_4 is higher than that of silica, this fiber can guide the light by TIR, as shown in Figure 4.8 (c).

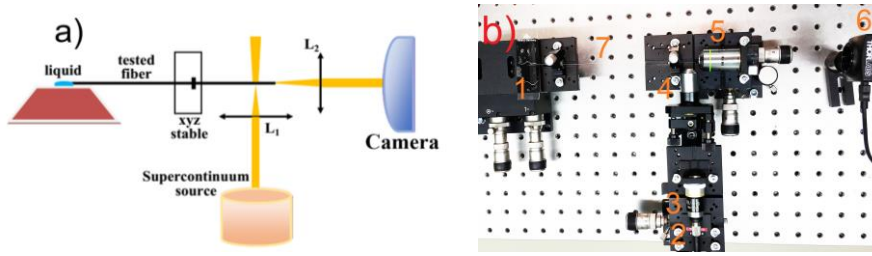

Figure 4.7. Scheme of setup for observation of liquid infiltration into the core (a). The experimental setup (b) contains:

- (1) the liquid (toluene or CCl_4)
- (2) output end the fiber guided the white-light for SC source
- (3) micro-objective collimating the white-light
- (4) micro-objective converges white-light on the fiber
- (5) micro-objective collimating the scattering light from facet of investigated fiber
- (6) CCD camera, the facet of investigated fiber is imaged by the camera.
- (7) the investigated fiber

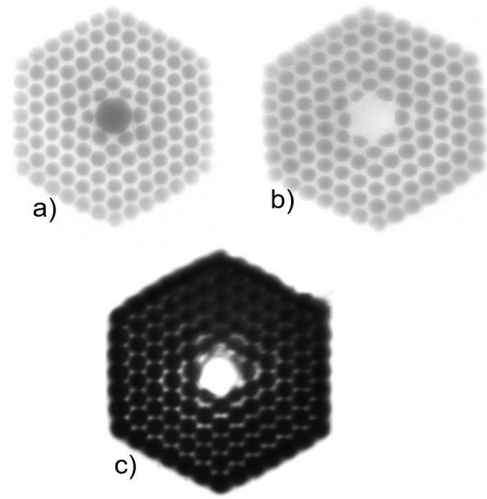

Figure 4.8. Facet of the investigated fiber with air in the core when it is illuminated by scattering light (a). For the nonlinear liquid in the core, the core is brighter than air-holes in the cladding (b). Facet of investigated fiber when the light is guided in the core (c).

Evaporation of toluene and CCl_4 leads to a lack of liquid at the fiber end. Therefore, during each measurement, e.g., *D* and SCG measurements, the collapsed end-face of the fiber is immersed in the reservoir containing liquid (Figure 4.9). The microfluidic pump system is used to supply the liquid into the reservoir.

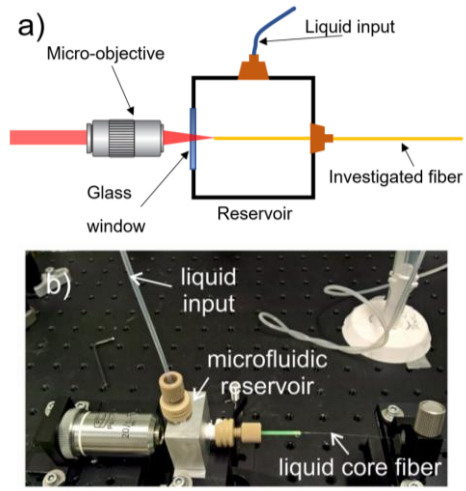

Figure 4.9 Scheme of the reservoir to maintain liquid in the core during *D* and SCG measurement (a). The experimental setup is shown in (b). The glass window is highly transparent and allows the light delivered by micro-objective to couple into the fiber.

The microfluidic structure includes the microfluidic flow controller, which was used to adjust output pressure. The air pressure has been increased in the liquid tank to push it up to the reservoir, as shown in Figure 4.10. For *D* and SCG measurements, the pressure from the microfluidic flow controller is 100 kPa.

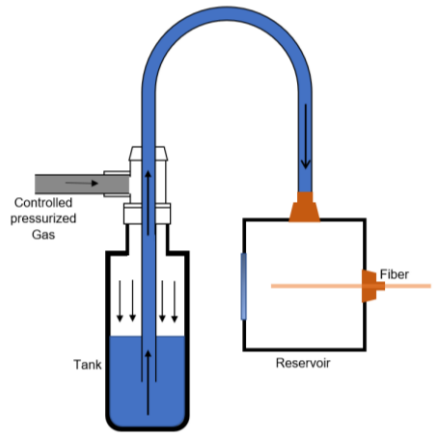

Figure 4.10. Schematic representation of the microfluidic pump with its operating principles.

4.4 Mach-Zehnder Interferometer for Dispersion Measurement

There are some methods for *D* measurement of optical fibers, e.g., time-of-flight method or modulation phase-shift method [123]. However, these methods require a long section of tested optical fiber. Thus, they cannot be used to measure *D* of liquid core fiber because the high attenuation of liquid core fiber results in low intensity of output light. Also, it is challenging to infiltrate liquid into a long fiber sample. Alternatively, a modified Mach–Zehnder interferometer technique [124], based on white-light interferometry and employing a low-resolution spectrometer, makes it possible to measure *D* for a short length of the liquid core PCF.

The experimental setup employing spectral-domain white-light interferometry to measure the *D* of liquid core PCF is shown in Figure 4.11. SC source (Koheras SuperK) emits the white-light in range 450÷2400 nm with an average power of 150 mW. The light from SC source is collimated by micro-objective (MO_1), and then, divided into two parts by a beam splitter. The first part is coupled into the investigated fiber by micro-objective (MO_2). The output light from the investigated fiber is collimated by micro-objective (MO_3) and changes direction by minor (M_1) to beam splitter (BS_2). The second part is delivered to the reference arm. The variable neutral density filter is used to adapt the beam intensity. The optical path of the reference arm is controlled by the translational motion of (M_3) and (M_4) system, which is mounted on the micropositioner. Their positions, as well as, the corresponding spectral signal are recorded. The glass (G) is inserted in the reference arm for compensation of D_m of the glass window of the reservoir. All the components, i.e., micro-objective, variable intensity filter, were characterized and their influence on the *D* measurement of the fiber has been taken into account. The spectrometers are: visible spectrometer (Red Tide, Ocean Optics Inc., Largo, FL, USA) with a wavelength range of 350 ÷1000 nm and infrared spectrometer (AvaSpec-NIR256/512-1.7, Avantes BV, Apeldoorn, The Netherlands) with a wavelength range of 900÷1700 nm.

The Optical Path Difference (*OPD*) between the signal arm and the reference arm is described by:

$$\begin{aligned}\Delta(\lambda) = L_2 + OPD_{MO2} + OPD_R + d_{fiber}(N_a(\lambda)-1) \\ + OPD_{MO3} - L_1 - OPD_{NDF} - OPD_{glass},\end{aligned} \tag{4.2}$$

where L_1 and L_2 denote optical path length in the air of signal and reference arm, respectively, $N_a(\lambda)$ has been named relative group refractive index, OPD_R denotes *OPD* of the reservoir.

OPD of components, such as micro-objectives and variable intensity filters were characterized by Michelson interferometer. The input light from (MO_2) propagates through the glass of the reservoir and then coupled into the core of the fiber. Therefore, the optical path difference of reservoir OPD_R is equal to that of the

glass (OPD_{glass}). The *OPD* of the fiber is described by $d_{fiber}\left(N_a(\lambda)\text{-}1\right)$ and depends on the length of fiber d_{fiber}.

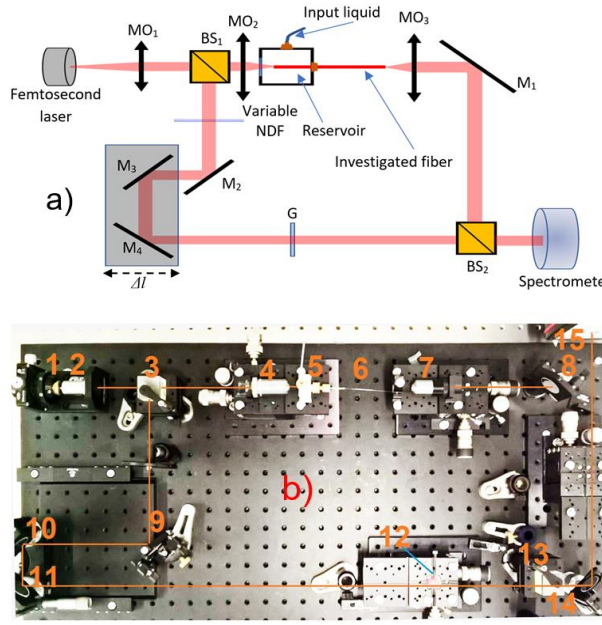

Figure 4.11. The schematic representation of Mach–Zehnder interferometer setup (a). The experimental setup (b) contains:

- (1) the output end of single mode fiber guiding the white-light from a SC source
- (2) micro-objective collimating the light
- (3) beam splitter divides input white-light to the signal arm and reference arm
- (4) Micro-objective couples the light into the fiber
- (5) reservoir
- (6) investigated fiber with a length of 12 cm
- (7) micro-objective collimating output light
- (8) mirror direct signal beam to the splitter
- (9) mirror
- (10,11) mirrors placed on the translation stage
- (12) glass similar to glass in the reservoir
- (13) a beam-splitter
- (14) a mirror directing the light to the spectrometer
- (15) spectrometer

The Mach–Zehnder interferometer in Figure 4.11 has been called as unbalance interferometer, what means that the D of the investigated fiber is not determined by the effective group refractive index of the fiber ($N_{eff}(\lambda)$), but calculated by $N_a(\lambda)$. The relation between $N_{eff}(\lambda)$ and $N_a(\lambda)$ is described in Eq (4.3):

$$N_{eff}(\lambda) = N_a(\lambda) + C, \tag{4.3}$$

where C is an unknown constant.

The derivative of constant C is equal to zero. Therefore, D of the fiber is determined by $N_a(\lambda)$:

$$D = \frac{1}{c}\frac{dN_{eff}}{d\lambda} = \frac{1}{c}\frac{dN_a}{d\lambda}. \tag{4.4}$$

The spectral interference fringes have the largest period at wavelength λ_0, as shown in Figure 4.12, when the optical path difference $\Delta(\lambda_0) = 0$. It gives the difference between path length of signal arm L_1 and reference arm L_2 is a function of λ_0:

$$2\Delta l(\lambda_0) = L_1 - L_2 = OPD_{MO2} + d_{fiber}(N_a(\lambda_0) - 1) + OPD_{MO3} - OPD_{NDF}. \tag{4.5}$$

Therefore, $N_a(\lambda)$ is calculated as a function of deference arm compensation length Δl

$$N_a(\lambda_0) = \frac{2\Delta l(\lambda_0) - OPD_{MO2} - OPD_{MO3} + OPD_{NDF}}{d_{fiber}} + 1. \tag{4.6}$$

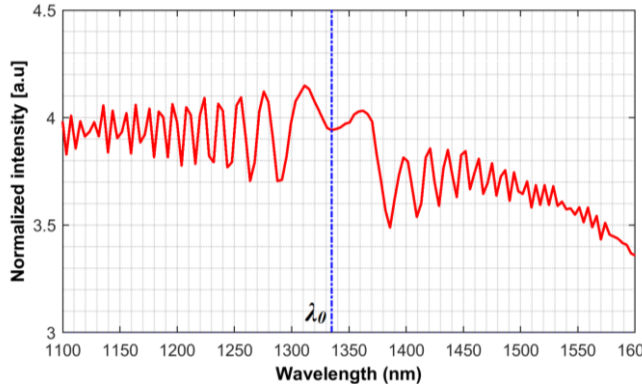

Figure 4.12. An example of the spectral signal recorded by Avantes spectrometer. The position of the largest fringe (the values of λ_0), as well as the respective value of Δl, is recorded to determine the $N_a(\lambda)$.

The deference arm compensation length Δl is the values, which are recorded from the micropositioner with each corresponding spectral signal. Based on experimental data, $N_a(\lambda)$ is calculated by Eq (4.4), and then it is fitted with an approximation curve, for example, the Laurent polynomial as given in Eq (4.7), where $A_{1,2,3,4,5,6}$ are experimentally determined coefficients.

$$N_a(\lambda) = \frac{A_1}{\lambda^4} + \frac{A_2}{\lambda^2} + A_3 + A_4\lambda^2 + A_5\lambda^4. \quad (4.7)$$

The D of the fiber is determined by the first-order derivative of the $N_a(\lambda)$ as described in Eq (4.4).

Toluene-core PCF with (Λ = 6.2 µm, f =0.88, d_{core} = 12 µm) and two CCl_4-core PCFs with (Λ = 4.45 µm, f=0.83, d_{core} = 9.8 µm) and (Λ = 3.1 µm, f=0.65, d_{core} = 5.3 µm) are used to measure D. The experimental data are shown in Figure 4.13. Toluene-core PCF has all-normal D over the investigated wavelength range (500 ÷ 2000 nm), and its value varies -150 ÷ - 5 ps/nm/km. Since toluene is not transparent around a wavelength of 1000 nm. Thus the D of toluene-core PCF has not been measured in this range (near 1000 nm). CCl_4-core PCFs with d_{core} = 9.8 µm and 5.3 µm have ZDW at 1740 and 1440 nm, respectively. The experimental data stay in good agreement with simulation. This agreement confirms that large-core PCFs infiltrated with toluene and CCl_4 are possible to offer normal D over the investigated wavelength range (NIR).

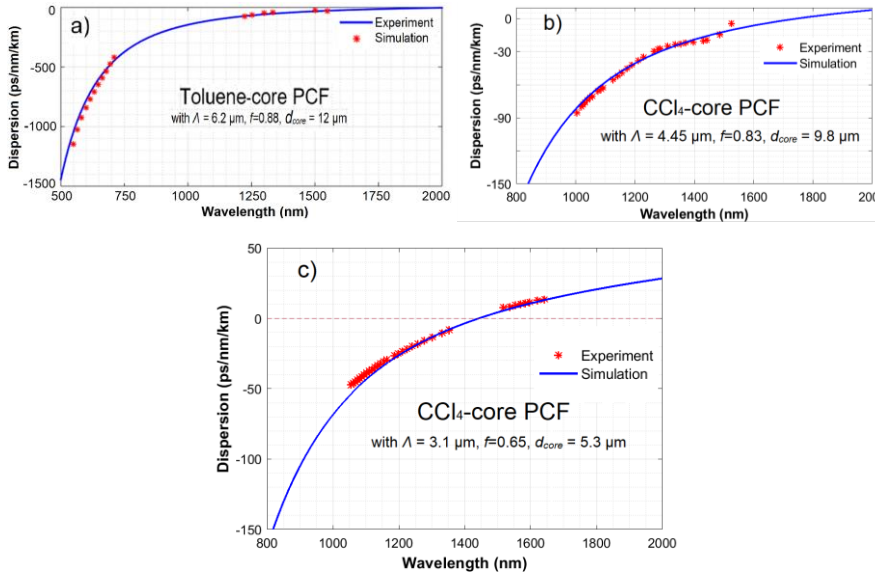

Figure 4.13. Experimental results of D of toluene-core (a) and CCl_4-core PCFs (b), (c). The structure parameters of toluene core PCF is (Λ = 6.2 µm, f =0.88, d_{core} = 12 µm), and CCl_4 core PCFs are (Λ = 4.45 µm, f=0.83, d_{core} = 9.8 µm), and (Λ = 3.1 µm, f=0.65, d_{core} = 5.3 µm). The simulation results are given for reference.

4.5. Losses of Liquid Core Photonic Crystal Fibers

The loss of a liquid core PCF is mostly a sum of confinement and material losses. Confinement loss owing to a finite number of air-holes in the cladding that causes the light to leak. The $n(\lambda)$ of CCl_4 and toluene are higher than silica. Thus, the light is confined strongly in the core. In the other words, the confinement loss of the liquid core PCF is relatively small when compared to material loss, which is the result of the attenuation in liquid. The loss of the fiber is determined numerically by FDE method. As D calculation, the complex refractive index ($n_c(\lambda)$) of toluene and CCl_4 are used:

$$n_c(\lambda) = n(\lambda) + ik(\lambda) \tag{4.8}$$

where $k(\lambda)$ is an imaginary part relates to the absorption of the liquids, as shown in Figure 4.14. The imaginary part does not influence the D of the fiber. However, it has an impact on the attenuation of the liquid core PCF.

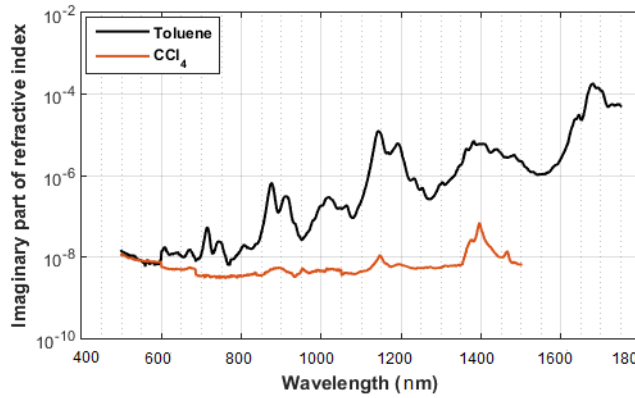

Figure 4.14. $k(\lambda)$ of toluene and CCl_4 [46].

Material loss of liquid core PCF results from the absorption of selected liquid in the core. For example, if the electric field of plane electromagnetic field travels in the liquid in z-direction, the relation between the electric field at $z = 0$ and $z = z_1$ is given in Eq (4.9):

$$\boldsymbol{E}(z_1,t) = \boldsymbol{E}_0 \exp\left[i(\kappa_c z_1 - \omega t)\right], \tag{4.9}$$

where ω is the angular frequency, κ_c is a complex wave number as defined:

$$\kappa_c = \frac{2\pi n_c}{\lambda} = \frac{2\pi(n+ik)}{\lambda}. \tag{4.10}$$

Eq. (4.9) is expanded to:

$$\boldsymbol{E}(z_1,t) = \boldsymbol{E}_0 \exp\left[i\left(\frac{2\pi(n+ik)}{\lambda} - \omega t\right)\right] = \boldsymbol{E}_0 \exp\left(\frac{-2\pi kz}{\lambda}\right)\exp\left(\frac{i2\pi n}{\lambda} - \omega t\right). \tag{4.11}$$

The relation between intensity at $z = 0$ and at $z = z_1$ is:

$$\frac{I}{I_0} = exp\left(\frac{-4\pi k}{\lambda}\right). \tag{4.12}$$

Therefore, the absorption coefficient α of these liquids, that relates to material loss, can be determined through the $k(\lambda)$, as given in Eq (4.13):

$$\alpha[\text{dB/m}] = -10\log\left(\frac{I}{I_0}\right) \Rightarrow \alpha[\text{dB/m}] = 10\log\left[\exp\left(\frac{4\pi k}{\lambda}\right)\right]. \tag{4.13}$$

The absorption coefficient α of toluene-core PCF and CCl_4-core PCF are shown in Figure 4.14.

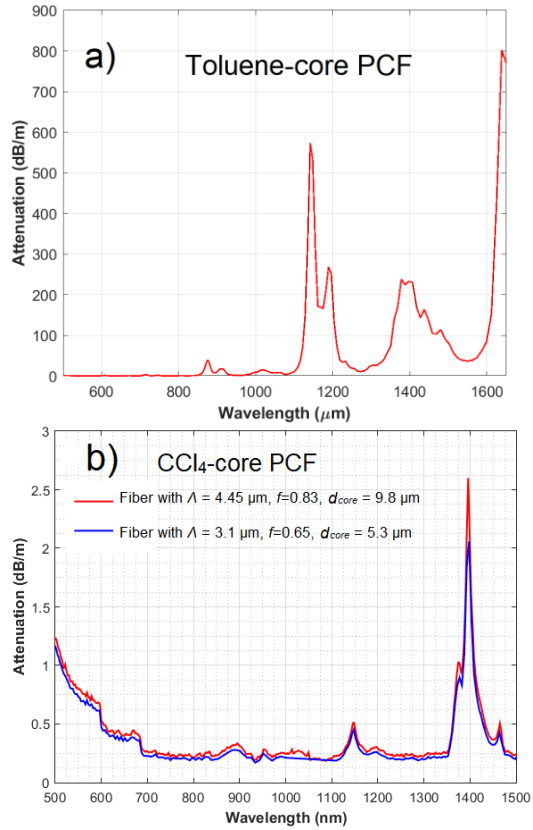

Figure 4.15. The numerical calculation of attenuation of toluene-core PCF (a) and CCl_4-core PCF (b). The structure parameters of toluene-core PCF is Λ = 6.2 µm, f =0.88, d_{core} = 12 µm and CCl_4-core PCFs are Λ = 4.45 µm, f = 0.83, d_{core} = 9.8 µm and Λ = 3.1 µm, f = 0.65, d_{core} = 5.3 µm.

As shown in Figure 4.15, the attenuation characteristics of toluene and CCl_4-core PCFs follow the material losses of liquids. Toluene shows relatively low transparency in NIR, therefore the loss of toluene core PCF is high when compared to that of CCl_4-core PCFs. The peak of the attenuation at λ = 1140 nm is around 600 dB/m. The high attenuation of toluene-core PCF leads to a decrease of energy in the fiber since a majority part of energy is absorbed by toluene and transforms into heat. As a result, brightness and spectral bandwidth of SCG in toluene-core PCF may be decreased. The attenuation of CCl_4-core PCFs are relatively small, the peak of attenuation is around 2.5 dB/m. The low attenuation of CCl_4-core PCF allows to use the long fiber to obtain the SCG with broad spectral bandwidth.

4.6. Conclusion

The linear optical properties of toluene and CCl_4-core PCFs have been studied. The results in this chapter support to prove **Thesis 1.** The silica hollow core PCFs infiltrated with nonlinear liquids can offer flat near-zero all-normal dispersion in NIR range for SCG applications. *D* characteristics of the liquid core PCFs have been modified by changing the structure parameters. The all-normal *D* over the investigated wavelength range of 0.5 ÷ 2 μm can be achieved by using either the small-core PCF (Λ < 1 μm) or the large-core PCF (Λ > 5 μm).

To fill only the core with liquid, the conventional fusion splicer is used to close all of the air-holes in the cladding. Next, the collapsed end of the fiber is immersed in the liquid reservoir. The liquid infiltrates into only the core by capillary action.

D characteristics of the investigated fibers are measured by Mach–Zehnder interferometer connected with a microfluidic pump system. Toluene-core PCF (d_{core} = 12 μm) has value of *D* varied -150 ÷ -5 ps/nm/km in wavelength range of 1000 ÷ 2000 nm. Two CCl_4-core PCFs with d_{core} = 9.8 μm and 5.3 μm are also discussed. Their ZDWs are at 1740 nm and 1440 nm, respectively.

The losses of investigated fibers are also analyzed by the numerical method. The toluene-core PCF has relatively high attenuation, while CCl_4-core PCFs have relatively low attenuation in NIR range with the peak of attenuation of 2 dB/m at the wavelength of 1400 nm.

With the flexibility of structure design to optimize the *D* and high nonlinear refractive indices of selected liquids, the toluene-core and CCl_4-core PCFs may offer broad SC spectra. In the following chapters, SCG in these fibers would be theoretically and experimentally discussed. The linear properties of toluene-core and CCl_4-core PCFs would be used for SCG analysis.

5 Supercontinuum Generation in Photonic Crystal Fiber Infiltrated with Toluene

This chapter is devoted to measurement and numerical simulation of SCG in toluene-core PCF with a femtosecond laser as a pump source. The results shown in this chapter is based on paper [A1].

The investigated fiber is a hollow core PCF, which is fabricated by the stack-and-draw method [116], and then selectively filled toluene into the core. The fiber has d_{core} = 12 µm, Λ = 6.2 µm, and f = 0.88 (Figure 5.1). SCG in this fiber is numerically analyzed and then verified by an experimental setup with a femtosecond pump laser. The laser has a central wavelength of 1030 nm and 400 fs duration of the pulse. Toluene has relatively low transmittance in the NIR. Thus, the laser source with a longer central wavelength of the pulse, e.g., 1560 nm, is not used as a pump source. The high attenuation leads to a decrease of nonlinear coefficient resulting in limitation of spectral bandwidth and brightness of the output spectrum. The dynamics of SCG in this fiber is revealed to stay in a good agreement with established state-of-the-art in nonlinear fiber optics.

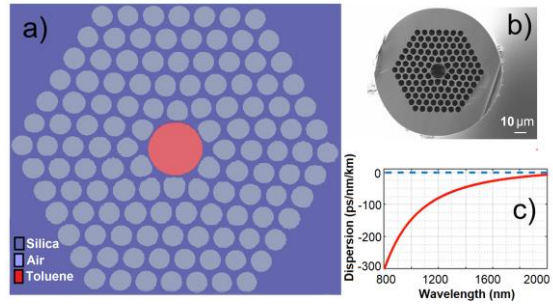

Figure 5.1. Toluene-core structure (a). SEM of hollow core silica which used for selective filling toluene into the core (b). *D* of toluene-core PCF (c).

The first observation of the SCG in toluene core step-index fiber was reported in [52] with a laser source, which has a pulse duration of 18 ps and the central wavelength at 532 nm. The authors used high pulse energy (around 200 nJ) to generate spectral bandwidth from 550 to 870 nm, which was induced by Raman-Kerr scattering. It must be noted that if a long pulse (order of picoseconds) is coupled into the nonlinear fiber, MI noise critically reduces the level of coherence of SCG. To suppress the effect of MI, and thus, to increase the coherence of SCG, the sub-picosecond pulse should be used.

5.1 Simulation of Supercontinuum Generation in Toluene-core Photonic Crystal Fiber

Modeling nonlinear pulse propagation in the large core PCF infiltrated with toluene is analyzed by solving GNLSE, as shown in Eq (2.42) in Chapter 2:

$$\frac{\partial A}{\partial z}+\frac{\alpha}{2}A+\sum_{k=1}\frac{(i)^{k-1}}{k!}\frac{\beta_k\partial^{(k)}A(z,t)}{\partial t^k}=i\gamma\left(1+\frac{i}{\omega_0}\frac{\partial}{\partial t}\right)\left(A(z,t)\int_{-\infty}^{\infty}R(t')\left|A(z,t-t')\right|^2dt'\right). \quad (2.42)$$

Implementing the change of variable $T=t-\beta_1 z$ to transform into the co-moving frame at envelope group v_g. Eq (2.42) is rewritten in the form:

$$\frac{\partial A}{\partial z}+\frac{\alpha}{2}A-\sum_{k\geq 2}\frac{i^{k+1}}{k!}\beta_k\frac{\partial^k A}{\partial T^k}=i\gamma\left(1+i\tau_{shock}\frac{\partial}{\partial T}\right)\times\left(A(z,T)\int_{-\infty}^{\infty}R(T')\left|A(z,T-T')\right|^2dT'\right), \quad (5.1)$$

where $\tau_{shock}=1/\omega_0$ corresponds to the D of nonlinearity, i.e., self-steepening and optical shock formation.

The Eq (5.1) includes several time derivatives, which are only calculated approximately in the discrete numerical case with a finite number of the sample point. Therefore, the use of GNLSE in time-domain leads to numerical errors. However, it is possible to avoid these derivatives using Fourier transform for Eq (5.1) with $\partial/\partial T\leftrightarrow -i(\omega-\omega_0)$. Moreover, in the frequency domain, it is possible to directly use the frequency-dependency of *D*, attenuation, and A_{eff} of the investigated fiber. Eq (5.1) is given in the frequency domain according to Eq (5.2):

$$\partial_z\tilde{A}-\mathrm{i}\tilde{\beta}(\omega)\tilde{A}+\frac{\tilde{\alpha}(\omega)}{2}\tilde{A}=\mathrm{i}\gamma\left(1+\frac{\omega-\omega_0}{\omega_0}\right)\tilde{A}\mathcal{F}\left[\int_{-\infty}^{\infty}R(T')\left|A\right|^2(T-T')dT'\right]. \quad (5.2)$$

The left side of Eq (5.2) describes linear propagation effects. $\tilde{\alpha}$ and $\tilde{\beta}$ is determined from attenuation and *D* of the fiber, respectively. $\tilde{\beta}(\omega)=\beta(\omega)-\beta_0(\omega)-\omega\left.\frac{\partial\beta}{\partial\omega}\right|_{\omega=\omega_0}$. In the frequency domain, these linear properties have been described in Chapter 4. The *D* of the toluene-core PCF was measured and shown in Figure 4.13(a).

The right side of the equation models nonlinear effects. These effects depend on the nonlinear optical response of toluene that is determined by the combination of bound-electronic and nuclear contribution, as shown in Chapter 3. Table 5.1 shows the nonlinear parameters of these contributions, where the subscripts *el*, *d*, *l*,

c indicate the bound-electronic, molecular reorientation, molecular interaction, and collision-induced, respectively. τ_r and τ_f are rise time and fall time.

Tab 5.1. Parameters of the response function of toluene [62].

$n_{2,el}$ (10-19 m2/W)	$n_{2,c}$ (10-19 m2/W)	$\tau_{r,c}$ (ps) $\tau_{f,c}$ (ps)	$n_{2,l}$ (10-19 m2/W)	ω_0 (THz) σ (THz)	$\tau_{f,l}$ (ps)	$n_{2,d}$ (10-19 m2/W)	$\tau_{r,d}$ (ps) $\tau_{f,d}$ (ps)
0.6	0.12	0.25 0.2	1.2	11 8	0.35	3	0.25 2.1

The Raman response function in Eq (5.1) is given by:

$$R(t) = (1 - f_R)\delta(t) + f_R R_1(t), \tag{5.3}$$

where f_R is a fraction contribution of the delayed contribution, which is a fraction of nuclear contribution to the nonlinear optical response of toluene. Based on Table 5.1, f_R of toluene is around 0.87. $R_1(t)$ represents the delayed nonlinear response, as shown in Eq (3.4) in Chapter 3.

$$R_1(t) = \frac{1}{N}\left[n_{2l} C_{2l} e^{-t/t_{fl}} \int_0^{\infty} \frac{\sin(\omega t)}{\omega} g(\omega) d\omega + \sum_{k=c,d} n_{2k} C_{2k} \left(1 - e^{-t/t_{rk}}\right) e^{-t/t_{fk}}\right] \Theta(t), \tag{3.4}$$

where $N = n_{2,el} + n_{2,l} + n_{2,c} + n_{2,d}$.

The A_{eff} depends on the wavelength, the contrast of refractive indices between core and cladding, and the size of the core. The use of the large core PCF leads to a an increase of A_{eff}, and thus, decreases the nonlinear coefficient. However, the nonlinear coefficient of toluene-core PCF can be compensated by the high nonlinear refractive index of toluene. For the investigated fiber, the nonlinear coefficient γ varies of 128 ÷142 $W^{-1}km^{-1}$ in the wavelength range of 500 ÷ 2000 nm, as shown in Figure 5.2. The γ is relatively small when compared to that of e.g., soft-glass fibers [40, 41]. However, it is relatively high when compared to the nonlinear coefficient of the previously reported larger-mode area fibers for SCG [125].

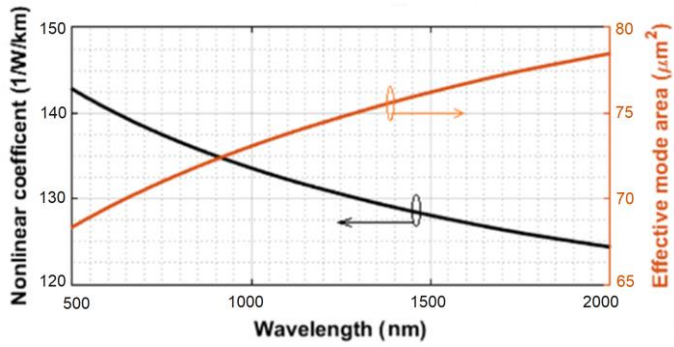

Figure 5.2. Nonlinear coefficient and A_{eff} of toluene-core PCF.

Eq (5.2) is calculated with the initial pulse, which has a temporal shape described by the Gaussian function, as given in Eq (5.4):

$$A(0,t) = \sqrt{P_0}\exp\left(\frac{T^2}{2T_0^2}\right) \tag{5.4}$$

where P_0, T_0 are peak power and duration of the pulse, respectively.

The initial pulse parameters are as follows: 400 fs pulse duration, the central wavelength at 1030 nm, the repetition rate of 10 MHz. The input pulse energies vary from 1 nJ to 10 nJ, corresponding to a peak power of 2.5 kW ÷ 25 kW and average power of the pulse of 1 mW ÷ 10 mW.

Figure 5.3 shows spectral broadening with various input pulse energies at the 10 cm of propagation. SPM is the pure contribution to spectral broadening with input pulse energy up to 4 nJ. With further high input pulse energy, e.g. 10 nJ, the spectral broadening is a result of SPM at the central range of the spectrum and OWB at the edges.

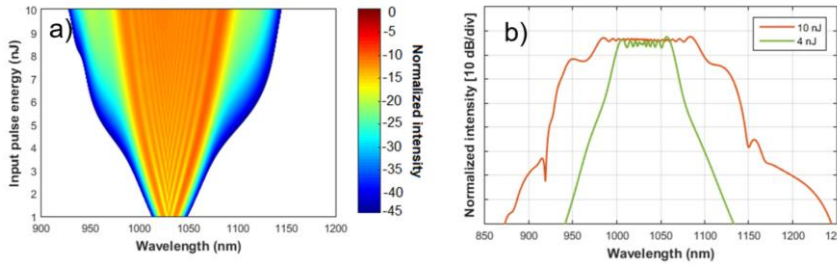

Figure 5.3. The evolution and spectra of SCG with 10cm fiber, 1030 nm pump wavelength 400 fs duration of the pulse. Evolution of SCG with various pulse energies (a), spectra of SCG with 4, and 10 nJ input pulse energies (b).

In the case of input pulse energy 10 nJ, as shown in Figure 5.4, SPM is the main contribution to spectral broadening during initial propagation in the fiber. The temporal profile shows the characteristic of SPM that is S-shape feature with a red-shift on the leading edge and blue-shift on the trailing pulse edge. OWB begins appearing at 6 cm of propagation and creates the new wavelength band around 950 nm. The effects of optical self-steepening lead to spectrum having a slight asymmetry spectrum toward the short wavelength, thus OWB occurs earlier on the short wavelength side. After 7 cm of propagation, OWB occurs for both the edges and another new wavelength band is generated around 1150 nm. During further propagation, the energy is redistributed from central to wings of the spectrum. However, no new wavelengths are generated. The slope of normal D limits the spectrum at the short-wavelength edge. The further increasing input energy, spectral

broadening can continue at the red-shifted wavelengths (leading edge) due to favorably flat *D*.

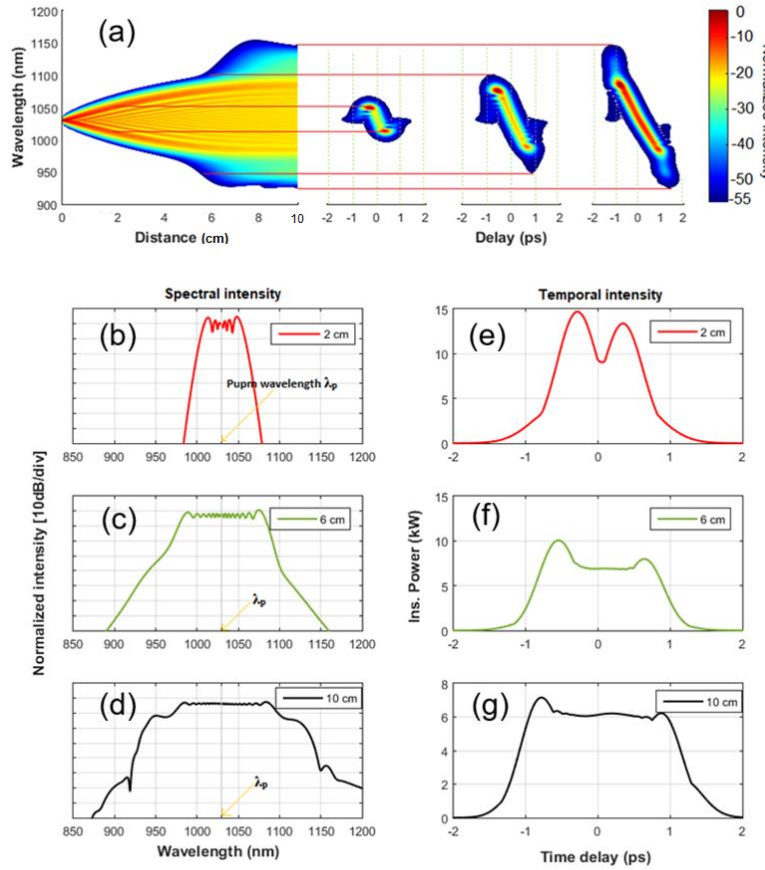

Figure 5.4. Evolution of SCG in toluene-core PCF with 10 nJ pulse energy, 1030 nm pump wavelength, 400 fs duration of the pulse with various fiber length (a), spectral intensity (b,c,d) and temporal intensity (e,f,g). The color bar indicates the normalized intensity on a logarithmic scale.

5.2 Measurements of Supercontinuum Generation

Toluene has a high nonlinear refractive index, but its attenuation is also high in NIR range. The high attenuation leads to that a part of energy would be absorbed, resulting in a decrease of spectral broadening. Thus, a femtosecond laser with a short central wavelength of the pulse should be used as a pump source. For measurements of SCG in the toluene-core PCF, the laser source is BlueCut Femtosecond Fiber Laser

with a central wavelength at 1030 nm, 400 fs duration of the pulse, and 10 MHz repetition. The length of the fiber is 10 cm. Thorlbab CCS 175 and Avantes AvaSpec-NIR512 with a sensitivity range of 500÷1000 nm and 900÷1700 nm are used for recording received spectra.

The light is coupled into the collapsed end of the fiber, which is immersed in the toluene reservoir to avoid the lack of toluene at the input end-face, as shown in Figure 5.5. However, the relatively long distance between the in-coupling point and the fiber at the front faces, imposed by the toluene reservoir, requires using of 10X miro-objective for coupling the light into the. This, in turn, gives the beam diameter of around 16 μm, much larger than the size of collapsed core (around 3 μm), resulting in further limitation of coupling efficiency, approximately 16% for setup in Figure 5.5.

Investigated fiber allows for the multimode operation. However, high-order modes do not influence significantly on the spectral broadening with the duration of pump pulse smaller than 10 ps [117]. Also, in the SCG measurement, 10X mico-objective with the relative small numerical aperture (NA= 0.25, NA of 40X lens is 0.4) allows to excite the fundamental mode in the fiber structure. The intensity profile of the far-field of the output beam is fitted with a Gaussian function (Figure 5.6). This work is to confirm that the investigated fiber can support a single mode operation during measurements of the SCG. Therefore, the results of SCG simulation with the scalar (single mode) model is used to compare with the experimental results.

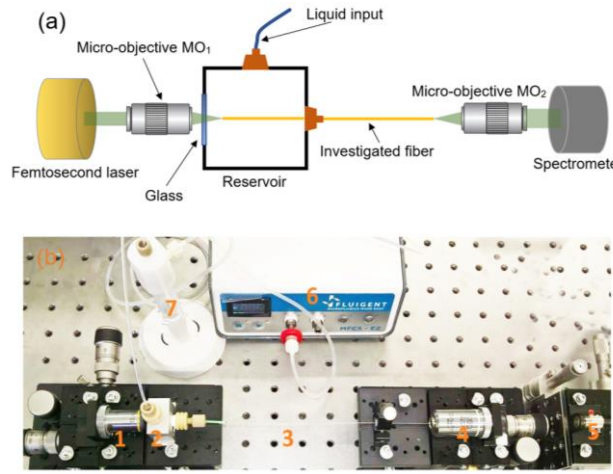

Figure 5.5. Scheme of setup used for measurement SCG setup (a), the image of the setup (b) with 1 - Micro-objective MO_1, 2 - reservoir, 3 - investigated fiber, 4 - Micro-objective MO_2, 5 - multimode fiber connected with a spectrometer, 6 – microfluidic flow controller, 7 – tank provides liquid for the reservoir.

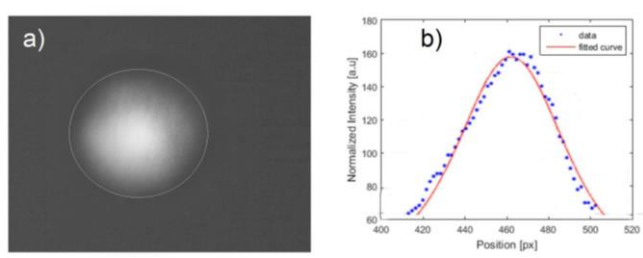

Figure 5.6. Far-field image of the effectively single mode beam at the output of toluene-core PCF (a), a central cross-section of the beam intensity profile along with Gaussian curve fit (b).

The experimental results of SCG in toluene-core PCF are shown in Figure 5.7. The spectral broadening with an input pulse energy of 4 nJ is induced by SPM and covers from 1000 to 1075 nm. This spectrum has symmetry around pump wavelength. The spectrum of SCG with an input pulse energy of 10 nJ broads from 950 to 1100 nm.

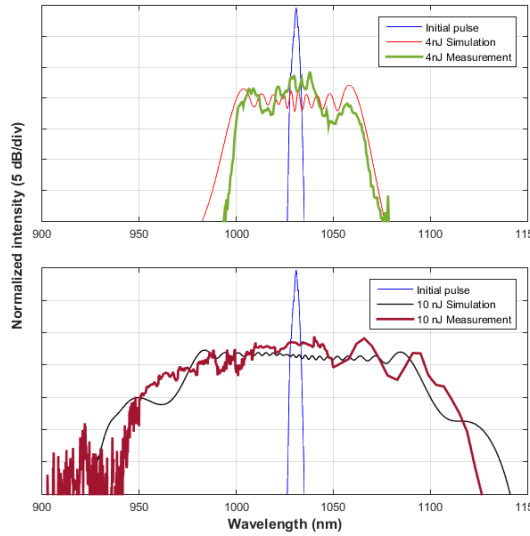

Figure 5.8. Experimental result of SCG in toluene core PCF pumped with a laser source having 400 fs duration of the pulse, 4 nJ and 10 nJ input pulse energies, 1030 nm central wavelength. The simulated results are shown for reference.

The experimental results show a good agreement with the simulation results considering the spectral width and flat of the spectrum. The noise that appears in the experimental spectrum is reasonable for measurement performed with a compact,

Czerny-Turner CCD-based spectrometer. Further broadening is pump power-limited in relation to the thermal properties of the proposed fiber setup. Due to the high input pulse energy, the thermal effects, e.g. combustion of toluene at the input end of the fiber, leads to a decrease of coupling efficiency. Therefore, 10 nJ is the maximum incident pulse energy for SCG measurement in this work.

The experimental results of SCG in the toluene-core PCF match very well those the simulation. Therefore, it is possible to conclude that the spectrum of observed SCG is induced by SPM and OWB. As shown in [58], the all-normal dispersion SCG generated by femtosecond laser and low peak power in short length of fiber has the potential for coherence. The level of coherence of SCG spectrum also depends on the noise appearing during propagation, such as Raman noise, polarization noise, shot-to-shot noise, and amplitude noise of laser source. If only shot-to-shot noise is taken into account, the all-normal dispersion SCG pumped by a femtosecond laser shows high coherence. However, unfortunately, the investigated fiber does not have any intentional birefringence, thus the polarization noise critically reduces the coherence of SCG [126]. Also, the amplitude noise of BlueCut laser is around 1% rms (root-mean-square) [127], therefore, amplitude noise is also a significant cause for the degradation of coherence of observed SCG [128]. These noises can be suppressed by using the femtosecond laser with the short duration of a pulse, such as Menlo Femtosecond Fiber Laser with 90 fs duration of the pulse [129].

5.3 Conclusion

The all-normal dispersion SCG in toluene-core PCF was observed with a femtosecond laser source, which has a central wavelength at 1030 nm and 400 fs duration of the pulse. The observed spectrum covers the range from 950 to 1100 nm. The results of this chapter support to prove **Thesis 1**, that it is possible to use the liquid core PCF for all-normal dispersion SCG.

The toluene-core PCFs can offer reasonable, but not record-high broadening, when pumped with low energy sub-picosecond pulses, typical for fiber femtosecond oscillators with simple 1 or 2 stage amplification systems. The main reason for the moderate spectral bandwidth of observed SCG is a relatively low nonlinear coefficient related to the assumed large A_{eff} and high attenuation of toluene. The high attenuation also leads to the thermal effects, and thus, limitation of input pulse energy. The further broad spectral bandwidth can achieve if the toluene-core PCF with reduced core diameter and optimization D, e.g., further flat and low-value, is used for SCG applications.

The use of liquid core PCF with low attenuation liquids, such as CCl_4-core fibers, are also promising approaches for broadband SCG. Although CCl_4 has lower nonlinear refractive index than that of toluene, low attenuation of CCl_4 allows to use long fiber samples to compensate for its low nonlinearity. Therefore, it can offer broad spectral bandwidth. In the following chapter, SCG in CCl_4—core PCFs will be studied theoretically and experimentally.

6 Supercontinuum Generation in Photonic Crystal Fiber Infiltrated with Carbon-tetrachloride

In this chapter, SC spectra are measured in CCl_4-PCFs with femtosecond lasers as pump sources. Work presented in this chapter has been published in [A2,A3].

As has been shown in Chapter 3, CCl_4 is highly transparent in NIR and MIR range. Its nonlinear refractive index is five times higher than that of silica. Thus, CCl_4 is an interesting liquid for SCG. In this work, two structures of CCl_4-core PCFs are used, as shown in Figure 6.1. The first one - named $\#F_1$ fiber - has d_{core} = 9.8 µm, Λ = 4.45 µm, while the second one - name $\#F_2$ fiber – has d_{core} = 5.3 µm, Λ = 3.1 µm. Their linear properties, i.e., D, attenuation, A_{eff}, have been already calculated in chapter 4.

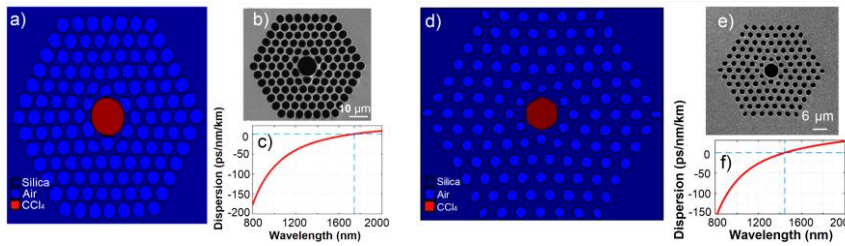

Figure 6.1. The image of $\#F_1$ fiber with d_{core} = 9.8 µm, Λ = 4.45 µm (a), the SEM of $\#F_1$ fiber without CCl_4 (b), D of $\#F_1$ fiber with ZWD at 1740 nm (c). The structure $\#F_2$ with d_{core} = 5.3 µm, Λ = 3.1 µm (d), SEM of $\#F_2$ (e) and D $\#F_2$ with ZDW at 1440 nm (f).

The SCG for the $\#F_1$ has been observed and analyzed with BlueCut Femtosecond Fiber Laser (central wavelength of 1030 nm, 400 fs duration) and Menlo Femtosecond Fiber Laser (1560 wavelength, 90 fs duration). Next, the anomalous dispersion SCG in $\#F_2$ has been observed with the Menlo Femtosecond Fiber Laser as a pump source.

6.1 Simulation of Supercontinuum Generation in Carbon-Tetrachloride-Core Photonic Crystal Fiber

CCl_4 has a nonlinear refractive index $n_2 = 1.53\times10^{-19}$ m^2/W [45]. The nonlinear response is contributed by instantaneous mechanism, i.e. bound-electronic and collision-induced [62]. The Raman oscillations is also a considerable contribution to the nonlinear response function of CCl_4 with input pulse below 100 fs [49]. The nonlinear response parameters of CCl_4 are shown in Table 6.1, where the subscripts *el, d, l, c, R* indicate the bound-electronic, molecular reorientation, molecular interaction, collision-induced, Raman oscillations, respectively. Molecular reorientation and interaction response vanish in CCl_4 because its molecules are highly symmetric with zero polarizability anisotropy.

Table 6.1. Parameters of the response function of carbon tetrachloride [49, 62].

$n_{2,el}$ (10^{-19} m^2/W)	$n_{2,c}$ (10^{-19} m^2/W)	$n_{2,R}$ (10^{-19} m^2/W)	$\tau_{r,c}$ (ps) $\tau_{f,c}$ (ps)	$n_{2,l}$	ω_0 σ	$\tau_{f,l}$	$n_{2,d}$	$\tau_{r,d}$ $\tau_{f,d}$
0.48	0.2	0.16	0.1 0.15	0	NA NA	NA	0	NA NA

CCl_4 has high transparency, thus CCl_4-core PCF offers relatively low attenuation when compared to that of toluene-core fiber. The low attenuation allows to use the long fiber sample for SCG. As shown in Chapter 4, the *D* of $\#F_1$ fiber is in normal regime up to 1740 nm wavelength. The reduction of d_{core} causes blue-shifting of ZDW and decreasing of the A_{eff}. $\#F_2$ fiber has ZDW at 1440 nm, thus this fiber can offer SCG induced by soliton dynamics.

The numerical analysis of SCG in CCl_4-core PCFs is implemented by solving GNLSE. Raman response function $R_1(t)$ has been determined as a sum of molecular contribution, as commented in Chapter 3. The Raman oscillation is a contribution with the duration of input pulse below 100 fs [130,131]. In the case of input pulse with a duration larger 100 fs, $R_1(t)$ is a result induced by the collision-induced contribution [62]:

$$R_1(t) = n_{2c}C_{2c}\left(1-e^{-t'/t_{rc}}\right)e^{-t'/t_{fc}}\Theta(t), \tag{6.1}$$

where C_{2c} is normalized constant.

In the case of input pulse with a duration shorter 100 fs, $R_1(t)$ is the sum of collision-induced and Raman oscillation [49,62]:

$$R_1(t) = n_{2c}C_{2c}\left(1-e^{-t'/t_{rc}}\right)e^{-t'/t_{fc}}\Theta(t) + n_{2R}\,\mathrm{Im}\left(F^{-1}\left\{S(\omega)\right\}\right)\Theta(t), \tag{6.2}$$

where $F^{-1}\{S(\omega)\}$ is inverse Fourier transform of Raman spectrum *S(ω)* of CCl_4 and normalized: $\int Im\left(F^{-1}\{S(\omega)\}\right)\Theta(t)dt = 1$. The Raman spectrum *S(ω)* of CCl_4 is provided in [49].

6.1.1 Normal Dispersion Supercontinuum Generation in Carbon-Tetrachloride-Core Photonic Crystal Fiber

SCG in CCl_4-core PCFs is analyzed with two sorts of input pulses named B-pulse and M-pulse. The parameters of these pulses are shown in Table 6.2. The B-pulse generated from Blue-cut femtosecond fiber laser with high output power (up to 10 W). This feature offers flexibility in studying SCG in various nonlinear liquid core PCF. M-pulse with central wavelength is near ZDWs of the investigated fibers, thus it can offer broad SC spectra with low input peak power.

Table 6.2. Parameter of initial pulse for SCG in CCl_4-core PCF.

Pulse	Central wavelength	Pulse duration	Repetition
B-pulse	1030 nm	400 fs	10 MHz
M-pulse	1560 nm	90 fs	100 MHz

When *#F1* fiber is pumped by B-pulse with 25 nJ pulse energy (62.5 kW peak power), SPM and OWB are the main contributions to SCG, as shown in Figure 6.2. At the beginning of propagation length, the spectral broadening is induced by SMP which has the temporal profile of S-shape, and the appearance of peaks in the spectrum (Figure 6.2(b)). During further propagation, the onset of OWB is at 7 cm. FWM process [80] also creates a new wavelength band which contributed to OWB. The wavelength band generated by FWM is estimated using Eq (6.3) [80]:

$$\omega_{\mathrm{FWM}} = 2\omega_{\mathrm{pump}} - \omega_{\mathrm{seed}} \Leftrightarrow \frac{1}{\lambda_{\mathrm{FWM}}} = \frac{2}{\lambda_{\mathrm{pump}}} - \frac{1}{\lambda_{\mathrm{seed}}}. \tag{6.3}$$

The wavelength λ=950 nm, which generated by SPM, acts as a pump wavelength, and the pulse tail 1030 nm acts as a seed. The component generated by FWM is around 880 nm. After further propagation, the OWB also generated the new wavelength at leading pulse edge (around 1250 nm wavelength).

Performance of the spectrum broadening at the 20 cm propagation for various input pulse energies is shown in Figure 6.3. In the case of low-input pulse energy (below 4 nJ), SCG is relatively narrow and solely induced by SMP. The OWB contributes significantly to spectral broadening when input pulse energy higher than 7

nJ. With input pulse energy 25 nJ, the spectral broadening in $\#F_1$ fiber covers in range of 850 nm ÷ 1250 nm wavelength.

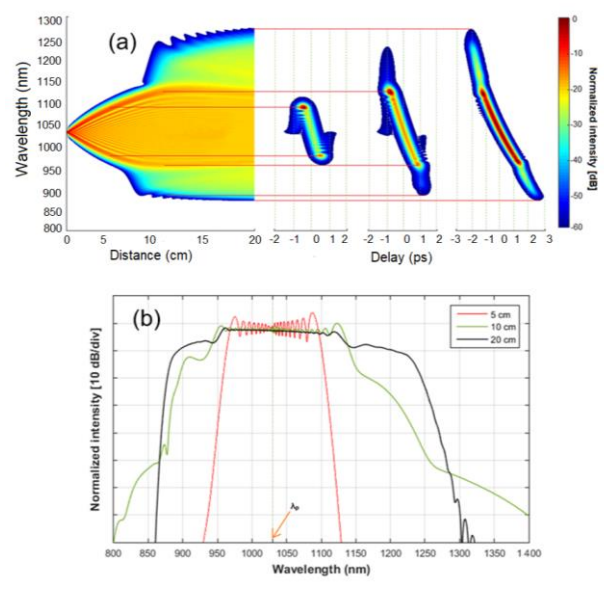

Figure 6.2. Evolution of SCG in $\#F_1$ fiber and temporal profile with various propagation length (a), the spectrum of SCG at the various length of fiber (b). The input pulse having 25 nJ, 400 fs duration of the pulse, and a central wavelength at 1030 nm. The color bar indicates normalized intensity in the logarithmic scale.

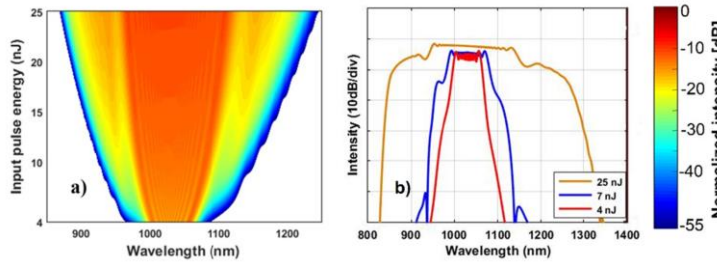

Figure 6.3. Numerical simulation of the evolution of the pulse spectrum for increasing input pulse energy in $\#F_1$ fiber: (a) SC spectral at 20 cm of propagation with various input pulse energy, (b) intensity distribution of output spectra with selected input pulse energies. The color bar indicates normalized intensity in the logarithmic scale. The input pulse with 400 fs duration of the pulse and a central wavelength at 1030 nm. The color bar indicates normalized intensity in the logarithmic scale.

When #F_1 fiber is pumped by M-pulse, the output spectrum of SCG at 15 cm of propagation length is analyzed with various input pulse energies of 0.1 ÷ 2 nJ, corresponding to 1.8 ÷37 kW of peak power. As shown in Figure 6.4, with input pulse energy below 1 nJ, the spectral broadening is induced via pure SPM, and the spectrum covers from 1300 to 1900 nm. For input pulse higher than 1 nJ, there are Raman solitons generated by MI-induced oscillations [132]. Due to the soliton self-frequency shift, the Raman solitons shift toward longer wavelengths in further propagation.

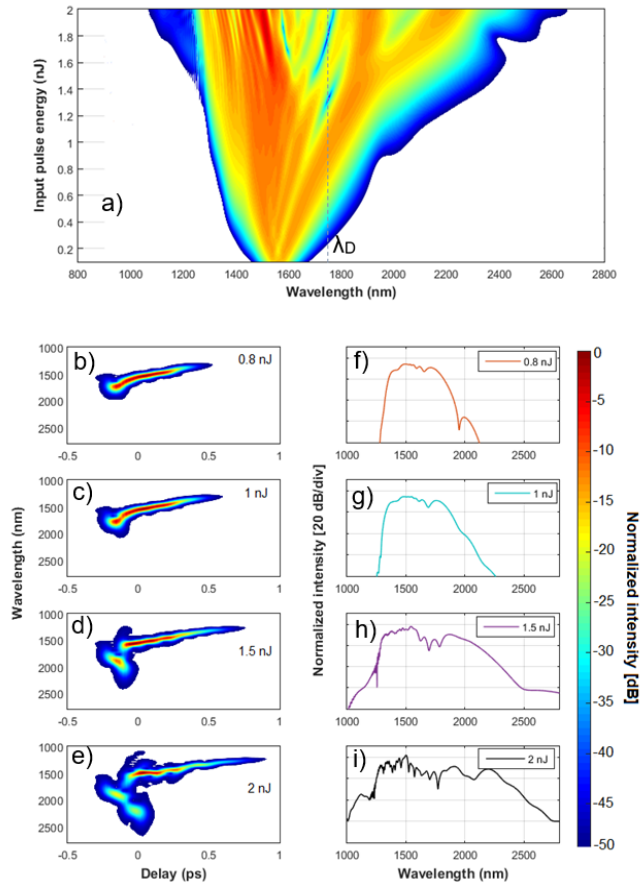

Figure 6.4. Evolution of SCG at 15 cm of propagation length of #F_1 fiber with various input pulse energies, from 0.1 to 2 nJ (a). The temporal profiles (b, c, d, e) and spectra of SCG at 15 cm of propagation (f, g, h, i) with input pulse energies: 0.8, 1, 1.5, 2 nJ. The input pules having the central wavelength of 1560 nm, 90 nJ duration of the pulse. The color bar indicates normalized intensity in the logarithmic scale.

With an input pulse energy of 0.9 nJ (peak power of 10 kW), the numerically obtained the evolution of spectral broadening along the fiber is shown in Figure 6.5. SPM is a significant contribution to spectral broadening at the beginning of propagation length, which is consistent with established knowledge on nonlinear dynamics of femtosecond laser pulses in fibers pumped in normal *D* regime [30]. When SPM components reach to ZDW of #F_1 fiber that is located at 1740 nm, the soliton dynamics begin appearing - this can be observed around 10 cm of propagation. During further propagation, the soliton shifts toward long wavelength by soliton-self frequency shift. The trailing edge belongs to the normal *D* regime, it has a complicated mechanism due to the interaction between SPM, OWB, and dispersive wave from red-shifting soliton.

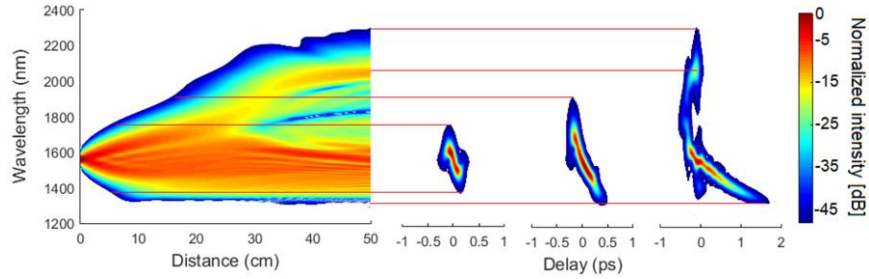

Figure 6.5. Evolution of SC along #F1 for the input pulse energy of 0.9 nJ and temporal profile at the various lengths of propagation. The color bar indicates normalized intensity in the logarithmic scale.

6.1.2 Anomalous Dispersion Supercontinuum Generation in Carbon-Tetrachloride-Core Photonic Crystal Fiber

SCG in #F_2 fiber is pumped by M-pulses. The ZDW of this fiber is around 1440 nm, thus the pump wavelength (1560 nm) belongs to the anomalous *D* regime. Figure 6.6 shows the evolution of the spectrum with increasing input pulse energy. With input pulse energy below 0.1 nJ, the broadening of the spectrum predominantly causes SPM. Further increasing input pulse energy, a significant boost to the spectral broadening by soliton fission and dispersive wave (DW). The increasing input pulse energy, followed by peak power, leads to high-number soliton. The high-order soliton with number *M* was fissioned into *M* injected fundamental solitons with different red-shifted due to soliton-self frequency shift. At the same time, the non-soliton radiation appears and blue-shifts at shorter wavelengths due to the phase matching between soliton pulses, which are generated by the soliton fission process, and linear dispersive waves [133].

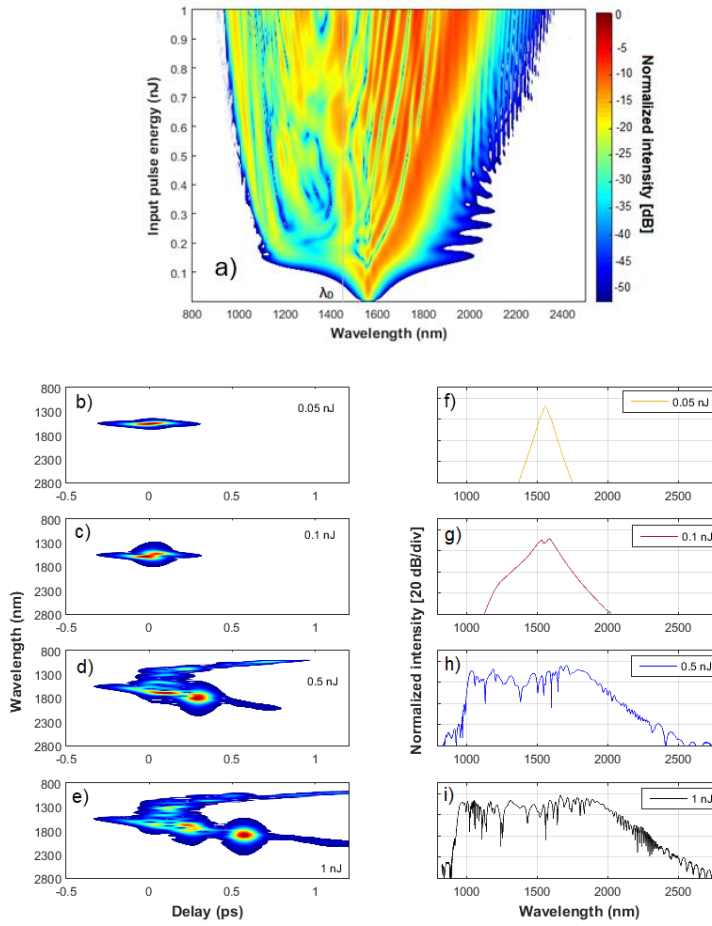

Figure 6.6. Evolution of SCG at 15 cm of propagation length of #F_2 infiltrated with CCl_4 with various input pulse energies, from 0 to 1 nJ (a). The temporal profiles **(**b, c, d, e**)** and spectra of SCG at 15cm of propagation (f, g, h, i) with input pulse energies: 0.05, 0.1, 0.5, 1 nJ. The input pules having the central wavelength of 1560 nm, 90 nJ duration of the pulse. The color bar indicates normalized intensity in the logarithmic scale.

The soliton fission and DW appear at the first centimeters of propagation length. For example, in the case of 0.5 input pulse energy (peak power 5.55kW). The nonlinear L_{NL} and dispersion length L_D are calculated as 0.98 cm and 76.24 cm, respectively. The soliton number $M = (L_D / L_{NL})^{1/2}$ approx. 9, MI characterictics length $L_{MI} = 16 \times L_{NL}$ equal to 15.7 cm. Soliton fission length $L_{fission} = L_D / M$ equal to 8 cm. As shown in Figure 6.7 (a), after 8 cm of propagation, the broadening of the spectrum is essentially concluded. It covers from 1000 to 1900 nm. Further propagation, each ejected soliton subsequently red-shifted to longer wavelength due to soliton self-

frequency shift and transform energy to short-wavelength in normal *D* range via dispersive wave. However, the use of a further length of fiber causes an increase of the effects of the noise, e.g., polarization noise [127], resulting in coherence degradation.

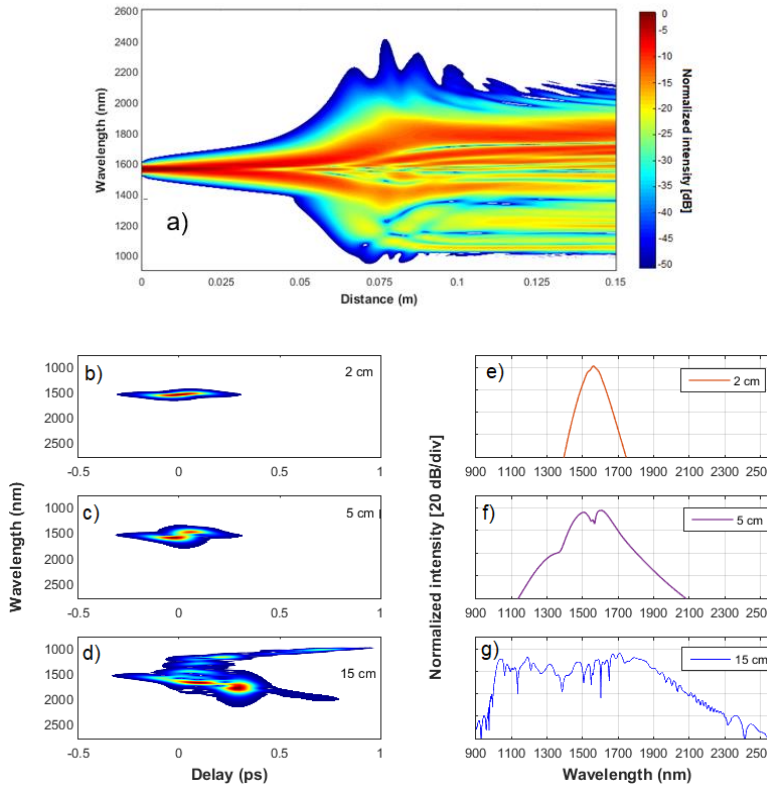

Figure 6.7. Evolution of SCG of #F_2 with 0.5 nJ input pulse energy (a). The temporal profiles **(**b, c, d**)** and spectra of SCG **(**e, f, g**)** at different propagation length: 2 cm, 5 cm, and 15 cm. The input pules having the central wavelength of 1560 nm, 90 nJ duration of the pulse. The color bar indicates normalized intensity in the logarithmic scale.

6.2 Measurement of Supercontinuum Generation in Carbon-Tetrachloride-Core Photonic Crystal Fiber

6.2.1 Normal Dispersion Supercontinuum Generation

The all-normal dispersion SCG is measured using femtosecond laser (BlueCut femtosecond fiber laser), which has a central wavelength at 1030 nm, 400 fs duration, coupling with $\#F_1$ fiber. The setup for measurement SCG in toluene core PCF as shown in Chapter 5 is also used for SCG measurement in $\#F_1$ and $\#F_2$ fibers. The ZDW of $\#F_1$ fiber is 1740 nm. The coupling efficiency between micro-objective and input end-face fiber is 54%. The output spectrum was recorded by Thorlab compact spectrometer CC-175 (range of 500÷1000 nm) and Avantes spectrometer **(**AvaSpec-NIR256-1.7) in the range of 900÷1700 nm. The length of $\#F_1$ used in this measurement is 20 cm. This length ensures optimum broadening of the spectra as it was confirmed in numerically simulated results in the previous section.

The experimental results of the SCG are shown in Figure 6.8. The output spectrum with 4 nJ input pulse energy covers in a range of 980 ÷ 1080 nm wavelength. For 25 nJ input pulse energy, the spectrum of SCG covers in range of 850 ÷ 1250 nm wavelength. An increase of either input peak power or the nonlinear coefficient by means of a reduction in core diameter is necessary to obtain further spectral broadening. However, when core of the fiber is reduced, it is challenging to get high coupling efficiency with standard single mode fiber in an all-fiber SCG system.

The experimental results show a good agreement with simulated results for both 4 nJ and 25 nJ input pulse energies. This confirms that the spectrum of SCG in this tested fiber is broadened by SPM and OWB as predicted in simulation represented in section 6.1.1. The noises appearing in the experimental spectra, which have a roughly -20 dB noise floor, relates to a measurement performance of compact spectrometer, which typically uses the Czerny–Turner monochromator. The measured spectrum has a notable structure with almost 10 dB dynamics. This structure does not significantly depend on the spectrometer integration time.

The soliton fission and MI are fundamental mechanisms to govern the level of temporal coherence of output SCG. In the normal *D* regime, soliton formation and MI are suppressed with sub-picosecond laser as a pump source. Therefore, the experimental SCG here has the potential for high coherence. However, the level of coherence also depends on the technical noises, e.g., polarization noise, amplitude noise of laser source. For laser source with 400 fs duration of the pulse, the technical noises critically decrease the coherent level of observed SCG [126,128]. In order to reduce the effects of these noises, the laser source with a short duration pulse (below 100 fs) should be used as a pump source. In the following section, the SCG measurement is implemented with MENLO Femtosecond Fiber Laser with a central wavelength of 1560 nm, 90 fs duration of the pulse.

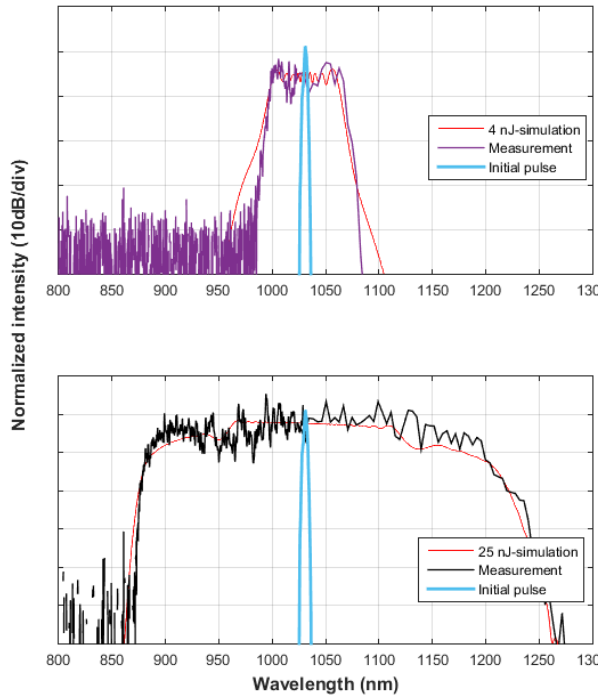

Figure 6.8. Experimental results of SCG in #F$_1$ fiber with femtosecond laser source having 1030 nm central wavelength, 400 fs duration of the pulse. Input pulse energy here is 4 nJ and 25 nJ. The simulated results of SCG are shown for reference.

In the case of using a pump laser source - a compact erbium-fiber-based femtosecond laser from Menlo Systems (model C-fiber HP), which delivers around 90 fs duration of the pulse, 1560 nm central wavelength of the pulse, a repetition rate of 100 MHz, the output spectra were recorded by OSA Yokogawa spectrometer in wavelength range of 1200÷2400 nm. As shown in section 6.1, the use of a long sample of #F_1 fiber allows to obtaining of the broad spectral bandwidth of SCG due to the soliton dynamics. However, as shown in [126], in the case of this laser source, the polarization noise can be neglect if a short fiber is used. Thus, the fiber with 15 cm is used for the SCG measurement. The highest average power pulse emits from this laser source around 340 mW, corresponding to 3.4 nJ pulse energy. In the case of #F_1 fiber, the coupling efficiency between micro-objective and the laser source is 58%. The coupling efficiency between micro-objective and fiber is 50% for the setup.

The experimental results of pump-power-dependent of output spectra are shown in Figure 6.9. The recorded spectrum with the highest laser pulse energy of 3.4 nJ covers the range from 1350 nm to 1900 nm within the 20 dB dynamics. The simulation of SCG with 0.9 nJ input pulse energy is shown for reference. Limitation of the accuracy of the digitized SEM images of the fiber sample which is used for

numerical calculation of A_{eff}, D, and attenuation leads to a difference of A_{eff} between the numerically modeled and real fiber. This also explains the misalignment of 40 nm between recorded and simulated bandwidths.

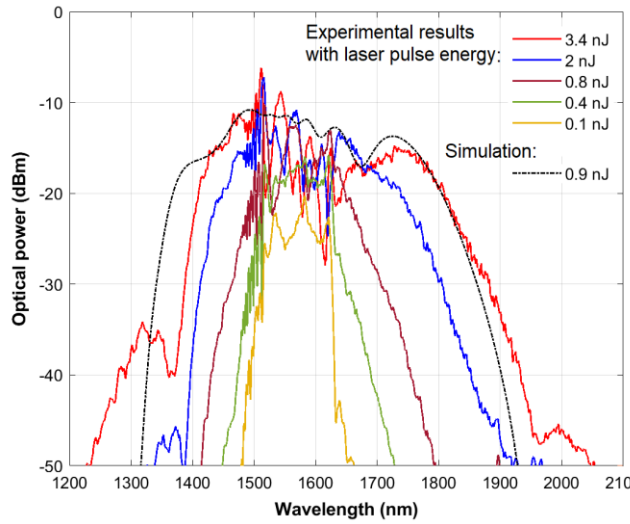

Figure 6.9. Experimental results of SCG in #F_1 fiber with femtosecond laser source having 1560 nm central wavelength, 90 fs duration of the pulse, and various pulse energies emitted from the laser source (from 0.1 to 3.4 nJ). The length of fiber is 15 cm. The simulated results of SCG with input pulse energy 0.9 nJ are shown for reference.

6.2.2 Anomalous Dispersion Supercontinuum Generation

The Menlo Femtosecond Fiber Laser (model C-fiber HP) having 1560 nm central wavelength, 90 fs duration of the pulse, and 100 MHZ repetition rate is also used for measurement SCG in #F_2 fiber. The observed spectra are shown in Figure 6.8. The spectrometer used for recording experimental data is OSA (Yokogawa) with range of 1200÷1400 nm, and, in the case spectrum exceeding this range, the Avantes spectrum with a range of 1000÷1700 is used.

The ZDW of #F_2 infiltrated with CCl_4 is 1440 nm, thus the central wavelength of the laser pulse is at the anomalous D regime. As shown in Section 6.1, the main dynamics for a spectral broadening of SCG in the fiber are soliton fission and dispersive wave. Due to the soliton dynamics, the broadening of the spectrum occurs rapidly, and thus, spectral bandwidth can conclude after the first centimeters of propagation length as predicted by numerical simulation. The experimental data, as well as the comparison with simulation results in Figure 6.8, confirm the soliton dynamics for spectral broadening in #F_2 fiber. The largest observed spectrum covers from 1000 to 1900 nm (900 nm spectral bandwidth) in roughly 30 dB dynamic. The

non-flat spectra relate to the nature of spectral broadening based on the soliton dynamics. The further spectral bandwidth could be obtained by increasing input peak power or using further propagation length. However, increasing the length of the investigated fiber, in turn, decrease the level of temporal coherence.

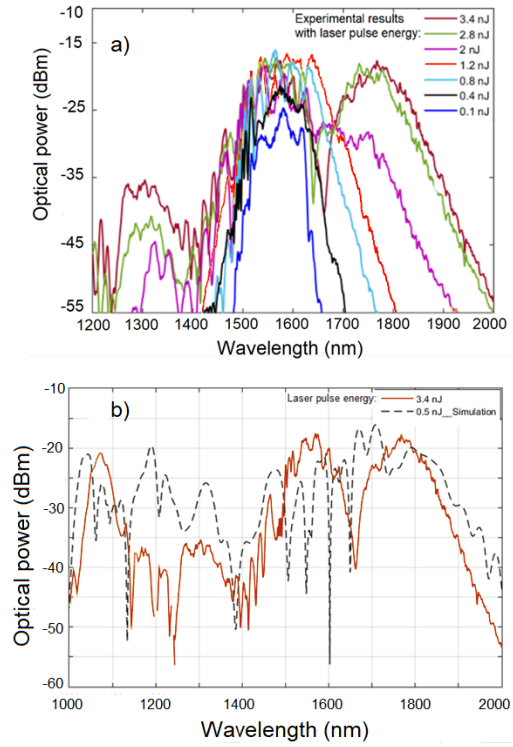

Figure 6.8. The output spectra from *#F₂* infiltrated with CCl_4 with various laser pulse energies (a), the experimental data with the highest laser pulse energy (3.4 nJ), and the numerical simulation spectrum of SCG with 0.5 nJ input pulse energy as a reference (b). The length of fiber is 15 cm. Parameters of the laser source: 1560 nm central wavelength, 90 fs duration.

The experimental results are evidence to confirm that if the nonlinear liquid core fiber is used for SCG, it is possible to achieve the broad SCG with low peak power of input pulse. In this work, the recorded SC spectrum in *#F₂* fiber corresponds to an input pulse energy of 0.5 nJ or peak power of 5.5 kW. This peak power is relatively low when compared to that of the works in [55,56] for SCG in liquid core PCFs.

6.3 Temporal Coherence

The high coherent SCG have found their way into countless applications in, e.g., frequency combs, spectroscopy, and frequency metrology [34]. The noises, that are the fundamental reason for degradation of coherence, are noise-seeded cascaded stimulated Raman scattering (called SRS noise), polarization-related noise, single-photon-per-mode noise related to spontaneous emission, laser noise originated from the fluctuation of amplitude and duration of each pulse. SRS noise is neglected in the case of the short investigated fiber pumped by femtosecond laser [134]. The effect of polarization noise, which is induced by polarization MI, can be suppressed by increasing the birefringence of the fiber, e.g. using the polarization-maintain fiber. In reference [126], the authors pointed out that the effects of polarization noise are possible to reduce if the short fiber and ultra-short lasers are used. According to that result, when $\#F_1$ fiber is pumped by BlueCut laser with 400 fs duration of the pulse, the polarization noise critically decreases the coherence of observed SCG. In contrast, the influence of polarization noise on the coherence is possible to be neglected in the case of using the Menlo Systems laser with 90 fs duration and the short length of fiber (15 cm).

The single-photon-per-mode noise is modeled semi-classically through the addition of a noise seed of one photon per mode with a random phase on each spectral discretization bin. This noise, in the frequency domain, is given in Eq (6.4):

$$\Gamma_{noise} = \sqrt{\frac{\hbar\omega}{f_{rep}}}\exp(-i\Phi), \tag{6.4}$$

where Γ_{noie} is amplitude of the noise, $\hbar$ is reduced Planck's constant, f_{ree} is pumped repetition rate, Φ is a random phase sample uniformly over interval $[0,2\pi]$.

Laser noise, i.e., amplitude noise, is described by δ_{AN} that has unit mean and a standard deviation equal to rms (root-mean-square) of amplitude noise of the laser. The amplitude noise of Menlo system laser (C-fiber HP) around 0.5% rms (over 24 h) [129] and the amplitude noise of BlueCut Femtosecond Fiber Laser is 1% rms (over 12h) [127]. The effects of amplitude noise lead to fluctuation of the pulse duration with standard deviation δT_0 [128]:

$$\delta T_0 = -0.8*(\delta_{AN} - 1). \tag{6.5}$$

The initial input pulse with laser noise and pulse shot noise is formed according to:

$$A(0,t) = \sqrt{P_0}\delta_{AN}\exp\left(\frac{T^2}{2T_0^2(1-\delta T_0)^2}\right) + F^{-1}(\Gamma_{noise}) \tag{6.6}$$

The temporal coherence of SCG is determined by using the first-order coherence:

$$\left|g_{12}^{(1)}\left(\lambda,t_1-t_2=0\right)\right|=\left|\frac{\left\langle E_1^{*}\left(\lambda,t_1\right)E_2\left(\lambda,t_2\right)\right\rangle}{\left[\left\langle\left|E_1\left(\lambda,t_1\right)\right|^2\right\rangle\left\langle\left|E_2\left(\lambda,t_2\right)\right|^2\right\rangle\right]^{1/2}}\right|. \tag{6.7}$$

where the angle bracket denotes an ensemble average over independently generated pairs of SC spectra [E_1, E_2] with one photon per mode noise seeds.

Figure 6.9 shows the first-order coherence of the SCG in #F_1 when pumped by BlueCut Femtosecond Fiber Laser, which has a pulse duration of 400 fs and intensity noise of 1% rms. Albeit observed SCG in all-normal *D*, the effects of laser noise significantly reduce the coherent level of the spectrum.

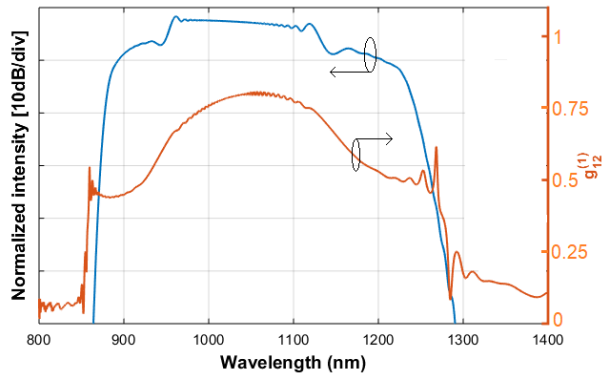

Figure 6.9. Numerical calculation the first-order of coherence $g_{12}^{(1)}$ of the SCG in #F_1 fiber with 20 individual pairs of spectra generated with the random noise seed for 25 nJ input pulse energy. The laser source is the BlueCut Femtosecond Fiber Laser having a central wavelength at 1030 nm, 400 fs duration of the pulse, amplitude noise of 1% rms. The length of the fibers is 20 cm. The simulation of SC spectrum for reference.

Figure 6.10 shows the first-order coherence of the SCG in #F_1 and #F_2 fibers with the Menlo system laser as a pump laser source. As the above analysis, the SCG in #F_1 is generated by SPM and OWB mechanisms. Therefore, SCG in #F_1 fiber shows the high potential for coherence (Figure 6.10 (a)). In the case of #F_2, the pump wavelength is in the anomalous *D* regime. The soliton fission and DW are the significant contributions to spectral broadening. At the same time, the effects of input noises amplified by MI is the primary cause of coherence degradation. In order to estimate the level of the degradation of the coherence of anomalous dispersion SCG, the straightforward way is to consider the relative distance scales associated with MI

and soliton fission. With an input peak power of 5.5 kW, the soliton fission length L_{fiss} = 8 cm, the MI characteristic length L_{MI} = 15.7 cm. According to these calculations, soliton fission occurs not long before the onset of MI-related noise which corresponds to the coverage of the MI gain bands with seed signal, which has not experienced significant decoherence due to soliton dynamics. Consequently, the anomalous dispersion SCG in $\#F_2$ fiber with low input peak power (5.5 kW) has high degree of coherence [86], (Figure 6.10 (b)). With the further increase of input peak power, the L_{MI} will be decreased, resulting in the gradual degradation of coherence.

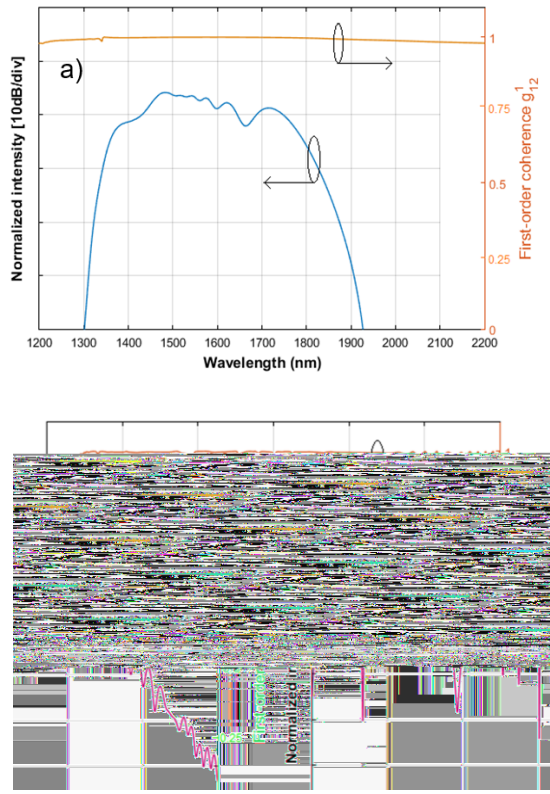

Figure 6.10. Numerical simulation the first-order of coherence $g_{12}^{(1)}$ of the SCG with 20 individual pairs of spectra generated with the random noise seed in $\#F_1$ fiber with 0.9 nJ input pulse energy (a) and in $\#F_2$ fiber with 0.5 nJ input pulse energy (b). The laser source is the Menlo system laser having a central wavelength of 1560 nm, 90 fs duration of the pulse, amplitude noise of 0.5% rms. The length of the fibers is 15 cm. The simulation of spectra here is as the references.

6.4 Conclusion

This chapter provided the experimental data of SCG in photonic crystal fibers infiltrated with CCl_4 pumped by femtosecond laser. Simulation SCG in investigated fibers by solving GNLSE has been shown as the reference to compare with the experimental data. The large core PCF infiltrated with CCl_4 ($\#F_1$ fiber) was used for SCG measurement with the laser sources having central wavelength 1030 nm and 400 fs duration of the pulse. $\#F_1$ fiber has ZDW at 1740 nm, and all-normal dispersion SC

these fibers is near 0.5 [27]. The D of tested fiber is slightly different from these commercial fibers.

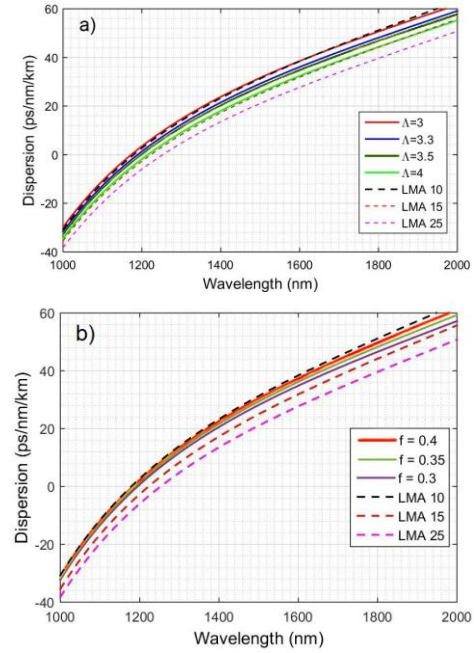

Figure 7.2. The D with f = 0.34 and various value of Λ (a), and Λ = 3.3 µm and various value of f (b). The D of commercial LMA 10, LMA 15, LMA 25 [27] is shown for reference.

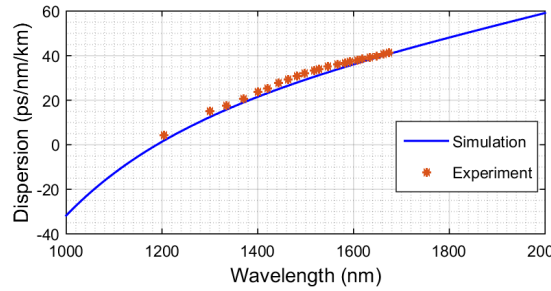

Figure 7.3. Simulation and experimental D of proposed LMA PCF.

The D of proposed PCF is verified by Mach-Zehnder interferometer setup as shown in Chapter 4. The experimental results stay in a good agreement with simulated results. Based on both simulation and experimental results, it is possible to conclude that the investigated LMA PCF has ZDW at 1190 nm, blue-shifted by 60 nm when compared with ZDW of LMA 15. D of the investigated PCF change from – 30

ps/nm/km to 60 ps/nm/km in a wavelength range of 1000 ÷ 2000 nm, and it is around 30 ps/nm/km at 1560 nm.

7.2.2 Low Bending Loss

The loss characteristics of investigated LMA PCF as well as its bending loss are calculated by FDE method, using boundary condition as the energy contained in the dislocated part of guided-mode absorbed at the PML. As shown in [143,144], the LMA PCF is relatively sensitive to bending, this leads to the limitation of using the LMA PCF in a compact system. In the case of proposed LMA PCF, based on the simulated results, the waveguide loss of fundamental mode is below 0.05 dB/km in the range of investigated wavelength range of 1000 nm ÷ 2000 nm (Figure 7.4(a)). The high-order mode has a critical increase of waveguide loss with the wavelength longer 1400 nm, and it is around 25 dB/km at a wavelength of 2000 nm.

The high-order mode is relatively sensitive to bending, as shown in Figure 7.4(b). When the bending radius $R < 2$ cm, it critically increasing with the reduction of bending radius, and it is around 15 dB/km with $R = 5$ cm. The numerical results also show, that in the feasible range of bending radiuses of uncoated fiber ($R \geq 2.5$ cm), the investigated PCF is insensitive to bending. The bending loss of commercial available LMA 10 is calculated with $R < 2$ cm, Figure 7.5. The results show that bending loss of proposed fiber is significantly reduced with $R < 1$ cm when compared to that of LMA 10.

The loss of investigated fiber measured at a wavelength of 1064 nm is 0.18 dB/m. This value is higher than expected for fiber made from silica because technical-grade silica with a high concentration of OH- has bee used for fiber fabrication.

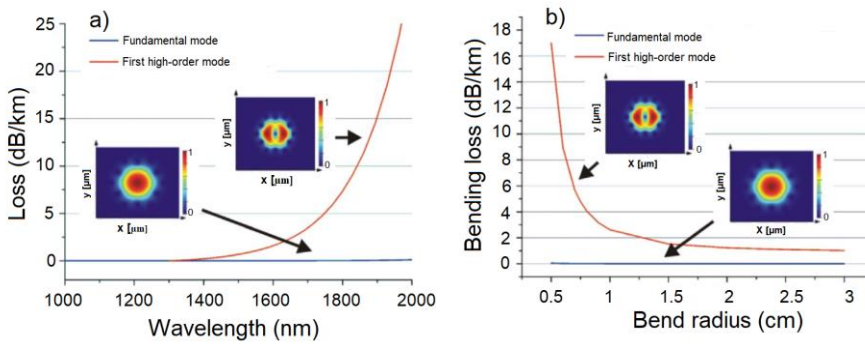

Figure 7.4. Numerically calculated waveguide losses of the fundamental mode and first higher-order mode in the silica PCF in the function of wavelength (a), bend radius R (b) and for wavelength 1500 nm and the fiber was bent in the XZ plane. Insets show mode field distribution of the fundamental and first higher-order mode, scaled in the normalized electric field.

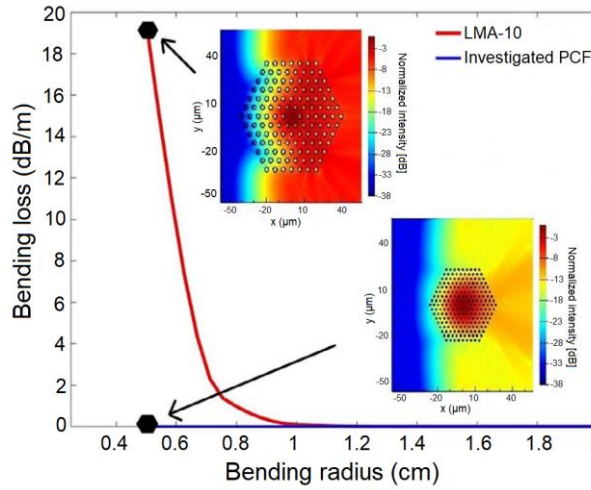

Figure 7.5. Waveguide losses of the fundamental mode for commercially available LMA-10 fiber (reconstructed from geometrical data [27]) and our proposed PCF calculated for the wavelength λ = 1064 nm. The insets present the field intensity distribution in the logarithmic scale corresponding to a waveguide with a bend radius of 0.5 cm.

7.2.3 Single Mode Operation

The setup to investigate the propagation properties, like beam profile and mode structure of the LMA fiber is shown in Figure 7.6. The laser source is the quasi-continuous-wave single mode high-power laser operating a wavelength at 1017 nm, duration of 3 ms, period of 50 ms and a maximum power of 9.1 W. The beam from the laser source is coupled into the investigated fiber core by microscope objectives (L_1) and (L_2) of focal lengths of 50 mm and 35 mm, respectively. The IR CCD camera is used for far-field image capture. The investigated fiber is 731 cm long, and it is bent with a radius of 7.76 cm.

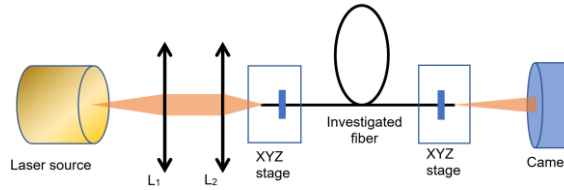

Figure 7.6. The setup used for testing the propagation properties of the investigated PCF.

The far-field of the mode profile of the output beam is imaged by CCD camera, and then its distribution of intensity of central cross-section is fitted with a Gaussian curve, as shown in Figure 7.7. The agreement between the Gaussian curve and the distribution of intensity confirmed that the investigated fiber can support the single

mode regime at the wavelength of 1017 nm. The results obtained at 1017 nm correspond with those, which could be achieved for longer wavelengths, and they would not differ significantly.

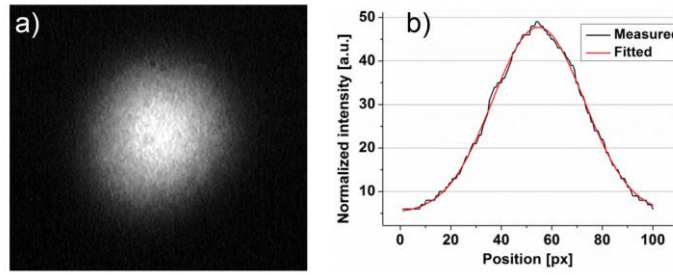

Figure 7.7. Far-field image of the effectively single mode beam at the output of the silica PCF (a), a central cross-section of the beam intensity profile along with Gaussian curve fit (b).

Proposed LMA PCF has four higher-order modes at 1017 nm wavelength and the cut-off wavelength λ_c = 4400 nm. The effective refractive indices (n_{eff}) of the fundamental mode and the first higher-order mode are shown in Figure 7.8. In the NIR range, the difference of n_{eff} between the fundamental mode and high-order mode is relatively large. In particular, Δn_{eff} = 0.002 at a wavelength of 1017 nm. Due to the significant difference of n_{eff} of these modes, the fundamental mode is separated from higher-order mode, and thus, it could be selectively excited.

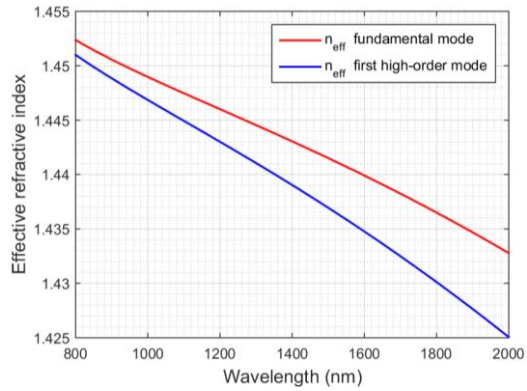

Figure 7.8. n_{eff} of the fundamental mode and first high-order mode in the investigated LMA PCF.

7.3 Low Nonlinearity of Large Mode Area Photonic Crystal Fiber

The A_{eff} of proposed LMA PCF is calculated by numerical method. As shown in Figure 7.9, its values are from 54.5 μm^2 to 60.5 μm^2 in the wavelength range of 1000 nm to 2000 nm. The nonlinear coefficient (γ) of the fiber is from 1.5 ($W^{-1}km^{-1}$) to 3 ($W^{-1}km^{-1}$) in the investigated wavelength range. For 1560 nm wavelength, investigated fiber has A_{eff} = 57.5 μm^2 and γ = 2 $W^{-1}km^{-1}$. The nonlinear coefficient of proposed LMA fiber is very small when compared to that of the soft glass-fiber and SCG fiber.

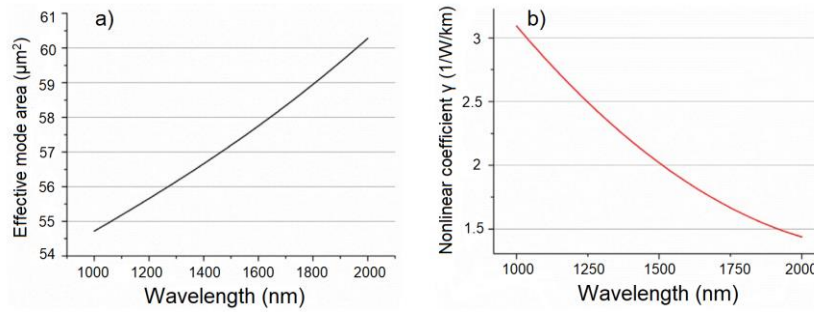

Figure 7.9. The A_{eff} (a) and nonlinear coefficient of investigated LMA PCF.

The spectral and temporal distortion of pulse shape in the investigated fiber is analyzed by solving GNLSE, as shown in Chapter 2. The initial pulse is in a Gaussian shape with parameters: central wavelength at 1560 nm, pulse duration of 90 fs, pulse energy of 0.1 nJ ÷ 1.8 nJ – corresponding to the peak power of 1kW ÷ 20 kW. The length of fiber is 1 m. One-photon-per-mode noise is also included in all simulations. The results show that:

(i) peak power at 1 kW, the pulse is undistorted (Figure 7.10(a) and 7.11);

(ii) peak power at 5.55 kW, the nonlinear self-focusing occurs spectrally (Figure 7.10(b)), and temporal profile is undistorted (Figure 7.12(a) and 7.12(d));

(iii) peak power at 13.3 kW, the pulse is undistorted spectrally and temporally, however, the temporal profile has delay time around 1 ps (Figure 7.12 (b,e));

(iv) peak power at 20 kW, the soliton fission generates the wavelengths around 1540 nm and 1660 nm – Figure 7.10, 7.11. The temporal profile has two parts with the delay times around 2.5 ps and -0.5 ps (Figure 7.12 (c,f)).

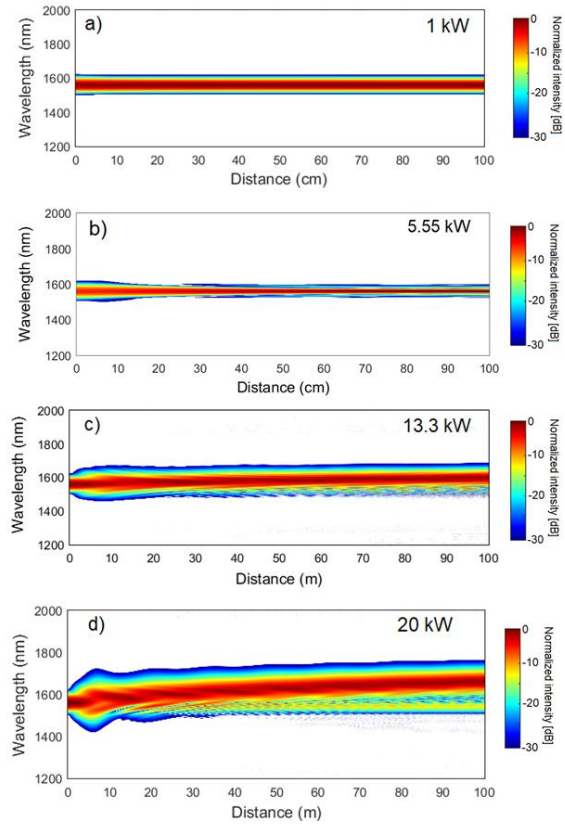

Figure 7.10. Calculated nonlinear spectral broadening of the pulse in the 1 m LMA PCF sample. Pulse peak power 1 kW (a), 5.55 kW (b), 13.3 kW (c), and 20 kW (d). Color maps are scaled in normalized intensity.

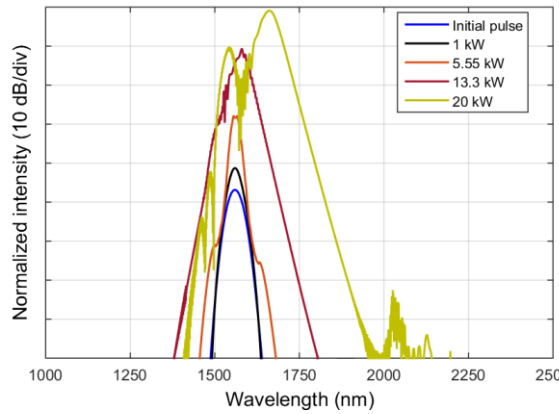

Figure 7.11. The spectral broadening of the pulse in the 1m of propagation with various peak power.

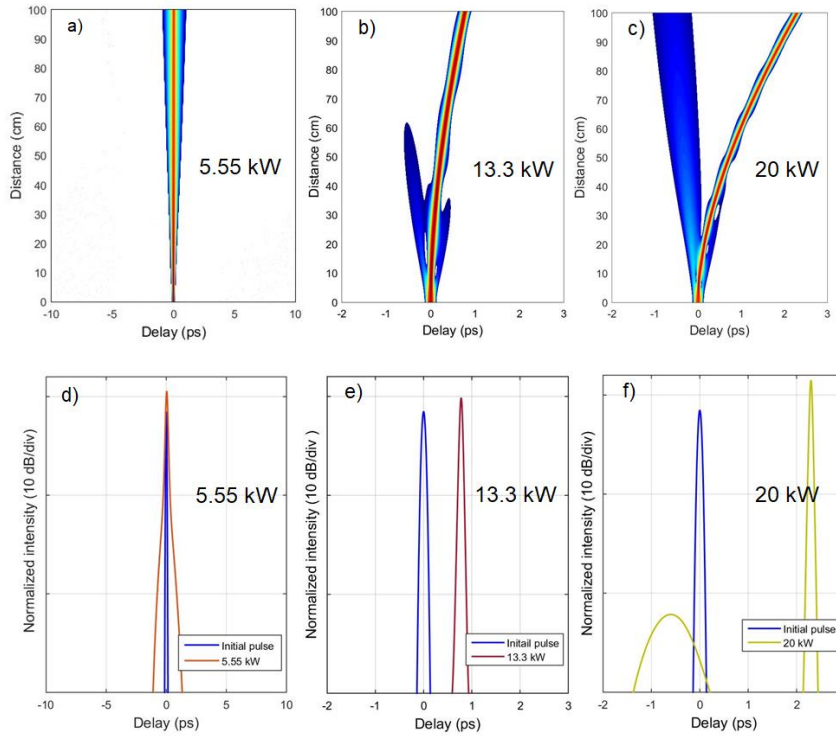

Figure 7.12. The evolution of temporal profile in investigated LMA PCF with various peak power (a, b,c), and the temporal profile of the pulse in 1m of propagation with various peak power (d,e,f).

The proposed LMA fiber can resist up to peak power of 16 kW without temporal and spectral distortion. The further increase of peak power leads to spectral broadening induced by soliton fission and DW. The undistorted pulses, which can be delivered by this fiber, have lower peak power as required for SCG in typical silica-based on nonlinear PCF. Typically, SCG silica PCF requires the input pulse with peak power higher than 20 kW. But, due to the high nonlinear of selected liquid, the liquid core fiber typically requires the low peak power for broad SCG. For example, near one octave SCG was observed in #F_2 fiber with peak power around 5.5 kW.

The proposed LMA fiber is dedicated to coupling with liquid core PCF in an all-fiber SCG system, as the following configuration in Figure 7.13, including two LMA PCF with minimum length at 20 cm fusion-spliced with liquid core PCF.

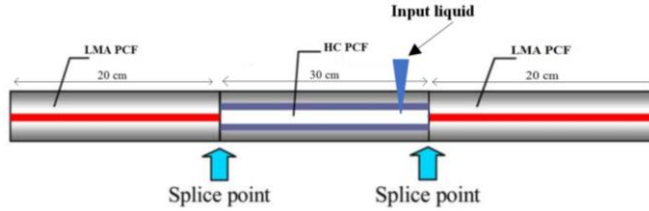

Figure 7.13. Schematic representation of fusion splice coupling between LMA PCF and liquid core PCF.

The coupling efficiency of liquid core PCF and LMA fiber depends on their A_{eff} and other technical parameters, e.g., direction of propagation, transverse and angular alignment of the modes in the fibers. The coupling efficiency (η) of two fibers is given in Eq (7.2) [145], where w_1 and w_2 are mode radii, Δd is transverse offset:

$$\eta = \frac{4w_1^2 w_2^2}{\left(w_1^2 + w_2^2\right)^2} \exp\left(-\frac{2\left(\Delta d\right)^2}{\left(w_1^2 + w_2^2\right)}\right) \tag{7.2}$$

Table 7.2. shows the numerical calculation of coupling efficiency between the LMA fibers and CCl_4 core PCFs. The LMA-25 has the large A_{eff} (around 311.5 μm^2 at 1560 nm), but it offers the low coupling efficiency with the CCl_4-core PCF. Coupling efficiency between investigated LMA PCF and the liquid core PCF is relatively high, around 91% and 79% with $\#F_1$ and $\#F_2$ fiber, respectively.

Table. 7.2. Coupling efficiency between LMA fiber and the CCl_4-core PCF at 1560 nm.

Liquid core PCF	LMA 10	LMA 15	LMA 25	This work
$\#F_1$ fiber	87%	68%	32%	91%
$\#F_2$ fiber	73%	49%	21%	79%

7.4 Conclusion

The low D, low nonlinearity, LMA PCF was developed to dedicate for short pulse delivery and coupling with liquid core PCF for an all-fiber SCG system. Proposed LMA PCF can deliver the ultra-short pulse (90 fs) with peak power up to 16 kW at 1560 nm without temporal and spectral distortion. The D of this fiber varies from -30 ps/nm/km to 60 ps/nm/km in the wavelength range of 1000 nm ÷2000 nm and the ZDW is located around 1190 nm wavelength. The A_{eff} is 57.5 μm^2 at 1560 nm. This fiber is also effectively single mode for 1017 nm wavelength. Although this fiber has A_{eff} and D are similar to that of commercial LMA-10 and LMA-15, it can

significantly reduce bending losses for the low radius of curvature. Low bending losses with a small radius are very important for packaging issues in practical applications.

This result shows that proposed LMA PCF cannot replace hollow core fibers used for pulse energy required for SCG in typical silica nonlinear PCFs. However, this fiber can be used for pulse delivery in all-fiber systems with liquid core fibers where requires much lower peak power of input pulse. For example, due to the high nonlinearity of liquids, an octave-spanning SC spectrum was observed in $\#F_2$ fiber with input peak power of 5.5 kW, as shown in Chapter 6. Proposed LMA PCF also can offer high coupling efficiency with $\#F_1$ and $\#F_2$ fiber, which are up to 91% and 79%, respectively. The high coupling efficiency between proposed LMA PCF with liquid core PCF confirms the feasibility of **Thesis 1** and **Thesis 2** in SCG applications, as a promising approach for compact, low-cost all-fiber SCG system.

8 Antiresonant Fibers Infiltrated with Liquids

This chapter is devoted to studying the optical properties of AR fibers infiltrated with water and ethanol. It includes the experimental setup to observe the spectral position of transmission windows of AR fibers with different thicknesses of capillaries and the numerical simulation to estimate the attenuation of the liquid core AR fibers. The results in this chapter are my original contributions and have been submitted in a JCR journal [A9].

The liquids, e.g, water, ethanol, buffers, and CCM have refractive indices ($n(\lambda)$) smaller than those of silica, thus hollow core fiber infiltrated with these liquids would guide the light by either band-gap mechanism or AR mechanism. However, the hollow core PBG fiber infiltrated with low-index liquid has an intrinsic narrow transmission window [65], and unsuitable for broadband spectral measurement. Moreover, the small scale of the core of hollow core PBG fiber (at the micrometer level) makes the liquid filling process time-consuming and impossible to control the flow-rate of liquid inside the fiber. On the other hand, AR fiber with further broad transmission windows has been utilized for several optofluidic applications [70÷75].

8.1 Experimental Setup

The AR fibers are fabricated in-house by the stack-and-draw method [116], they have seven capillaries which are detached from each other (Figure 8.1). The parameters of the fibers are shown in Table 8.1.

Table 8.1. geometrical parameters of AR fibers.

Fiber	**Thickness t (μm)**	**Capillary diameter d (μm)**	**Outer diameter d_t (μm)**	**Core diameter d_{core} (μm)**
AR_1 fiber	7.25	22.85	232	91.88
AR_2 fiber	2.272	12.53	148.8	68.79
AR_3 fiber	1.828	21	160.9	64.89
AR_4 fiber	1.802	25.86	161	64.92

AR_4 fiber has a different structure from those of other fibers, it has 7-non-touching double-nested capillaries with the outer and inner capillary diameter are 25.86 μm and 14.8 μm, and their thicknesses of capillaries are 1.802 μm and 0.925 μm. The thickness of outer capillaries in AR_4 fiber is close to the thickness of AR_3 fiber, thus these AR fibers may have transmission windows with the similarity of spectral position. However, it is noted that, as shown in [137], AR fibers typically are very sensitive to bending and are considered as one of their biggest disadvantages.

The use of AR fibers with double-ring capillaries, such as AR_4 fiber, has been shown to alleviate the challenge of reducing bending loss [146, 147].

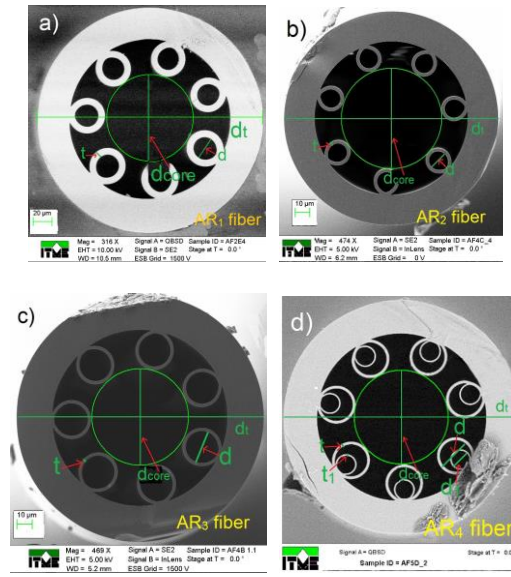

Figure 8.1. SEM imagine of AR_1 fiber (a), AR_2 fiber (b), AR_3 fiber (c), AR_4 fiber (d).

The non-transmission wavelengths (λ_m) of unfilled and liquid core AR fibers could be estimated using Eq (2.4) in Chapter 2:

$$\lambda_m \approx \frac{2t}{m}\sqrt{n_s^2 - n_i^2}, \tag{2.4}$$

where n_s and n_i are $n(\lambda)$ of silica and the liquid, respectively, m is an integer.

The spectral position of non-transmission wavelengths, and thus transmission window, depends on the thickness t and $n(\lambda)$ of the selected liquid.

$n(\lambda)$ and attenuation of water and ethanol are shown in Figure 8.2. These liquids are quite transparent in the visible range with attenuation smaller than 1 dB/m. However, their attenuation increases critically in the NIR range. The attenuation spectrum of water shows peaks at 980 nm, 1200 nm, and 1450 nm which results from the overtone stretch vibration of -OH group. The peak of the attenuation of ethanol is at 910 nm, 1190 nm, and 1580 nm.

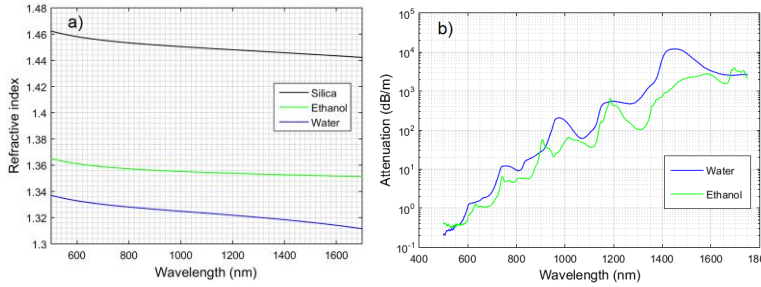

Figure 8.2. Refractive index (a) and attenuation (b) of water and ethanol [46].

The system to observe transmission window of the fibers is shown in Figure 8.3. The SC source with a wavelength range of 450÷2400 nm is used as an emitting light source. $MO_{1,2}$ are 4X and 20X lenses, respectively. In the case of AR fibers infiltrated with liquids, two the ends of the fibers are inserted into liquid reservoirs with a thin transparent glass window for light coupling, one of the reservoirs is connected with a liquid pump system to maintain liquid inside the fiber and avoid the lack of liquid at the ends of the fiber during measurement. The output beam is collimated by MO_2 lens and then launched into the multimode fiber, which is connected with the spectrometers. AvaSpec-NIR256-1.7 by Avantes with the wavelength range 1÷1.7 μm and Thorlbab CCS 175 (500 nm ÷1100 nm) are used to record output spectra.

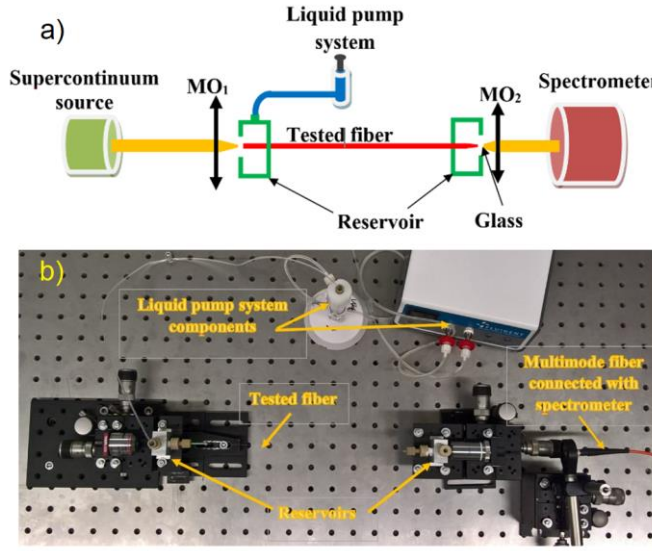

Figure 8.3. Schematic representation of setup used to observe transmission window of AR fiber (a) and experimental setup (b).

8.2 Experiment Results

The transmission windows of unfilled and liquid-filled AR_1 fibers are shown in Figure 8.4. The investigated wavelength range is from 500 nm to 1700 nm for AR_1 fiber, while liquid core AR_1 fibers are observed in a range of 500 ÷ 1100 nm because of the high attenuation of ethanol and water in the NIR range. AR_1 fiber has a relatively large thickness of capillaries (t=7.25 μm), thus the spectral bandwidths of its transmission windows are relatively narrow when compared to those of other investigated AR fibers. For instance, the largest one around 1600 nm spans from 1520 nm to 1660 nm. When AR_1 fiber infiltrates with water and ethanol, the transmission window shift toward a shorter wavelength. The blue-shifting of AR filled with liquids can be estimated using Eq (2.4). Compared to the spectral position of unfilled AR_1 fiber, the transmission windows of water-core and ethanol-core AR_1 fiber blue-shift around 655 nm and 760 nm, respectively.

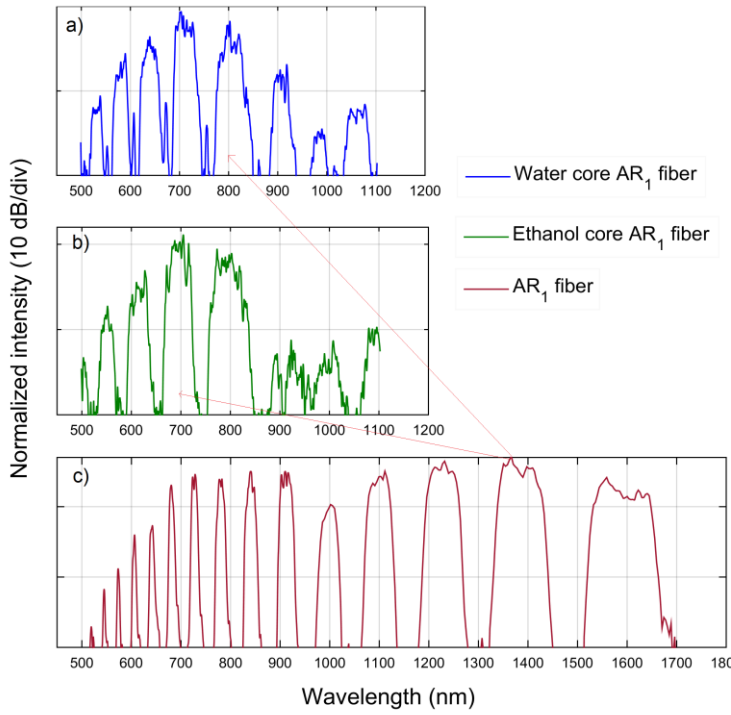

Figure 8.4. Transmission windows AR_1 fiber infiltrated with water (a), ethanol (b), and unfilled AR_1 fiber (c). The length of fiber is 20 cm.

AR_2 fiber has a thickness of capillaries (t = 2.272 μm) smaller than that of AR_1 fiber, thus its transmission window is broader than AR_1 fiber (Figure 8.5). Based on the Eq (2.4) and $n(\lambda)$ of silica as shown in Figure 8.2, the λ_m of unfilled AR_2 fiber can be predicted to be at 1580 nm, 1200 nm, 960 nm, 800 nm, 692 nm, 605 nm, and 540 nm with $m = 3 \div 9$, respectively. For water-core AR_2 fiber, λ_m is at 900 nm, 674 nm, and 545 nm with m = 3,4, and 5, respectively. Ethanol-core AR_2 fiber has λ_m at 792 nm and 600 nm for m = 3 and 4, respectively. These values of λ_m match very well with experimental data of transmission windows as shown in Figure 8.5. When this fiber is filled with water and ethanol, the transmission windows experience blue-shift by 680 and 785 nm, respectively.

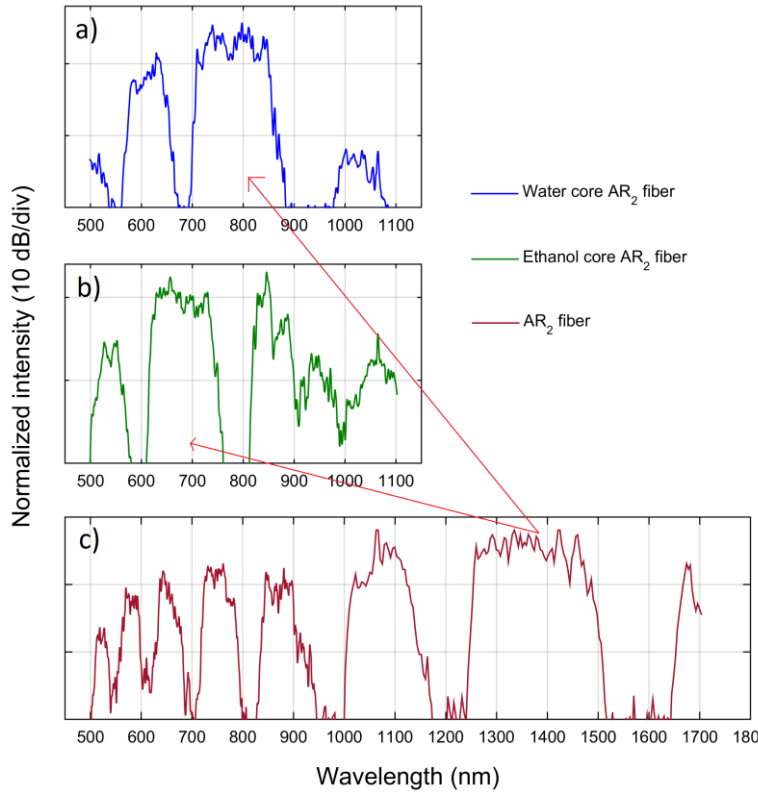

Figure 8.5. Transmission windows AR_2 fiber infiltrated with water (a), ethanol (b) and unfilled AR_2 fiber (c). The length of fiber is 20 cm.

The further decrease of thickness of capillaries leads to reduce the number of λ_m in the investigated wavelength range. For example, in a range of 500 nm ÷1700 nm, AR_2 fiber has 8 values of λ_m, which is calculated by Eq (2.4) and shown in Figure 8.5, while AR_3 fiber (t = 1.828 μm) has only 6 values of λ_m. Thus, the transmission windows of AR_3 fiber are slightly broader than that of AR_2 fiber in the investigated

wavelength range. λ_m of AR_3 fiber is at 1280 nm, 966 nm, 780 nm, 660 nm, and 560 nm for m = 3÷7, respectively. Water-core AR_3 fiber has λ_m at 1085nm, 720nm, and 540nm for m = 2,3,4, respectively, while ethanol-core AR_3 fiber has λ_m at 980nm and 630 nm for m = 2 and 3, respectively. The amount of blue-shifting when AR_3 fiber is filled with water and ethanol is 560 nm and 680 nm, respectively.

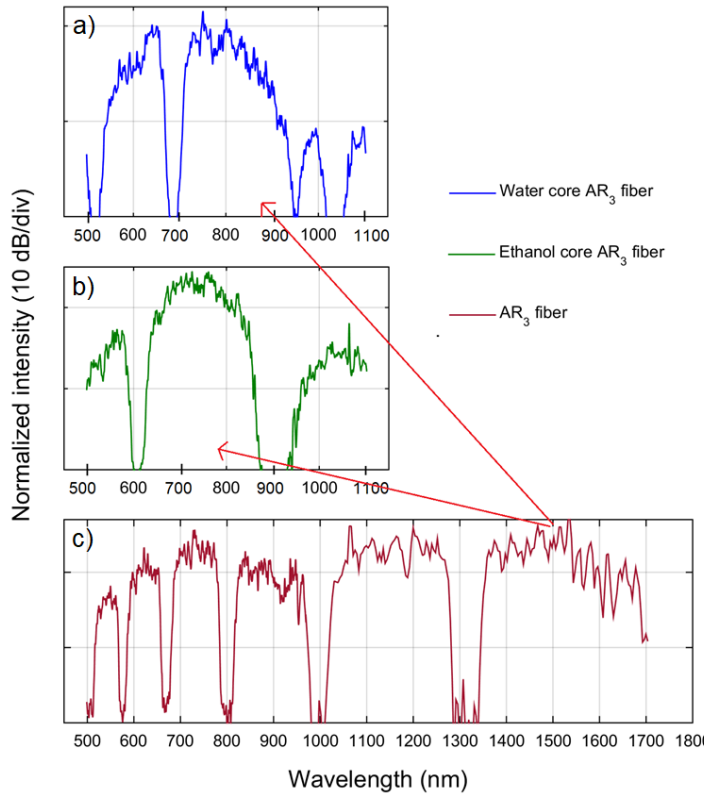

Figure 8.6. Transmission windows AR_3 fiber infiltrated with water (a), ethanol (b), and unfilled AR_3 fiber (c). The length of fiber is 20 cm.

AR_4 fiber has the thickness of capillaries t = 1.802 μm, it is slightly different from that of AR_3 fiber. Thus, as shown in Figure 8.7, the spectral position of transmission windows of AR_4 fiber is similar to AR_3 fiber. The λ_m of unfilled AR_4 fiber is 1250 nm, 942 nm, 635 nm, and 551 nm for m = 3 ÷ 7, respectively. For water-core AR_4 fiber, it is 1056 nm, 705 nm, and 530 nm for m = 2,3, and 4, respectively. In the case of ethanol-core AR_4 fiber, λ_m is at 924 nm and 623 nm for m = 2 and 3, respectively The amount of blue-shifting when AR_3 fiber filled with water and ethanol is 545 nm and 625 nm, respectively.

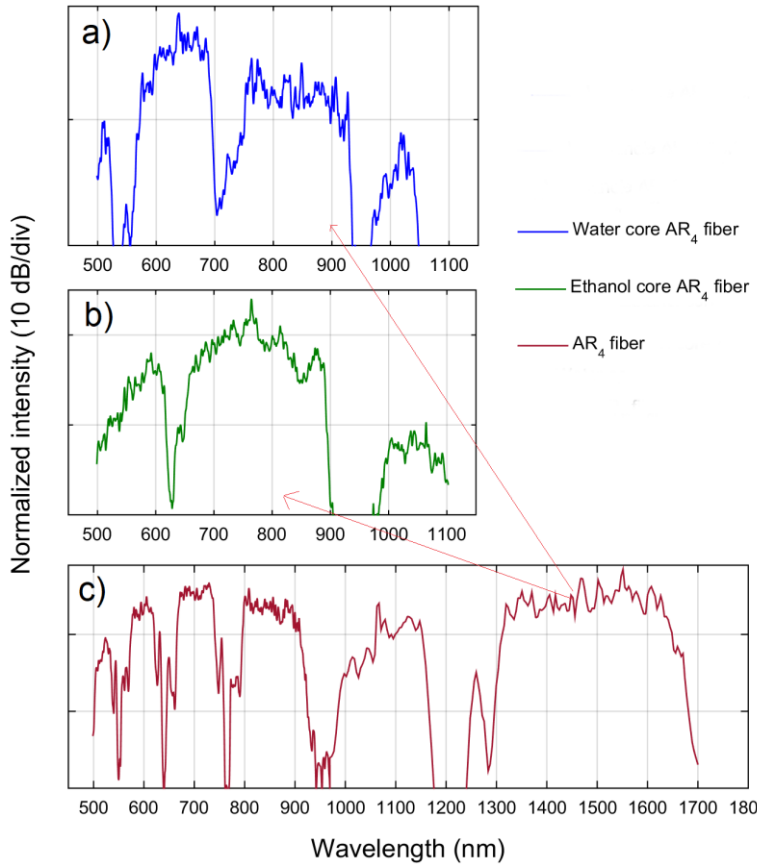

Figure 8.7. Transmission windows AR_4 fiber infiltrated with water (a), ethanol (b), and unfilled AR_4 fiber (c). The length of fiber is 20 cm.

8.3 Numerical Simulation Loss of Antiresonant Fiber Infiltrated with Liquid

Measuring the losses of liquid core AR fiber shows some difficulties, which relate to the material absorption of the selected liquids and instability of the output beam. The use of the optofluidic pump system to make the flow of liquid in the tested fiber leads to the output spectrum is not stable in the long-term. Thus, a simulation tool is implemented to estimate the losses of tested fibers. Numerical simulations are performed in COMSOL Multiphysics software (finite-element method, FEM). Replacing the air by water and ethanol was assumed in the whole hollow area of the fiber.

The losses of AR fiber infiltrated with liquids include confinement loss (CL), material loss (ML), and surface scattering loss (SSL). In which, CL originates from the mechanism guidance of the fiber. Also, CL depends on the range of investigated wavelength. The material loss here originates from the attenuation feature of water and ethanol, which have high attenuation in NIR range.

Another source of losses, significant in the short-wavelength range is surface scattering loss (SSL). It was calculated according to Eq (8.1) [148]:

$$\alpha_{SSL} = \frac{\mu F}{\lambda^3}, \tag{8.1}$$

where F is power fraction in silica glass and μ is a proportionality coefficient. The value of μ was taken equal to 300 at 1550 nm wavelength, according to [148]. F was calculated as a ratio between power transmitted in the glass and total transmitted power, calculated as z component of the Poynting vector.

In the investigated wavelength range, transmission windows of AR_1 fiber are quite narrow, this leads to the limitation of its application in optofluidics. With the small wall thickness t, AR_3 and AR_4 fibers support the broad transmission windows. Thus, the attenuation analysis herein focuses on this characteristic of AR_3 and AR_4 infiltrated with water and ethanol.

The losses of AR_3 fiber infiltrated with water and ethanol are presented in Figure 8.8. The results show that CL and SSL are relatively small when compared to the total loss in each transmission range. The loss bands have the same spectral position as transmission windows. It is clear to conclude that the total loss of investigated fibers follows that shape of material loss of water and ethanol. And CL could be neglected since the material loss of the liquids is on the order of dB/m.

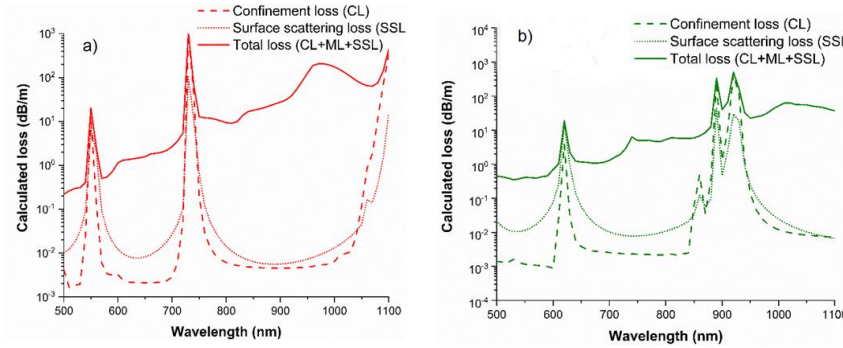

Figure 8.8. CL, SSL, and total loss of water-core AR_3 fiber (a), and ethanol-core AR_3 fiber (b).

The losses of AR_4 fiber infiltrated with water and ethanol are similar to those of water and ethanol-core AR_3 fiber. In the NIR range, the high absorption of these liquids leads to the liquid core fibers have a high total loss (Figure 8.9). In the range

of 750 nm ÷ 950 nm, the loss of water-core AR_4 fiber is from 10 dB/m to 100 dB/m, while ethanol-core AR_4 fiber has the total loss from 1 dB/m to 20 dB/m in the range of 650 nm÷900 nm.

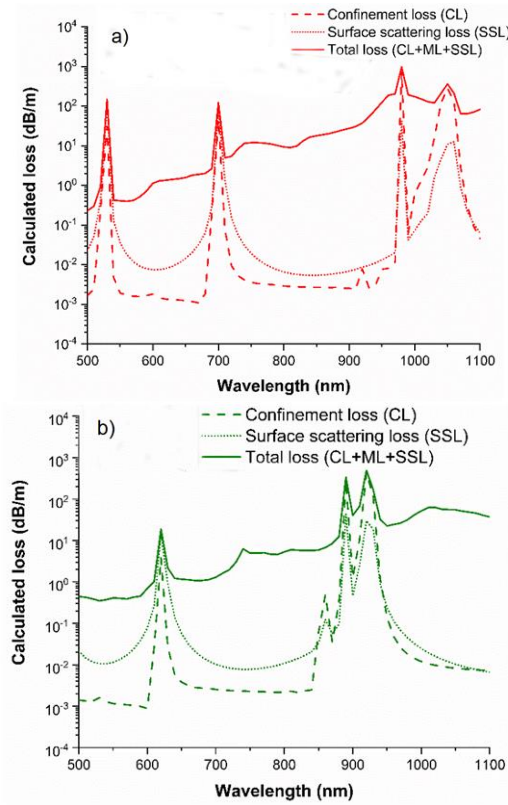

Figure 8.9. CL, SSL, and total loss of water-core AR_4 fiber (a), and ethanol-core AR_4 fiber (b).

8.4 Outlook of Application of Low-Index Liquid Core Antiresonant Fiber

As shown in Chapter 3, the buffers and CCM have the $n(\lambda)$ and transmission property close to that of water. In particular, among buffers and CCM, EXPRESS 5 has the highest $n(\lambda)$ (n = 1.3381 at λ=589 nm) and PBS has the lowest $n(\lambda)$ (n = 1.3348 at λ=589 nm). While $n(\lambda)$ of water and ethanol are 1.3332 and 1.361 at λ=589 nm. In long-term handling, $n(\lambda)$ of buffers and CCM do not change. Also, their transmission characteristics are almost the same that of water. Thus, it is possible to predict the optical properties of AR fibers infiltrated with these biological liquids by relying on the optical properties of the investigated AR fibers infiltrated with water and ethanol. Incorporating buffers and CCM into fiber geometry offer a promising

approach for creating compact, integrable and biocompatible all-fiber multifunctional optofluidic devices, which have potential applications in, e.g., sensing and bio-laser fiber.

A bio-laser uses the gain medium which is the aqueous solution containing biological material. Due to the effects of the light from the pump source, the lasing light can obtain from the fluorescent light of the biological components in the gain medium. There is some type of gain media compatible with an aqueous solution and biological components, e.g., fluorescent compounds (luciferin, vitamins) [149,150], natural fluorescent proteins [102]. The aqueous solution containing 293ETN cells, which has the green fluorescence protein (GFP), had been used as a gain medium for optofluidic laser [102]. The cells could emit the fluorescent light around 520 nm when they were pumped by laser source operating at 465 nm. Some researches for fluorescence of cells or bacteria in the bio-laser are shown in Table 8.2.

Table 8.2. Some bio-laser-based fluorescent light of microorganisms.

Pump wavelength (nm)	Organic component	Fluorescent wavelength (nm)	Ref.
465	293ETN cells	530	[102]
488	E. Coli Bacterial cells	545	[151]
488	Sf9 cells	508 -542	[152]
588	Sf9 cells	621-655	[152]
473	Aequorea victoria jellyfish cells	525	[153]

The buffers and CCM, which were shown in Chapter 3, are typically used to keep the appropriate microorganisms and provide the biological nutrients for their growth as well. Due to the slight difference of $n(\lambda)$ between water and these biological solutions, the spectral positions of transmission windows of the AR fibers infiltrated with these liquids may be close to those of AR fibers filled with water.

As shown in Figure 8.6 and 8.7, that the AR3 and AR4 fibers infiltrated with water have a transmission window of 550 ÷ 700 nm, which covers the pump wavelength (588 nm) as well as the fluorescent wavelength range of 621 ÷ 655 nm of Sf9 cells. Thus, The AR3 and AR4 fibers infiltrated with an aqueous solution containing Sf9 cells could be suitable to use for fiber laser with pump wavelength at 588 nm.

These liquids containing the microorganisms would be incorporated into AR fiber as a gain medium for laser, as shown in Figure 8.10. In this approach, it is possible to reduce the energy consumption of input light, because the light would be confined in the small effective area of the core of the AR fiber. With the facilitated microflow control and the flexible design, the liquid-filled AR fiber can ensure an

optimal overlap of optical properties between gain medium, laser pump system, and signal mode in the fiber. This allows optofluidic fiber laser can support the high output power [154].

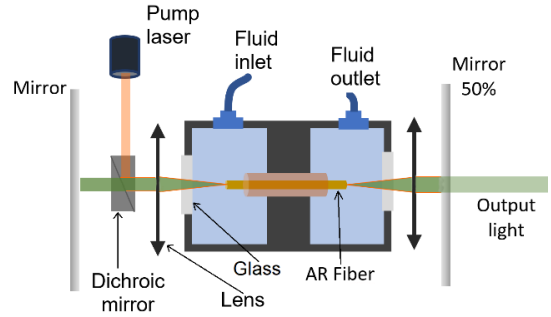

Figure 8.10. The schematic diagram of a model optofluidic bio-laser based on the AR fiber infiltrated with a biological solution containing the fluorescent microorganism.

Optofluidic bio-laser based on the AR fibers is also possible to utilize in biosensing applications. Due to the direct interaction of light with microorganisms containing in the AR fibers, the sensing signal derived from varying the light characteristics responding to the light-microorganism interaction is amplified. Thus, relying on laser characteristics, e.g., the input power threshold, the power, and spectra of output light, it is possible to obtain detailed information about the slight biological and chemistries changing of the liquid sample inside the fiber of the cavity.

The AR fibers infiltrated with water and ethanol are possible to apply for the temperature sensor. The temperature sensitivity of the investigated AR fibers is calculated according to Eq (8.2):

$$\frac{\partial \lambda_m}{\partial T} \approx -\frac{2t\alpha}{m} \frac{n_i(T)}{\sqrt{n_{silica}^2 - n_i^2(T)}}, \tag{8.2}$$

where α thermo-optic coefficient of the liquid. The α of silica, water, ethanol is 0.11×10^{-4} (K^{-1}), 1×10^{-4} (K^{-1}), and 4×10^{-4} (K^{-1}) [93], respectively. Since the α of silica is very small when compared to those of water and ethanol, the *n(λ)* of silica is constant with temperature variation in this case.

According to the Eq (8.2), the temperature sensitivities of the AR_3 and AR_4 fibers infiltrated ethanol around 1000 nm wavelength are -1.7 nm/^{0}C, and -1.65 nm/^{0}C, respectively. The AR fibers infiltrated with ethanol are more sensitive with temperature variation than that of AR fiber in [71], which has temperature sensitivity is -0.48nm/^{0}C, and also dedicated to a temperature sensor.

8.5 Conclusion

Experimental data confirmed that the broadness of the transmission window, as well as the number of non-transmission wavelengths in the investigated wavelength range of 500 ÷1700 nm, depends on the thickness of capillaries. In particular, AR_1 fiber has the thickness that is relatively larger than that of other investigated AR fiber, thus it has more non-transmission wavelengths in the investigated wavelength range. AR_4 fiber with thin thickness *t* offers the broad transmission window bandwidth in the investigated wavelength range.

When the AR fibers infiltrated with water and ethanol, they maintain the broad transmission windows. Their transmission windows will blue-shift, which relates to the reduction of the contrast of $n(\lambda)$ between cladding and core. The blue-shifting of the transmission window depends on $n(\lambda)$ of selected liquid and capillary thickness. In particular, since ethanol has a higher $n(\lambda)$ than that of water, the ethanol-core AR fibers have larger amount of blue-shifting that that of water-core AR fiber. Also, the amount of blue-shifting depends on the thickness of capillaries of AR fibers. For example, the amount of blue-shifting of AR_2 fiber (t=2.272 μm) blue-shifts amount of 680 nm and 785 nm with water and ethanol, respectively, while those of AR_4 fiber (t = 1.802 μm) are 545 nm and 625 nm.

The attenuation of AR_3 and AR_4 fiber infiltrated with liquids was estimated by numerical simulation. These results showed that the material loss of selected liquid is a majority part attributing to a total loss of the fiber. Thus, water-core and ethanol-core AR fiber have a relatively low loss in the visible range. However, it increases critically in the NIR range.

In the visible and NIR range, the buffers and CCM have $n(\lambda)$ and transmission characteristics close to those of water and ethanol. Therefore, based on these results, it is possible to predict the transmission characteristics of AR fibers when they are infiltrated with buffers and CCM for practical applications. Because an AR fiber has a relatively large core, it allows to create the fast liquid flow rate, as well as, controlling the liquid flow rate. AR fiber infiltrated with buffers and CCM containing the microorganism can use for, e.g., bio-laser fiber, biosensor, which is operated by fluorescence of cells and bacteria living in buffers and CCM.

With the observed broad transmission windows of the AR fibers in NIR range, they can be used as a promising approach for optofluidic applications. The results in this chapter confirm **Thesis 3**, that is "*Antiresonant fibers infiltrated with low-index liquids offer broadband transmission windows and are suitable for optofluidic systems".*

9 Conclusion and Future Work

9.1 Conclusion

In this dissertation, novel and versatile liquid core PCFs were investigated. This research was carried out to verify three theses:

- **Thesis 1:** *Silica hollow core photonic crystal fibers infiltrated with liquids can offer flat all-normal dispersion regime in near-infrared range. The dispersion feature is compatible with a central wavelength of commercially available femtosecond lasers for supercontinuum generation applications.*

- **Thesis 2:** *A broad spanning supercontinuum generation can be achieved in hollow core photonic crystal fibers with liquid infiltration and low peak power of input pulses.*

- **Thesis 3:** *Antiresonant fibers infiltrated with low-index liquids offer broadband transmission windows and are suitable for optofluidic systems.*

In order to verify these theses, the works in this dissertation were carried out from numerical simulation to design fiber structure, fabricate, and conduct the experimental systems to measure optical properties of the selected fibers. The good agreement between the experimental and simulated results confirm validity of our hypothesis.

In the case of **Thesis 1**, the large core PCFs were selectively infiltrated with toluene and CCl_4. These liquids were chosen for our works because of their high transparency in the investigated wavelength range (NIR) and low toxicity compared to that of other nonlinear liquids. Large core PCFs were used herein to get high coupling efficiency with standard single mode fiber when an all-fiber SCG system is considered. The dispersion characteristics of liquid core PCFs were numerically simulated and then verified by the March-Zehnder interferometer. The results in this dissertation showed the flat near-zero all-normal dispersion regime of liquid core PCFs in NIR range. The dispersion characteristics of the liquid core PCFs were compatible with commercial femtosecond lasers for SCG applications. Also, it is worth mentioning that PCFs have the design flexibility by changing the photonic factors, e.g., Λ, f, d_{core}, to optimize dispersion. Therefore, the use of liquid core PCF has been shown a high degree of freedom for the broad, brightness, coherent SCG from visible to MIR range with commercial femtosecond lasers as pump sources.

All-normal dispersion SCG in the liquid core PCFs were numerically simulated solving GNLSE by the split-step method and then verified by experimental set up with the femtosecond laser as a pump source. The laser had a central wavelength at 1030 nm. In the case of the toluene-core PCF, the observed SC spectrum spanned from 950 to 1150 nm in the normal dispersion regime. The replacement toluene by

CCl_4 would offer a further advantage for SCG applications. The most interesting feature of CCl_4 is its high transparency from visible to MIR range. In this dissertation, CCl_4-core PCF with a geometrical structure similar to that of toluene-core PCF offered all-normal dispersion SCG in wavelength range of 850 ÷ 1250 nm. The reason for moderate spectral bandwidth was the low nonlinear coefficient of the liquid core PCFs, because the large core PCFs were used herein. Increase nonlinear coefficient or input peak power are obligatory for broad SCG. Notwithstanding, the observed SC spectra in the liquid core PCFs confirms the possibility of liquid core PCFs for all-normal dispersion SCG. It is noted that, in the normal *D* regime, soliton formation and effects of input noises can be suppressed. As a result, the significant advantages for SCG can be obtained, e.g., the conservation of ultrashort compressible temporal pulses, uniformly flat spectral profiles, and, most importantly, high stability and coherence for a much larger range of pump pulse parameters.

In order to verify **Thesis 2**, the SCG in two different structures of CCL_4-core PCFs were numerically simulated and experimental verified. The different structures of CCl_4-core PCFs provide different dispersion profiles, such as the first one (*#F₁* fiber) has ZDW at 1740 nm, while the second one (*#F₂* fiber) with smaller core diameter has ZDW at 1440 nm, (Table 9.1). The pump wavelength used in this work had a central wavelength at 1560 nm. This pump wavelength was employed to better match the dispersion characteristics and the location of ZDWs. In this way, optimal PCFs are proposed with good nonlinear properties, and at the same time, they can offer further straightforwardness to incorporate in all-fiber systems.

Table 9.1. Investigated liquid core PCFs and their observed SCG.

Fiber	**d_{core} (µm)**	**ZDW (nm)**	**Bandwidth of Observed SCG (nm)**	**Laser source** - Pulse duration (fs) - Central wavelength (nm)
Toluene-core PCF	12	all-normal dispersion	950 ÷ 1150	400 1030
CCl_4-core PCF (*#F₁ fiber*)	9.8	1750	850 ÷ 1250	400 1030
			1350 ÷ 1900	90 1560
CCl_4-core PCF (*#F₂ fiber*)	5.3	1440	1000 ÷ 1900	90 1560

The high nonlinearity of liquids and flexibility of design to optimize the dispersion characteristics of PCFs were expected to offer the broad SCG with low input peak power of input pulses. A 650 nm spectral bandwidth of SC spectrum was observed in *#F₁* fiber with 10 kW peak power, and *#F₂* fiber offered a 900 nm spectral bandwidth with 5.5 kW peak power. These input peak powers were much lower compared to those in previous works [55,56]. In particular, as shown in Table 9.2, water-core PCFs in [55,56] needed peak power at 1.45 MW, or even at 150 MW for

SCG. The large core silica PCFs were also used for SCG [155-157]. Since of the low nonlinearity of silica, the large mode area silica PCF required the peak power at 1.1 MW for an octave-spanning SCG spectral [155]. The other silica PCFs, which has a small core diameter, and thus, increasing nonlinear coefficient, generated the coherent SCG with the peak power at 115 kW [156], 42 kW [157]. These peak powers are 10-times higher than that of $\#F_2$ fiber. The non-silica soft-glass fibers, e.g., tellurite fibers, have high nonlinearity and could offer coherent and board SCG with high input peak powers [158,159]. Therefore, based on the obtained results, it is possible to conclude that the use of hollow core PCF infiltrated with nonlinear liquid into the core as a propagation medium is able to obtain the broad SCG with low peak power of input pulses, and the SCG has the potential for high coherence.

The use of laser source with a central wavelength near ZDW of investigated fiber led to that obtained SCG was in both anomalous and normal *D* regime of investigated fibers. The anomalous dispersion SCG may have low coherence due to the effects of modulation instability, as well as the noises, e.g., laser noise and polarization noise. However, the use of short pulses (90 fs) and short fiber sample made to neglect the polarization noise, laser noise, and Raman scattering on coherence degradation, and thus, the numerical results pointed out that obtained SCG in CCL_4 – core PCFs had the potential for high coherence.

In this dissertation, the solid core LMA PCF was also developed, that offer high coupling efficiency with the liquid core PCFs. It is noted that free-space coupling was used for the SCG experiments in investigated liquid core PCFs. However, the system for SCG would not be all-fiber or compact anymore in this case. Thus, the use of short pulse delivery fiber to couple with the liquid core PCFs is necessary when a compact all-fiber SCG system is considered. The proposed LMA PCF is low *D*, low nonlinearity, single mode operation in NIR range, and low bending loss when compared with that of commercial LMA PCF. This fiber can resist up to peak power of 16 kW without temporal and spectral distortion and can offer high coupling efficiency with the investigated liquid core PCFs ($\#F_1$, $\#F_2$ fiber). The numerical calculation showed the coupling efficiency between the LMA PCF and $\#F_1$, $\#F_2$ fiber is 91%, and 79%, respectively. The high coupling efficiency between the liquid core PCFs with proposed LMA PCF confirms the feasibility of **Thesis 1** and **Thesis 2** and gives the capability for a feasible concept of low-cost compact all-fiber SCG system.

Table 9.2. Experimental results of SCG in liquid core PCF and some example for coherent SCG in solid core PCF in NIR range

#	Liquid core PCF	Nonlinear coefficient ($W^{-1}km^{-1}$)	Peak power (kW)	Pump wavelength (nm)	Pulse duration (fs)	Bandwidth of SCG (nm)	Ref.
1	Water-core PCF	1.5	1.45×10^3	980	60	600÷1140	[55]
2	Water-core PCF		150×10^3	1200	45	410÷1640	[56]
3	Solid core PCF filled with CCl_4 into an air-core in the cladding region as a second core for SCG	370	2 kW	1030	210	700÷1300	[57]
4	Toluene-core PCF	138	25	1030	400	950÷1100	[A1][a]
5	CCl_4 core PCF	22	62.5	1030	400	850÷1250	[A2][a]
6	CCL_4 core PCF	21	10	1560	90	1350÷1900	[A3][a]
7	CCL_4 core PCF	70	5.5	1560	90	1000÷1900	[A3][a]
Solid core PCF							
8	Large mode area silica core PCF	0.2	1.1×10^3	1260	100	550÷1600	[155]
9	Silica solid core PCF		115	1064	350	700÷1400	[156]
10	Silica solid core PCF	26	42	1050	50	750÷1400	[157]
11	Telluride core PCF	582.6	40	1560	90	1000÷2600	[158]
12	Solid core PCF (glass: SF_6/F_2)	7.6	100	2160	60	1100÷2700	[159]

[a] list of publications contributed by author.

In order to verify **Thesis 3**, the transmission windows of the AR fibers infiltrated with water and ethanol were measured. The AR fibers have different thicknesses of capillaries. The results confirm that the transmission windows of AR fiber infiltrated with low-index liquid maintains the broad transmission windows. In addition, the transmission window of AR fiber would blue-shift if this fiber infiltrated with low-index liquid. The amount of blue-shifting depends on the thickness t and $n(\lambda)$ of liquid, as shown in Table 9.3.

Table 9.3. The blue-shifting of AR fiber infiltrated with water and ethanol in NIR range.

Fiber / Liquid	**Amount of Blue-shifting**			
	AR_1 fiber (t =7.25 μm)	AR_2 fiber (t = 2.272 μm)	AR_3 fiber (t = 1.828 μm)	AR_4 fiber (t = 1.802 μm)
Water	655 nm	680 nm	560 nm	545 nm
Ethanol	760 nm	785 nm	680 nm	625 nm

The buffers and CCM, which are proper aqueous solution supporting life functions for bacteria or mammalian cells, have the linear optical properties similar to those of water. The difference of $n(\lambda)$ of these aqueous media and water and ethanol is below 0.0049 and 0.0262, respectively. Therefore, the optical properties of AR fiber infiltrated with these aqueous media would have optical properties similar to that of water-core or ethanol-core AR fiber. The use of AR fiber infiltrated with the buffers or CCM including the microorganism, e.g., bacteria or cells, allows increasing the light-microorganism interaction. Thus, it is capable to apply for optical sensors, bio-lasers, and other optofluidic systems.

9.2 Future Work of Fiber-Based Optofluidic System

In this works, I contributed the basic studies on liquid core fibers for optofluidic applications. The obtained results show the possibility of using liquid core PCFs for SCG, as well as AR fibers for sensors and optofluidic lasers. However, the experiments to measure the optical properties of liquid core fibers in this work used only free-space coupling. This can offer the high coupling efficiency, but the set up is not compact. Therefore, the use of proposed LMA PCF or single mode fiber to fusion splice with liquid core fibber is planning to implement as a future task for a compact all-fiber SCG system.

The PCFs with large hollow core were used to infiltrated with nonlinear liquids for SCG because they can offer high coupling efficiency with short pulse delivery fiber. This, in turn, offered large A_{eff}, and thus, low nonlinear coefficient. In the future works, one may develop liquid core PCFs with reduced in size core for broad spectral bandwidth SCG with low input peak powers.

It is worth mentioning that the liquids, e.g., CCl_4, CS_2, have high transparent up to MIR range. For example, the transmission windows of CCl_4 covers from the visible 0.5 μm to around 11 μm in the mid-infrared [46,95]. This future is more than offered by glasses dedicated to MIR range, for example, ZBLAN or tellurite glasses [160,161]. The transmission of ZBLAN is in the range of 0.3–6.7 μm [160]. Tellurite glasses exhibit transmission up to 35 μm but are opaque for wavelengths below 2 μm [161]. Although in this work, I did not profit from broadband MIR transmission offered by the liquids, the obtained results point out a high potential of the use of this liquid in fiber-based MIR systems.

Fibers infiltrated with low index liquids have been used for, e.g., chemical or biological sensors, based on the interaction between light and the liquids in both transverse and longitudinal dimensions. The light guidance in these fibers is based on either the band-gap or antiresonance mechanism. As shown in this dissertation, AR fibers infiltrated with low index liquids can offer broad transmission windows. The results will allow me in the future to develop AR fiber for concertation sensors and optofluidic fiber lasers.

References

[1] J. Hecht, *City of Light: The Story of Fiber Optics*, (The Sloan Technology Series, Oxford University Press USA, 1999).

[2] D. Colladon, “Sur les réflexions d’un rayon lumiére á l’interieur d’une veine liquide parabolique”, *Comptes Rendus.* 15, 800-802, (1842).

[3] J. Tyndall, “On some phenomena connected with the motion of liquids” Proceedings of the Royal Institution of Great Britain, 1, 446-448, (1854).

[4] C. W. Hansell, “Picture transmission”, *U.S. Patent.* 1, 751 584, (1930).

[5] J. L. Baird, “An improved method of and means for producing optical images”, *British Patent.* 285,738, (1928).

[6] A. C. S. van Heel, “A New Method of transporting Optical Images without Aberrations”, *Nature* 173(39), (1954).

[7] H. H. Hopkins and N. S. Kapany, “A Flexible Fibrescope, using Static Scanning”, *Nature* 173(39), (1954).

[8] C. K. Kao, G. A. Hockham, “Dielectric-fibre surface waveguides for optical frequencies”, *Proceedings of the Institution of Electrical Engineers* 113(7), 1151-1158, (1966).

[9] F. P. Kapron, D. B. Keck, and R. D. Maurer, “Radiation losses in glass optical waveguides”, *Appl. Phys. Lett.* 17 (10), 423-425 (1970).

[10] Corning, SMF-28 Ultra Optical Fibers, https://www.corning.com/cala/en/products/communication-networks/products/fiber/smf-28-ultra.html

[11] E. M. Dianov and V. M. Mashinsky, “Germania-based core optical fibers,” *J. Light. Technol.* 23 (11), 3500–3508 (2005).

[12] P. Kaiser and H. W. Astle, "Low-loss single-material fibers made from pure fused silica," *Bell Labs Tech. J.* 53(6), 1021 - 1039 (1974).

[13] R. D. Standley and W. S. Holden, "Experimental Results on a Single-Material Optical Fiber," *Bell Labs Tech. J.* 53(5), 779 - 784 (1974).

[14] S. John, "Strong localization of photons in certain disordered dielectric superlattices," *Phys. Rev. Lett.* 58, 2486 (1987).

[15] E. Yablonovitch, "Inhibited Spontaneous Emission in Solid-State Physics and Electronics," *Phys. Rev. Lett.* 58, 58, 2059 (1987).

[16] E. Yablonovitch, T. J. Gmitter, and K. M. Leung, "Photonic band structure: The face-centered-cubic case employing nonspherical atoms," *Phys. Rev. Lett.* 67, 2295 (1991).

[17] J. C. Knight, T. A. Birks, P. St. J. Russell, D. M. Atkin, “All-silica single-mode optical fiber with photonic crystal cladding”, *Opt. Lett.* 21(19), 1547-1549, (1996).

[18] R. F. Cregan, B. J. Mangan, J. C. Knight, T. A. Birks, P. St. J. Russell, P. J. Roberts, D. C. Allan, “Single-Mode Photonic Band Gap Guidance of Light in Air”, *Science* 285, 1537-1539, (1999).

[19] S. Février, B. Beaudou, and P. Viale, “Understanding origin of loss in large pitch hollow-core photonic crystal fibers and their design simplification,” *Opt. Express* 18(5), 5142–5150 (2010).

[20] F. Couny, P. J. Roberts, T. A. Birks, and F. Benabid, "Square-lattice large-pitch hollow-core photonic crystal fiber," *Opt. Express* 16(25), 20626-20636 (2008).

[21] A. Argyros, and J. Pla, "Hollow-core polymer fibres with a kagome lattice: potential for transmission in the infrared, " *Opt. Express* 15(12), 7713-7719 (2007).

[22] Y. Y. Wang, N. V. Wheeler, F. Couny, P. J. Roberts, and F. Benabid, "Low loss broadband transmission in hypocycloid-core Kagome hollow-core photonic crystal fiber," *Opt. Lett.* 36(5), 669-671 (2011).

[23] A. D. Pryamikov, A. S. Biriukov, A. F. Kosolapov, V. G. Plotnichenko, S. L. Semjonov, and E. M. Dianov, "Demonstration of a waveguide regime for a silica hollow - core microstructured optical fiber with a negative curvature of the core boundary in the spectral region > 3.5 μm, " *Opt. Express* 19(2), 1441-1448 (2011).

[24] P. J. Roberts, F. Couny, H. Sabert, B. J. Mangan, D. P. Williams, L. Farr, M. W. Mason, A. Tomlinson, “Ultimate low loss of hollow-core photonic crystal fibres”, *Opt. Express* 13(1), 236-244, (2005).

[25] NKT Photonics, Hollow Core PCFs, https://www.nktphotonics.com/lasers-fibers/product/hollow-core-photonic-crystal-fibers/

[26] T. Miya, Y. Terunuma, T. Hosaka, T. Miyashita, “Ultimate low-loss single mode fibre at 1.55μm”, *Electron. Lett.* 15(4), 106-108, (1979).

[27] NKT Photonics, LARGE MODE AREA PHOTONIC CRYSTAL FIBERS, https://www.nktphotonics.com/lasers-fibers/product/large-mode-area-photonic-crystal-fibers/

[28] A. V. Vasudevan Nampoothiri, A. M. Jones, C. Fourcade-Dutin, C. Mao, N. Dadashzadeh, B. Baumgart, Y.Y. Wang, M. Alharbi, T. Bradley, N. Campbell, F. Benabid, B. R. Washburn, K. L. Corwin, and W. Rudolph, “Hollow-core Optical Fiber Gas Lasers (HOFGLAS): a review ”, *Opt. Mater. Express* 2(7), 948-961 (2012) .

[29] A. S. Webb, F. Poletti, D. J. Richardson, J. K. Sahu, “Suspended-core holey fiber for evanescent-field sensing”, *Opt. Eng.* 46(1), 010503 (2007).

[30] J. M. Dudley and J. R. Taylor, *Supercontinuum Generation in Optical Fibers* (Cambridge University, 2010).

[31] Yu, Y. Liu, Y. Wang, Z. Wang, X. Zhang, X.Liu, S. Gao, X. Wang, and Pu Wang, "Optofluidic laser based on a hollow-core negative curvature fiber," *Nanophotonics* 7(7), 1307–1315 (2018).

[32] C. Wei, J. T. Young, C. R. Menyuk, and J. Hu, "Temperature sensor based on liquid-filled negative curvature optical fibers," *OSA. Continuum.* 2(7), 2123-2130 (2019).

[33] F. Shimizu, "Frequency broadening in liquids by a short light pulse," *Phys. Rev. Lett.* 19, 1097 (1967).

[34] R. R. Afano, *The Supercontinuum Laser Source* (Springer-Verlag, 2016).

[35] N. M. Israelsen, C. R. Petersen, A. Barh, D. Jain, M. Jensen, G. Hannesschläger, P. Tidemand-Lichtenberg, C. Pedersen, A. Podoleanu, and O. Bang, "Real-time High-Resolution Mid-infrared Optical Coherence Tomography," *Light: Sci. Appl.* 8(11), (2019).

[36] C. R. Petersen, N. Prtljaga, M. Farries, J. Ward, B. Napier, G. R. Lloyd, J. Nallala, N. Stone, and O. Bang, "Mid-infrared multispectral tissue imaging using a chalcogenide fiber supercontinuum source," *Opt. Lett.* 43(5), 999–1002 (2018).

[37] C. R. Petersen, P. M. Moselund, L. Huot, L. Hooper, and O. Bang, "Towards a table-top synchrotron based on supercontinuum generation," *Infrared Phys. Technol.* 91, 182–186 (2018).

[38] S. Kedenburg, A. Steinmann, R. Hegenbarth, T. Steinle, and H. Giessen, "Nonlinear refractive indices of nonlinear liquids: wavelength dependence and influence of retarded response," *Appl. Phys. B* 117, 803–816 (2014).

[39] G. Tao, H. Ebendorff-Heidepriem, A. M. Stolyarov, S. Danto, J. V. Badding, Y. Fink, J. Ballato, and A. F. Abouraddy, "Infrared fibers," *Adv. Opt. Photonics* 7, 379–458 (2015).

[40] S. Dai, Y. Wang, X. Peng, P. Zhang, X. Wang, and Y. Xu, "A review of mid-infrared supercontinuum generation in chalcogenide glass fibers," *Appl. Sci.* 8(5), 707 (2018).

[41] C. R. Petersen, U. Møller, I. Kubat, B. Zhou, S. Dupont, J. Ramsay, T. Benson, S. Sujecki, N. Abdelmoneim, Z. Tang, "Mid-infrared supercontinuum covering the 1.4–13.3 μm molecular fingerprint region using ultra-high NA chalcogenide step-index fibre," *Nat. Photonics* 8, 830–834 (2014).

[42] C. Markos, J. C. Travers, A. Abdolvand, B. J. Eggleton, and O. Bang, "Hybrid photonic-crystal fiber," *Rev. Mod. Phys.* 89(4), 045003 (2017).

[43] M. Cassataro, D. Novoa, M. C. Günendi, N. N. Edavalath, M. H. Frosz, J. C. Travers, and P. S. J. Russell, "Generation of broadband mid-IR and UV light

in gas-filled single-ring hollow-core PCF," *Opt. Express* 25(7), 7637–7644 (2017).

[44] A. I. Adamu, Md. S. Habib, C. R. Petersen, J. E. A. Lopez, B. Zhou, A. Schülzgen, M. Bache, R. Amezcua-Correa, O. Bang, and C. Markos, "Deep-UV to Mid-IR Supercontinuum Generation driven by Mid-IR Ultrashort Pulses in a Gas-filled Hollow-core Fiber," *Sci. Rep.* 9(1), (2019).

[45] P. P. Ho and R. R. Alfano, "Optical Kerr effect in liquids," *Phys. Rev. A* 20(5), 2170–2187 (1979).

[46] S. Kedenburg, M. Vieweg, T. Gissibl, and H. Giessen, "Linear refractive index and absorption measurements of nonlinear optical liquids in the visible and near-infrared spectral region," *Opt. Mater. Express* 2(11), 1588–1611 (2012).

[47] K. Schaarschmidt, H. Xuan, J. Kobelke, M. Chemnitz, I. Hartl, and M. A. Schmidt, "Long-term stable supercontinuum generation and watt-level transmission in liquid core optical fibers," *Opt. Lett.* 44(9), 2236-2239 (2019).

[48] M. Chemnitz, M. Gebhardt, C. Gaida, F. Stutzki, J. Kobelke, J. Limpert, A. Tünnermann, and M. A. Schmidt, "Hybrid soliton dynamics in liquid core fibers," *Nat. Commun.* 8(1), 42 (2017).

[49] M. Chemnitz, C. Gaida, M. Gebhardt, F. Stutzki, J. Kobelke, A. Tünnermann, J. Limpert, and M. A. Schmidt, "Carbon chloride-core fibers for soliton mediated supercontinuum generation," *Opt. Express* 26(3), 3221–3235 (2018).

[50] M. Chemnitz, R. Scheibinger, C. Gaida, M. Gebhardt, F. Stutzki, S. Pumpe, J. Kobelke, A. Tünnermann, J. Limpert, and M. A. Schmidt, "Thermodynamic control of soliton dynamics in liquid core fibers," *Optica* 5(6), 695–703 (2018).

[51] A. Ferrando, E. Silvestre, P. Andrés, J. J. Miret, and M. V. Andrés, "Designing the properties of dispersion-flattened photonic crystal fibers," *Opt. Express* 9(13), 687-697 (2001).

[52] G. Fanjoux, S. Margueron, J.-C. Beugnot, and T. Sylvestre, "Supercontinuum generation by stimulated Raman–Kerr scattering in a liquid core optical fiber," *J. Opt. Soc. Am. B* 34(8), 1677–1683 (2017).

[53] D. Churin, T. N. Nguyen, K. Kieu, R. A. Norwood, and N. Peyghambarian, "Mid-IR supercontinuum generation in an integrated liquid core optical fiber filled with CS2," *Opt. Mater. Express* 3(9), 1358–1364 (2013).

[54] S. Kedenburg, T. Gissibl, T. Steinle, A. Steinmann, and H. Giessen, "Towards integration of a liquid-filled fiber capillary for supercontinuum generation in the 1.2-2.4 μm range," *Opt. Express* 23(7), 8281–8289 (2015).

[55] A. Bozolan, C. J. S. de Matos, C. M. B. Cordeiro, E. M. Dos Santos, and J. Travers, “Supercontinuum generation in a water-core photonic crystal fiber,” *Opt. Express* 16(13), 9671–9676 (2008).

[56] J. Bethge, A. Husakou, F. Mitschke, F. Noack, U. Griebner, G. Steinmeyer, and J. Herrmann, “Two-octave supercontinuum generation in a water-filled photonic crystal fiber,” *Opt. Express* 18(6), 6230–6240 (2010).

[57] M. Vieweg, T. Gissibl, S. Pricking, B. T. Kuhlmey, D. C. Wu, B. J. Eggleton, and H. Giessen, “Ultrafast nonlinear optofluidics in selectively liquid-filled photonic crystal fibers,” *Opt. Express* 18(24), 25232–25240 (2010).

[58] A. M. Heidt, J. S. Feehan, J. H. V. Price, and T. Feurer, “Limits of coherent supercontinuum generation in normal dispersion fibers,” *J. Opt. Soc. Am. B* 34(4), 764 775 (2017).

[59] R. Zhang, J. Teipel, and H. Giessen, “Theoretical design of a liquid-core photonic crystal fiber for supercontinuum generation,” *Opt. Express* 14(15), 6800-6812 (2006).

[60] L. C. Van, A. Anuszkiewicz, A. Ramaniuk, R. Kasztelanic, K. D. Xuan, V. C. Long, M. Trippenbach, and R. Buczyński, “Supercontinuum generation in photonic crystal fibers with core filled with toluene,” *J. Opt.* 19(12), 125604 (2017).

[61] Q. H. Dinh, J. Pniewski, H.L. Van, A. Ramaniuk, V. C. Long, K. Borzycki, K. D. Xuan, M. Klimczak, and R. Buczyński, "Optimization of optical properties of photonic crystal fibers infiltrated with carbon tetrachloride for supercontinuum generation with subnanojoule femtosecond pulses," *Appl. Opt.* 57(14), 3738-3746 (2018).

[62] P. Zhao, M. Reichert, S. Benis, D. J. Hagan, and E. W. V. Stryland, “Temporal and polarization dependence of the nonlinear optical response of solvents,” *Optica* 5(5), 583–594 (2018).

[63] M. Nissen, B. Doherty, J. Hamperl, J. Kobelke, K. Weber , T. Henkel, and M, A. Schmidt, “UV Absorption Spectroscopy in Water-Filled Antiresonant Hollow Core Fibers for Pharmaceutical Detection,” *Sensors* 18(2), 478 (2018).

[64] L. Kröckel, T. Frosch, M.A. Schmidt, "Multiscale spectroscopy using a monolithic liquid core waveguide with laterally attached fiber ports," *Anal. Chim. Acta* 875, 1-6 (2015).

[65] G. Antonopoulos, F. Benabid, T. A. Birks, D. M. Bird, J. C. Knight, and P. St. J. Russell, "Experimental demonstration of the frequency shift of bandgaps in photonic crystal fibers due to refractive index scaling," *Opt. Express* 14(7), 3000-3006 (2006).

[66] F. M. Cox, A. Argyros, and M. C. J. Large, "Liquid-filled hollow core microstructured polymer optical fiber," *Opt. Express* 14(9), 4135 (2006).

[67] D. Yan, J. Popp, M. W. Pletz, and T. Frosch, "Fiber enhanced Raman sensing of levofloxacin by PCF bandgap-shifting into the visible range," *Anal. Methods* 10(6), 586–592 (2018).

[68] Ruskuc, P. Koehler, M. A. Weber, A. Andres-Arroyo, M. H. Frosz, P. S. J. Russell, and T. G. Euser, "Excitation of higher-order modes in optofluidic photonic crystal fiber," *Opt. Express* 26(23), 30245 (2018).

[69] R. Buczynski, I. Kujawa, R. Kasztelanic, D. Pysz, K. Borzycki, F. Berghmans, H. Thienpont and R. Stepien, "Supercontinuum generation in all-solid photonic crystal fiber with low index core," *Las. Phys.* 22(4), 784–790 (2012).

[70] S. Unterkofler, R. J. McQuitty, T. G. Euser, N. J. Farrer, P. J. Sadler, and P. St.J. Russell, "Microfluidic integration of photonic crystal fibers for online photochemical reaction analysis, " *Opt. Lett.* 37(11), 1952-1954 (2012).

[71] S. Liu, Y. Wang, M. Hou, J. Guo, Z. Li, and P. Lu, "Anti-resonant reflecting guidance in alcohol-filled hollow core photonic crystal fiber for sensing applications," *Opt. Express* 21(25), 31690-31697 (2013).

[72] X. Liu, W. Ding, Y. Wang, S. Gao, L. Cao, X. Feng, and P. Wang, "Characterization of a liquid-filled nodeless anti-resonant fiber for biochemical sensing," *Opt. Lett.* 42(4), 863-866 (2017).

[73] J. Yu, Y. Liu, Y. Wang, Z. Wang, X. Zhang, X. Liu, S. Gao, X. Wang, and Pu Wang, "Optofluidic laser based on a hollow-core negative-curvature fiber," *Nanophotonics* 7(7), 1307–1315 (2018).

[74] A. M. Cubillas, X. Jiang, T. G. Euser, N.Taccardi, B. J. M. Etzold, P. Wasserscheid, and P. St. J. Russell, "Photochemistry in a soft-glass single-ring hollow-core photonic crystal fibre, " *Analyst* 142(6), 925-929 (2017).

[75] R. E. Noskov, A. A. Zanishevskaya, A. A. Shuvalov, S. V. German, O. A. Inozemtseva, T. P. Kochergin, E. N. Lazareva, V. V. Tuchin, P. Ginzburg, J. S. Skibina, and Dmitry A. Gorin, "Enabling magnetic resonance imaging of hollow-core microstructured optical fibers via nanocomposite coating," *Opt. Express* 27(7), 9868-9878 (2019).

[76] P. Russell, "Photonic Crystal Fibers," *Science* 299, 358 (2003).

[77] J. C. Knight, "Photonic crystal fibres," *Nature* 424, 847-51 (2003).

[78] Thorlabs, Hollow-core photonic crystal fiber, https://www.thorlabs.com/newgrouppage9.cfm?objectgroup_id=912

[79] C. Wei, R. J. Weiblen, C. R. Menyuk, and J. Hu, "Negative curvature fibers," Adv. Opt. Photonics **9**(3), 504-561 (2017).

[80] G.P. Agrawal, *Nonlinear Fiber Optics*, 4th ed., (Academic Press, San Diego, 2007).

[81] A. Birks, J. C. Knight, andP. St. J. Russell, "Endlessly single-mode photonic crystal fiber," *Opt. Lett.* 22, 961–963 (1997).

[82] P. Diament, *Wave Transmission and Fiber Optics* (Macmillan, New York, 1990).

[83] Y. R. Shen, *Principles of Nonlinear Optics* (Wiley, New York, 1984).

[84] K. J. Blow and D. Wood, “Theoretical description of transient stimulated Raman scattering in optical fibers,” *IEEE J. Quantum Electron.* 25(12), 2665 (1989).

[85] A. M. Heidt, A. Hartung, G. W. Bosman, P. Krok, E. G. Rohwer, H. Schwoerer, and H. Bartelt, "Coherent octave spanning near-infrared and visible supercontinuum generation in all-normal dispersion photonic crystal fibers, " *Opt. Express* 19(4), 3775-3787 (2011).

[86] J. M. Dudley, G. Genty, and S. Coen, "Supercontinuum generation in photonic crystal fiber," *Rev. Mod. Phys.* 78, 1135 (2006).

[87] A. M. Heidt, *Novel coherent supercontinuum light sources based on all-normal dispersion fibers*, Dissertation of Doctor of Philosophy at the University of Stellenbosch (2011).

[88] F. M. Mitschke and L. F. Mollenauer, “Discovery of the soliton self-frequency shift,” *Opt. Lett.* 11, 659–661 (1986).

[89] Y. Wu, M. Meneghetti, J. Troles, and J.-L. Adam, “Chalcogenide Microstructured Optical Fibers for Mid-Infrared Supercontinuum Generation: Interest, Fabrication, and Applications,” *Appl. Sci.* 8(9), 1637 (2018).

[90] M. Reichert, H. Hu, M. R. Ferdinandus, M. Seidel, P. Zhao, T. R. Ensley, D.Peceli, J. M. Reed, D. A. Fishman, S. Webster, D.J. Hagan, and E. W. Van Stryland, “Temporal, spectral, and polarization dependence of the nonlinear optical response of carbon disulfide,” *Optica* 1(6), 436-445 (2014).

[91] H. Zhang, S. Chang, J. Yuan, D. Huang, "Supercontinuum generation in chloroform-filled photonic crystal fibers," *Optik* 121(9), 783-787 (2010).

[92] S. Pumpe, M. Chemnitz, J. Kobelke, and M. A. Schmidt, “Monolithic optofluidic mode coupler for broadband thermo- and piezo-optical characterization of liquids,” *Opt. Express* 25(19), 22932–22946 (2017).

[93] M. J. Weber, *Handbook of Optical Materials* (CRC, Boca Raton, Florida, 2003).

[94] H. L. Van, R. Buczynski, V. C. Long, M. Trippenbach, K. Borzycki, A. N. Manh, R. Kasztelanic, “Measurement of temperature and concentration influence on the dispersion of fused silica glass photonic crystal fiber infiltrated with water–ethanol mixture,” *Opt. Commun.* 407, 417-422 (2018).

[95] C.D. Craver, *The Coblentz Society Desk Book of Infrared Spectra* (The Coblentz Society, 1982).

[96] M. L. Miguez, T. G. B. De Souza, E. C. Barbano, S. C. Zilio, and L. Misoguti, “Measurement of third-order nonlinearities in selected solvents as a function of the pulse width,” *Opt. Express* 25(4), 3553-3565 (2017).

[97] N. Munera and R. A. Herrera, “Modelling a nonlinear optical switching in a standard photonic crystal fiber infiltrated with carbon disulfide,” *Opt. Commun.* 368, 185-189 (2016).

[98] Health Effects Notebook for Hazardous Air Pollutants | Hazardous Air Pollutants | US EPA https://www.epa.gov/haps/health-effects-notebook-hazardous-air-pollutants

[99] M. McParland, N. Bates, *Toxicology of Solvents* (iSmithers Rapra Publishing, 2004).

[100] M. Vieweg, T. Gissibl, Y. Kartashov, L. Torner, and H. Giessen, "Spatial solitons in optofluidic waveguide arrays with focusing ultrafast Kerr nonlinearity," *Opt. Lett.* 37(13), 2454 (2012).

[101] L. Shao, Z. Liu, J. Hu, D. Gunawardena, and H.-Y. Tam, “Optofluidics in Microstructured Optical Fibers,” *Micromachines* 9(4), 145-164 (2018).

[102] M. C. Gather, and S. H. Yun, “Single-cell biological lasers,” *Nat. Photon.* 5(7), (2011).

[103] X. Fan, SH. Yun, “The potential of optofluidic biolasers,” *Nat. Methods.* 11(2), 141-7 (2014).

[104] X. Fan, and S. -H. Yun, “Optofluidic Bio-Lasers: Concept and Applications,” *Nat. Methods.* 11(2), 141–147 (2014)

[105] R. Scorpio, *Fundamentals of Acids, Bases, Buffers & Their Application to Biochemical Systems* (Kendall Hunt Pub Co, 2000).

[106] M. Madigan and J. Martinko, *Brock Biology of Microorganisms* (Pearson, 2017).

[107] K.J. Ryan, C.G. Ray, *Sherris Medical Microbiology* (McGraw-Hill Education, 2014).

[108] J. R. Brody and S.E. Kern, “History and principles of conductive media for standard DNA electrophoresis,” *Anal. Biochem.* 333, 1–13 (2004).

[109] M. Daimon, and A. Masumura, “Measurement of the refractive index of distilled water from the near-infrared region to the ultraviolet region, *Appl. Opt.* 46, 3811-3820 (2007).

[110] E. Hecht, *Optics*, (Addison Wesley, 2002).

[111] Y. Xu, X. Chen, and Y. Zhu, “High sensitive temperature sensor using a liquid core optical fiber with small refractive index difference between core and cladding materials,” *Sensors* 8(3), 1872-1878 (2008).

[112] Y. Shevchenko, G. Camci-Unal, D. F. Cuttica, M.R. Dokmeci, J. Albert, A. Khademhosseini, “Surface plasmon resonance fiber sensor for real-time and

label-free monitoring of cellular behavior," *Biosens. Bioelectron.* 15(56), 359–367 (2014).

[113] P. R. Naira and M. A. Alam, "Theory of "Selectivity" of label-free nanobiosensors: A geometro-physical perspective," *J. Appl. Phys.* 107, 064701 (2010).

[114] Lumerical Mode Solution, https://www.lumerical.com/tcad-products/mode/.

[115] Z. Zhu, T. G. Brown, "Full-vectorial finite-difference analysis of microstructured optical fibers", *Opt. Express* 10(17), 853-864, (2002).

[116] D. Pysz, I. Kujawa, R. St˛epień, M. Klimczak, A. Filipkowski, M. Franczyk, L. Kociszewski, J. Buźniak, K. Haraśny, and R. Buczyński, "Stack and draw fabrication of soft glass microstructured fiber optics," *Bull. Pol. Acad. Sci.: Tech. Sci.* 62(4), 667–682 (2014).

[117] I. Kubat and O. Bang, "Multimode supercontinuum generation in chalcogenide glass fibres," *Opt. Express* 24(3), 2513 (2016).

[118] D. Mogilevtsev, T. A. Birks, and P. St. J. Russell, "Group-velocity dispersion in photonic crystal fibers," *Opt. Express* 23(21), (1998).

[119] Y. Huang, Y. Xu, and A. Yariv, "Fabrication of functional microstructured optical fibers through a selectivefilling technique," *Appl. Phys. Lett.* 85(22), 5182–5184 (2004).

[120] Norland Products, https://www.norlandprod.com/adhesives/noa%2073.html

[121] L. Xiao, W. Jin, M. Demokan, H. Ho, Y. Hoo, and C. Zhao, "Fabrication of selective injection microstructured optical fibers with a conventional fusion splicer," *Opt. Express* 13(22), 9014–9022 (2005).

[122] K. Nielsen, D. Noordegraaf, T. Sørensen, A. Bjarklev, and T. P Hansen, "Selective filling of photonic crystal fibres," *J. Opt. A: Pure Appl. Opt.* **7**(8), (2005).

[123] W. H. Knox, N. M. Pearson, K. D.Li, and C. A. Hirlimannt, "Interferometric measurements of femtosecond group delay in optical components," *Opt. Express* 13(7), 574-576 (1988).

[124] P. Hlubina, D. Ciprian, and R. Chlebus, "Group index dispersion of holey fibres measured by a white-light spectral interferometric technique," *Opt. Commun.* 281(15-16), 4008-4013 (2008).

[125] G. Genty, T. Ritari, and H. Ludvigsen, "Supercontinuum generation in large mode-area microstructured fibers," *Opt. Express.* 13(21), 8625 (2005).

[126] I. B. Gonzalo, R. D. Engelsholm, M. P. Sørensen, and O. Bang, "Polarization noise places severe constraints on coherence of all-normal dispersion femtosecond supercontinuum generation," *Sci. Rep.* **8**, 6579, 2018.

[127] BlueCut Femtosecond Fiber Laser,
https://www.menlosystems.com/products/microjoule-lasers/bluecut/

[128] E. Genier, P. Bowen, T. Sylvestre, J. M. Dudley, P. Moselund, and O. Bang, "Amplitude noise and coherence degradation of femtosecond supercontinuum generation in all-normal-dispersion fibers**,"** *J. Opt. Soc. Am. B.* 36(2), A161-A167 (2018).

[129] Menlo Systems, C-Fiber Femtosecond Erbium Laser, https://www.menlosystems.com/products/femtosecond-lasers-and-amplifiers/c-fiber/

[130] D. McMorrow, W. Lotshaw, and G. Kenney-Wallace, "Femtosecond optical Kerr studies on the origin of the nonlinear responses in simple liquids," *IEEE J. Quantum Elect.* 24, 443–454 (1988).

[131] N. Thantu and R. S. Schley, "Ultrafast third-order nonlinear optical spectroscopy of chlorinated hydrocarbons," *Vib. Spectroscopy* 32, 215–223 (2003).

[132] J. M. Dudley, S. Coen, "Numerical Simulations and Coherence Properties of Supercontinuum Generation in Photonic Crystal and Tapered Optical Fibers," *IEEE J. Sel. Top. Quantum Electron.* 8(3), 651 - 659 (2002).

[133] J. Herrmann, U. Griebner, N. Zhavoronkov, A. Husakou, D. Nickel, J. C. Knight, W. J. Wadsworth, P. St. J. Russell, and G. Korn, "Experimental Evidence for Supercontinuum Generation by Fission of Higher-Order Solitons in Photonic Fibers," *Phys. Rev. Lett.* 88(17), 173901 (2002).

[134] I. B. Gonzalo, O. Bang, "Role of the Raman gain in the noise dynamics of all-normal dispersion silica fiber supercontinuum generation," *J. Opt. Soc. Am. B.* 35(9), 2102-2110 (2018).

[135] F. Guichard, A. Giree, Y. Zaouter, M. Hanna, G. Machinet, B. Debord, F. Gérôme, P. Dupriez, F. Druon, C. Hönninger, E. Mottay, F. Benabid, P. Georges, "Nonlinear compression of high energy fiber amplifier pulses in air-filled hypocycloid-core Kagomé fiber," *Opt. Express* 23(6), 7416–7423 (2015).

[136] W. Belardi, "Design and properties of hollow antiresonant fibers for the visible and near infrared spectral range," *J. Light. Technol.* 33(21), 4497–4503 (2015).

[137] M. Michieletto, J.s K. Lyngsø, C. Jakobsen, J. Lægsgaard, O. Bang, and T. T. Alkeskjold, "Hollow-core fiber for high power delivery," *Opt. Express* 24(7), 7103-7119 (2016).

[138] H. Lim, F.W. Wise, "Control of dispersion in a femtosecond ytterbium laser by use of hollow-core photonic bandgap fiber," *Opt. Express* 12(10), 2231–2235 (2004).

[139] C.J. Engelbrecht, R.S. Johnston, E.J. Seibel, F. Helmchen, "Ultra-compact fiber-optic two-photon microscope for functional fluorescence imaging in vivo," *Opt. Express* 16(8), 5556–5564 (2008).

[140] M. Napierała, T. Nasilowski, E. Bereś-Pawlik, P. Mergo, F. Berghmans, H. Thienpont, “Large-mode-area photonic crystal fiber with double lattice constant structure and low bending loss,” *Opt. Express* 19(23), 22628–22636 (2011).

[141] M. M. Vogel, M. Abdou-Ahmed, A. Voss, and T. Graf, “Very-large-mode-area, single-mode multicore fiber,” *Opt. Lett.* 34(18), 2876-8 (2009).

[142] J.C. Knight, T.A. Birks, R.F. Cregan, P.S.J. Russell, P.D. de Sandro, “Large mode area photonic crystal fibre,” *Electron. Lett.* 34(13), 1347 – 1348 (1998).

[143] J.C. Baggett, T.M. Monro, K. Furusawa, V. Finazzi, D.J. Richardson, “Understanding bending losses in holey optical fibers,” *Opt. Commun.* 227 (4–6) 317–335 (2003).

[144] K. Saitoh, Y. Tsuchida, M. Koshiba, N.A. Mortensen, “Endlessly single-mode holey fibers: the influence of core design,” *Opt. Express* 13 (26) 10833–10839 (2005).

[145] D. Marcuse, “Loss analysis of single-mode fiber splices,” *Bell Labs Tech. J.* 56 (5), 703 – 718 (1977).

[146] M. Klimczak, D. Dobrakowski, A. N. Ghosh, G. Stępniewski, D. Pysz, G. Huss, T. Sylvestre, and R. Buczyński, "Nested capillary anti-resonant silica fiber with mid-infrared transmission and low bending sensitivity at 4000 nm," *Opt. Lett.* 44(17), 4395-4398 (2019).

[147] W. Belardi and J. C. Knight, “Hollow antiresonant fibers with reduced attenuation,” *Opt. Lett.* 39(7), 1853-1856 (2014).

[148] F. Poletti, "Nested antiresonant nodeless hollow core fiber," *Opt. Express* 22(20), 23807–23828 (2014).

[149] X. Wu, Q. Chen, Y. Sun, and X. Fan, “Bio-inspired optofluidic lasers with luciferin,” *Appl. Phys. Lett.* 102, 203706 (2013).

[150] S. Nizamoglu, M. C. Gather, and S. H. Yun, “All-Biomaterial Laser using Vitamin and Biopolymers,” *Adv. Mater*. 25, 5943-5947 (2013).

[151] A. Jonáš, M.. Aas, Y. Karadag, S. Manioğlu, S. Anand, D.McGloin, H. Bayraktar, and A. Kiraz, "In vitro and in vivo biolasing of fluorescent proteins suspended in liquid microdroplet cavities," *Lap Chip* 14(16), 3093-3100 (2014).

[152] Q. Chen, X. Zhang, Y. Sun, M. Ritt, S. Sivaramakrishnan, and X. Fan, "Highly sensitive fluorescent protein FRET detection using optofluidic lasers," *Lab Chip* 13(14), 2679-2681 (2013).

[153] M. C. Gather, and S. H. Yun, "Bio-optimized energy transfer in densely packed fluorescent protein enables near-maximal luminescence and solid-state lasers," *Nat. Commun*. 5(1), (2014).

[154] J. T. F. Johnston, R. H. Brady, and W. Proffitt, “Powerful singlefrequency ring dye laser spanning the visible spectrum,” *Appl. Opt.* 21 (13), 2307–2316 (1982).

[155] R. Cherif, I. Nikolov, M. Zghal, and M. Danailov, “Supercontinuum generation in a large mode area photonic crystal fiber,” Proceedings of SPIE - The International Society for Optical Engineering (2009).

[156] L. E. Hooper, P. J. Mosley, A. C. Muir, W. J. Wadsworth, and J. C. Knight, “Coherent supercontinuum generation in photonic crystal fiber with all-normal group velocity dispersion,” *Opt. Express* 19, 4902–4907 (2011).

[157] A. M. Heidt, A. Hartung, G. W. Bosman, P. Krok, E. G. Rohwer, H. Schwoerer, and H. Bartelt, “Coherent octave spanning near-infrared and visible supercontinuum generation in all-normal dispersion photonic crystal fibers,” *Opt. Express* 19, 3775–3787 (2011).

[158] M. Klimczak, D. Michalik, G. Stępniewski, T. Karpate, J. Cimek, X. Forestier, R. kasztelanic, D. Pysz, R. Stępień, and R. Buczyński, “Coherent supercontinuum generation in tellurite glass regular lattice photonic crystal fibers,” *J. Opt. Soc. Am. B.* 6 (2), A112-A124 (2019).

[159] M. Klimczak, B. Siwicki, B. Zhou, M. Bache, D. Pysz, O. Bang, and R. Buczynski, “Coherent supercontinuum bandwidth limitations under femtosecond pumping at 2 μm in all-solid soft glass photonic crystal fibers,” *Opt. Express* 24, 29406–29416 (2016).

[160] J. Cimek, X. Forestier, R. Stepien, M. Klimczak, and R. Buczynski, “Synthesis conditions of ZBLAN glass for mid-infrared optical components,” *Photon. Lett. Pol.* 10, 8–10 (2018).

[161] D. Le Coq, S. Cui, C. Boussard-Plédel, P. Masselin, E. Bychkov, and B. Bureau, “Telluride glasses with far-infrared transmission up to 35 mm,” *Opt. Mater.* 72, 809–812 (2017).